Rosenthal, Y., Holbourn, A.E., Kulhanek, D.K., and the Expedition 363 Scientists
Proceedings of the International Ocean Discovery Program Volume 363
publications.iodp.org

https://doi.org/10.14379/iodp.proc.363.110.2018

Site U1489[1]

Y. Rosenthal, A.E. Holbourn, D.K. Kulhanek, I.W. Aiello, T.L. Babila, G. Bayon, L. Beaufort, S.C. Bova, J.-H. Chun, H. Dang, A.J. Drury, T. Dunkley Jones, P.P.B. Eichler, A.G.S. Fernando, K. Gibson, R.G. Hatfield, D.L. Johnson, Y. Kumagai, T. Li, B.K. Linsley, N. Meinicke, G.S. Mountain, B.N. Opdyke, P.N. Pearson, C.R. Poole, A.C. Ravelo, T. Sagawa, A. Schmitt, J.B. Wurtzel, J. Xu, M. Yamamoto, and Y.G. Zhang[2]

Keywords: International Ocean Discovery Program, IODP, *JOIDES Resolution*, Expedition 363, Site U1489, South Eauripik Rise, Pleistocene, Pliocene, Miocene, Neogene, northern sector Western Pacific Warm Pool, orbital-scale climate variability, high-resolution interstitial water sampling, Last Glacial Maximum ocean density structure, carbonate accumulation, chalk, color banding, biosilica, soft-sediment deformation, stratigraphic intercalibration and cyclostratigraphy, high-resolution interstitial water sampling, Last Glacial Maximum ocean density structure, carbonate diagenesis

Contents

Background and objectives

International Ocean Discovery Program (IODP) Site U1489 (proposed Site WP-04A) is located on the western slope of the southern Eauripik Rise at 02°07.19′N, 141°01.67′E in 3421 m water depth (Figure **F1**). The site is situated on seismic Line RR1313-WP4-2 at the intersection with seismic Line RR1313-WP4-3 (Figure **F2**). The seismic profile shows a continuous succession of hemipelagic, carbonate-rich sediment with basement at >650 meters below seafloor (mbsf) (Rosenthal et al., 2016) (Figure **F3**). Site U1489 is located ~81 km west-northwest of Site U1488 and ~105 km northwest of Deep Sea Drilling Project (DSDP) Site 62 and shows a similar sedimentary cover (Shipboard Scientific Party, 1971).

Site U1489 is situated on the western slope of the southern part of Eauripik Rise, within the Caroline Basin north of Papua New Guinea (Figure **F1**). The roughly north–south trending Eauripik Rise is an ~250 km wide aseismic ridge that rises ~1–2 km above the surrounding seafloor and separates the East and West Caroline Basins. Magnetic Anomalies C13–C9 in both basins show that ocean crust formed along roughly east–west spreading centers from the Eocene until the late Oligocene. Offsets in these anomalies and the lack of magnetic lineations beneath the Eauripik Rise supports the interpretation that it formed due to excess submarine volcanism along a leaky north–south transform fault (Hegarty and Weissel, 1988.) An alternative interpretation attributes the formation of the Eauripik Rise to the northward passage of a mantle hotspot that contributed to the tectonically and structurally complex region sur-

Figure F1. Eauripik Rise within the Caroline Basin showing location of Sites U1488–U1490 (yellow circles).

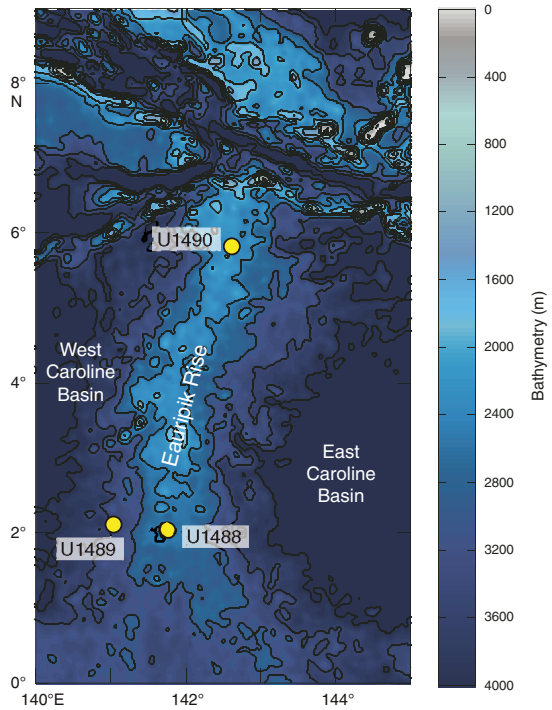

[1] Rosenthal, Y., Holbourn, A.E., Kulhanek, D.K., Aiello, I.W., Babila, T.L., Bayon, G., Beaufort, L., Bova, S.C., Chun, J.-H., Dang, H., Drury, A.J., Dunkley Jones, T., Eichler, P.P.B., Fernando, A.G.S., Gibson, K., Hatfield, R.G., Johnson, D.L., Kumagai, Y., Li, T., Linsley, B.K., Meinicke, N., Mountain, G.S., Opdyke, B.N., Pearson, P.N., Poole, C.R., Ravelo, A.C., Sagawa, T., Schmitt, A., Wurtzel, J.B., Xu, J., Yamamoto, M., and Zhang, Y.G., 2018. Site U1489. *In* Rosenthal, Y., Holbourn, A.E., Kulhanek, D.K., and the Expedition 363 Scientists, *Western Pacific Warm Pool*. Proceedings of the International Ocean Discovery Program, 363: College Station, TX (International Ocean Discovery Program). https://doi.org/10.14379/iodp.proc.363.110.2018

[2] **Expedition 363 Scientists' addresses.**

MS 363-110: Published 8 June 2018

Figure F2. Contoured bathymetric map showing location of Site U1489 on seismic Lines RR1313-WP4-2 and RR1313-WP4-3 collected during the R/V *Roger Revelle* 13-13 cruise. Bathymetry is based on EM122 multibeam survey collected during the same cruise. Numbers along the seismic lines (black) are common depth points. Location of hydrocast Station HC38 is shown with data displayed in Figure F4. Contour interval = 20 m.

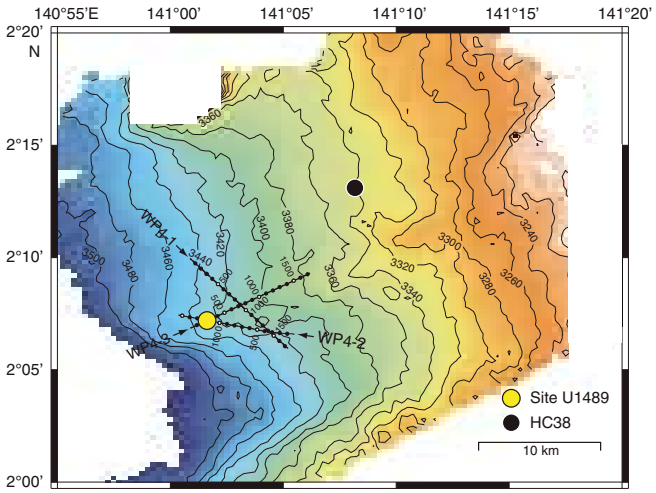

Figure F3. Seismic Line RR1313-WP4-3 showing the location of Site U1489. Location of crossing seismic lines shown with dashed line at top. CDP = common depth point. Seismic data available at **http://www-udc.ig.utexas.edu/sdc/cruise.php?cruiseIn=rr1313**.

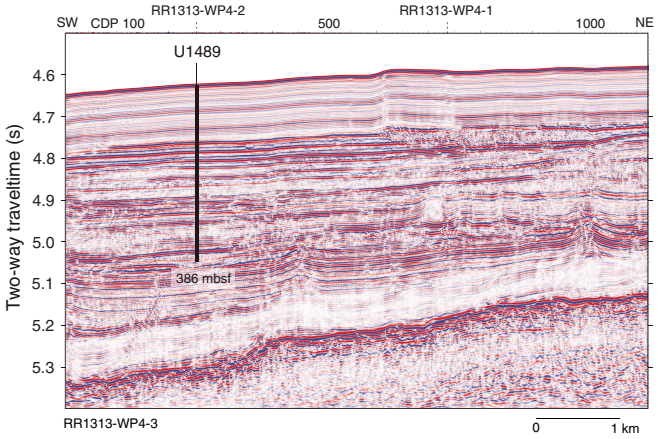

rounding the Sorol Trough (Bracey, 1975). Seismic refractions show thickened ocean crust beneath the Eauripik Rise, and a small free-air anomaly and positive geoid anomaly indicate a compensated structure reaching deep into the mantle (Hegarty and Weissel, 1988). Although there are no discernible magnetic lineations on the Eauripik Rise, these data and the recovery of tholeiitic basalt at Site 62 (Shipboard Scientific Party, 1971) make it difficult to argue that it is a remnant of ancient continental material. The igneous rocks recovered from the bottom of Site 62 are slightly vesicular and highly altered and contain calcite veins with well-preserved foraminifers and nannofossils. The dolomitization of overlying limestone suggests that these basalts intruded into marine chalk leading to extensive diagenetic reactions near the base of the sedimentary succession.

Site U1489 is located ~2° north of the Equator and is thus suitable for reconstructing the hydrographic history of the Western Pacific Warm Pool (WPWP). The comparatively low sedimentation rate at this site, typical of open-ocean environments, allows coring of the middle Miocene at a relatively shallow depth, which was not possible at Site U1488, offering the opportunity to reconstruct the evolution of the WPWP from the Middle Miocene Climate Optimum to the middle Miocene climate transition associated with expansion of the Antarctic ice sheet. At ~3400 meters below sea level (mbsl), the site is bathed by modified Lower Circumpolar Deepwater (LCDW) and therefore will be useful to monitor past changes in this water mass (Figure **F4**). Because this site is close to Site U1488 but at ~900 m deeper water depth, comparing results from these two sites also offers the opportunity to investigate potential diagenetic effects of foraminifer geochemical proxy records. High-resolution interstitial water sampling at this site will be used for geochemical reconstructions of the deep Pacific water mass ($\delta^{18}O$, salinity, and seawater chemistry) during the Last Glacial Maximum (LGM).

Figure F4. Hydrographic profiles of temperature, salinity, and dissolved oxygen near Sites U1488 and U1489 at hydrocast Station HC38 on Figure F2 (Y. Rosenthal, unpubl. data). NPSTW = North Pacific Subtropical Water, NPIW = North Pacific Intermediate Water, UCDW = Upper Circumpolar Deepwater, LCDW = Lower Circumpolar Deepwater.

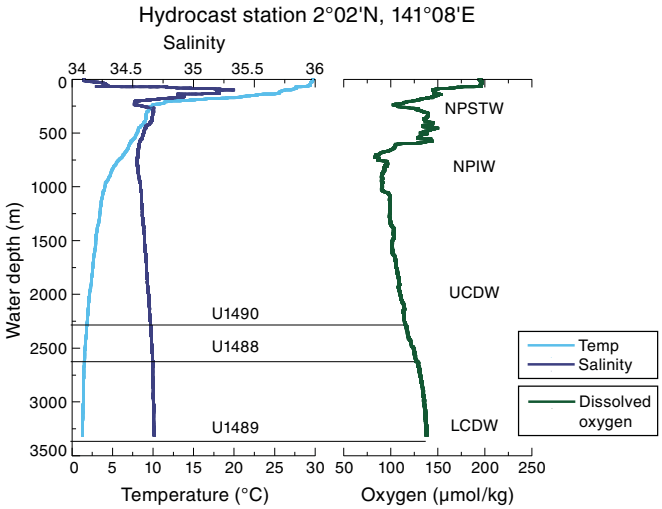

Operations

Transit to Site U1489

The 44.0 nmi transit to Site U1489 was completed in 5.2 h at an average speed of 8.5 kt. We lowered the thrusters and switched to dynamic positioning mode at 1442 h (all times local ship time; UTC + 10 h) on 24 November 2016. After arriving on site, we deployed a positioning beacon at 1448 h before commencing coring operations. Excessive noise was noted in the beacon signal, requiring that a second beacon be deployed and used as the primary beacon.

Operations summary

Site U1489 was an alternate site that was added during the expedition to complement the record cored at Site U1488. We initially planned to core three holes to 200 mbsf; however, we requested and received permission to core to 5.0 s two-way traveltime at our site location on seismic reflection profile Line RR1313 WP4-2 (Figure **F3**). We ultimately cored four holes at Site U1489 (Table **T1**). Hole U1489A consisted of a single full advanced piston corer (APC) core,

Table T1. Site U1489 core summary. CSF = core depth below seafloor (mbsf in text), DRF = drilling depth below rig floor, DSF = drilling depth below seafloor. APC = advanced piston corer, XCB = extended core barrel, HLAPC = half-length advanced piston corer. Core types: H = advanced piston corer, F = half-length advanced piston corer, X = extended core barrel, numeric core type = drilled interval. APCT-3 = advanced piston corer temperature tool, Icefield = orientation tool. (Continued on next two pages.) **Download table in CSV format.**

Hole U1489A
Latitude: 02°07.1976′N
Longitude: 141°01.6654′E
Water depth (m): 3419.8
Date started (UTC): 24 November 2016, 0442 h
Date finished (UTC): 24 November 2016, 1515 h
Time on hole (days): 0.44
Seafloor depth DRF (m): 3431.0
Seafloor depth calculation method: APC calculated depth
Rig floor to sea level (m): 11.20
Drilling system: 11-7/16 inch APC/XCB DC280 bit
Penetration DSF (m): 9.5
Cored interval (m): 9.5
Recovered length (m): 9.53
Recovery (%): 100.32
Total cores (no.): 1
APC cores (no.): 1
Age of oldest sediment cored: middle Pleistocene

Hole U1489B
Latitude: 02°07.1984′N
Longitude: 141°01.6757′E
Water depth (m): 3419.5
Date started (UTC): 24 November 2016, 1515 h
Date finished (UTC): 25 November 2016, 1355 h
Time on hole (days): 0.94
Seafloor depth DRF (m): 3430.7
Seafloor depth calculation method: APC calculated depth
Rig floor to sea level (m): 11.20
Drilling system: 11-7/16 inch APC/XCB DC280 bit
Penetration DSF (m): 129.2
Cored interval (m): 129.2
Recovered length (m): 120.66
Recovery (%): 93.39
Total cores (no.): 14
APC cores (no.): 14
Age of oldest sediment cored: late Miocene

Hole U1489C
Latitude: 02°07.1772′N
Longitude: 141°01.6746′E
Water depth (m): 3423.68
Date started (UTC): 25 November 2016, 1355 h
Date finished (UTC): 27 November 2016, 1900 h
Time on hole (days): 2.21

Hole U1489C (continued).
Seafloor depth DRF (m): 3434.9
Seafloor depth calculation method: APC calculated depth
Rig floor to sea level (m): 11.22
Drilling system: 11-7/16 inch APC/XCB DC280 bit
Penetration DSF (m): 385.6
Cored interval (m): 385.6
Recovered length (m): 376.35
Recovery (%): 97.6
Total cores (no.): 42
APC cores (no.): 29
HLAPC cores (no.): 2
XCB cores (no.): 11
Age of oldest sediment cored: early Miocene

Hole U1489D
Latitude: 02°07.1761′N
Longitude: 141°01.6651′E
Water depth (m): 3421.55
Date started (UTC): 27 November 2016, 1900 h
Date finished (UTC): 29 November 2016, 1612 h
Time on hole (days): 1.88

Hole U1489D (continued).
Seafloor depth DRF (m): 3432.8
Seafloor depth calculation method: APC calculated depth
Rig floor to sea level (m): 11.25
Drilling system: 11-7/16 inch APC/XCB DC280 bit
Penetration DSF (m): 385.6
Cored interval (m): 238.8
Recovered length (m): 229.24
Recovery (%): 96.0
Drilled interval (m): 146.8
Drilled interval (no.): 1
Total cores (no.): 26
APC cores (no.): 14
XCB cores (no.): 12
Age of oldest sediment cored: early Miocene

Core	Date (2016)	Time on deck UTC (h)	Depth DSF (m) Top of interval	Depth DSF (m) Bottom of interval	Interval advanced (m)	Depth CSF (m) Top of cored interval	Depth CSF (m) Bottom of cored interval	Recovered length (m)	Curated length (m)	Recovery (%)	Sections (N)	Comments
363-U1489A-												
1H	24 Nov	1500	0	9.5	9.5	0	9.53	9.53	9.53	100	8	Icefield
363-U1489B-												
1H	24 Nov	1610	0	5.7	5.7	0	5.76	5.76	5.76	101	5	Icefield
2H	24 Nov	1720	5.7	15.2	9.5	5.7	15.54	9.84	9.84	104	8	Icefield
3H	24 Nov	1825	15.2	24.7	9.5	15.2	25.07	9.87	9.87	104	8	Icefield, mechanically sheared
4H	24 Nov	1935	24.7	34.2	9.5	24.7	34.74	10.04	10.04	106	8	Icefield, APCT-3
5H	24 Nov	2030	34.2	43.7	9.5	34.2	44.14	9.94	9.94	105	8	Icefield
6H	24 Nov	2130	43.7	53.2	9.5	43.7	53.56	9.86	9.86	104	8	Icefield, split liner
7H	24 Nov	2240	53.2	62.7	9.5	53.2	63.26	10.06	10.06	106	8	Icefield, APCT-3, liner twisted and split throughout
8H	24 Nov	2335	62.7	72.2	9.5	62.7	72.55	9.85	9.85	104	8	Icefield, mechanically sheared
9H	25 Nov	0035	72.2	81.7	9.5	72.2	82.11	9.91	9.91	104	8	Icefield
10H	25 Nov	0140	81.7	91.2	9.5	81.7	88.41	6.71	6.71	71	7	Icefield, APCT-3
11H	25 Nov	0350	91.2	100.7	9.5	91.2	91.20	0	6.71	0	0	Icefield
12H	25 Nov	0740	100.7	110.2	9.5	100.7	110.70	10.00	10.00	105	8	Icefield, APCT-3, 2 wireline runs, reshot at same depth
13H	25 Nov	0950	110.2	119.7	9.5	110.2	119.26	9.06	9.06	95	8	Icefield, 2 wireline runs, reshot at same depth
14H	25 Nov	1050	119.7	129.2	9.5	119.7	129.46	9.76	9.76	103	8	Icefield; attempt Core 15H, but came up empty; terminate hole
363-U1489C-												
1H	25 Nov	1700	0	3.5	3.5	0	3.59	3.59	3.59	103	4	Icefield
2H	25 Nov	1815	3.5	13.0	9.5	3.5	13.36	9.86	9.86	104	8	Icefield

Table T1 (continued).

Core	Date (2016)	Time on deck UTC (h)	Depth DSF (m) Top of interval	Depth DSF (m) Bottom of interval	Interval advanced (m)	Depth CSF (m) Top of cored interval	Depth CSF (m) Bottom of cored interval	Recovered length (m)	Curated length (m)	Recovery (%)	Sections (*N*)	Comments
3H	25 Nov	2035	13.0	22.5	9.5	13.0	22.90	9.90	9.90	104	8	Icefield, mechanically sheared
4H	25 Nov	2150	22.5	32	9.5	22.5	32.39	9.89	9.89	104	8	Icefield
5H	25 Nov	2250	32.0	41.5	9.5	32.0	41.66	9.66	9.66	102	8	Icefield
6H	25 Nov	2355	41.5	51.0	9.5	41.5	51.45	9.95	9.95	105	8	Icefield
7H	26 Nov	0055	51.0	60.5	9.5	51.0	60.92	9.92	9.92	104	8	Icefield
8H	26 Nov	0200	60.5	70.0	9.5	60.5	70.40	9.90	9.90	104	8	Icefield
9H	26 Nov	0300	70.0	79.5	9.5	70.0	79.99	9.99	9.99	105	8	Icefield
10H	26 Nov	0355	79.5	89.0	9.5	79.5	89.44	9.94	9.94	105	8	Icefield
11H	26 Nov	0450	89.0	98.5	9.5	89.0	98.88	9.88	9.88	104	8	Icefield
12H	26 Nov	0545	98.5	108.0	9.5	98.5	108.49	9.99	9.99	105	8	Icefield
13H	26 Nov	0645	108.0	117.5	9.5	108.0	118.00	10.00	10.00	105	8	Icefield
14H	26 Nov	0740	117.5	127.0	9.5	117.5	127.44	9.94	9.94	105	8	Icefield
15H	26 Nov	0840	127.0	136.5	9.5	127.0	136.16	9.16	9.16	96	7	Icefield
16H	26 Nov	0935	136.5	146.0	9.5	136.5	143.46	6.96	6.96	73	6	Icefield, liner twisted and split throughout
17H	26 Nov	1035	146.0	155.5	9.5	146.0	155.89	9.89	9.89	104	8	Icefield
18H	26 Nov	1135	155.5	165.0	9.5	155.5	165.32	9.82	9.82	103	8	Icefield
19H	26 Nov	1225	165.0	174.5	9.5	165.0	174.55	9.55	9.55	101	8	Icefield
20H	26 Nov	1320	174.5	184.0	9.5	174.5	183.33	8.83	8.83	93	7	Icefield
21H	26 Nov	1420	184.0	193.5	9.5	184.0	190.10	6.10	6.10	64	5	Icefield, liner imploded (bottom)
22H	26 Nov	1515	193.5	203.0	9.5	193.5	203.28	9.78	9.78	103	8	Icefield, liner split throughout
23H	26 Nov	1620	203.0	212.5	9.5	203.0	212.89	9.89	9.89	104	8	Icefield
24H	26 Nov	1720	212.5	222.0	9.5	212.5	222.46	9.96	9.96	105	8	Icefield
25H	26 Nov	1825	222.0	231.5	9.5	222.0	231.94	9.94	9.94	105	8	Icefield
26H	26 Nov	1930	231.5	241.0	9.5	231.5	241.38	9.88	9.88	104	8	Icefield
27H	26 Nov	2030	241.0	250.5	9.5	241.0	250.60	9.60	9.60	101	8	Icefield
28H	26 Nov	2135	250.5	260.0	9.5	250.5	260.51	10.01	10.01	105	8	Icefield
29H	26 Nov	2355	260.0	269.5	9.5	260.0	269.98	9.98	9.98	105	8	Icefield, drillover
30F	27 Nov	0115	269.5	274.2	4.7	269.5	273.59	4.09	4.09	87	5	Imploded liner, pumped liner out
31F	27 Nov	0245	274.2	278.9	4.7	274.2	279.16	4.96	4.96	106	5	Drill over
32X	27 Nov	0435	278.9	288.6	9.7	278.9	287.11	8.21	8.21	85	7	
33X	27 Nov	0545	288.6	298.3	9.7	288.6	297.27	8.67	8.67	89	8	Shattered liner, pumped liner out
34X	27 Nov	0735	298.3	308.0	9.7	298.3	308.02	9.72	9.72	100	8	
35X	27 Nov	0920	308.0	317.7	9.7	308.0	317.63	9.63	9.63	99	8	
36X	27 Nov	1030	317.7	327.4	9.7	317.7	327.40	9.70	9.70	100	8	
37X	27 Nov	1135	327.4	337.1	9.7	327.4	335.20	7.80	7.80	80	6	
38X	27 Nov	1230	337.1	346.8	9.7	337.1	347.00	9.90	9.90	102	8	
39X	27 Nov	1330	346.8	356.5	9.7	346.8	356.68	9.88	9.88	102	8	
40X	27 Nov	1440	356.5	366.2	9.7	356.5	364.05	7.55	7.55	78	6	
41X	27 Nov	1540	366.2	375.9	9.7	366.2	372.03	5.83	5.83	60	5	
42X	27 Nov	1640	375.9	385.6	9.7	375.9	384.26	8.65	8.36	89	7	
363-U1489D-												
1H	27 Nov	2100	0	3.7	3.7	0	3.69	3.69	3.69	100	4	Icefield
2H	27 Nov	2225	3.7	13.2	9.5	3.7	13.64	9.94	9.94	105	8	Icefield
3H	27 Nov	2345	13.2	22.7	9.5	13.2	23.14	9.94	9.94	105	8	Icefield
4H	28 Nov	0055	22.7	32.2	9.5	22.7	32.73	10.03	10.03	106	8	Icefield, APCT-3
5H	28 Nov	0150	32.2	41.7	9.5	32.2	41.81	9.61	9.61	101	8	Icefield
6H	28 Nov	0250	41.7	51.2	9.5	41.7	51.53	9.83	9.83	103	8	Icefield
7H	28 Nov	0355	51.2	60.7	9.5	51.2	58.47	7.27	7.27	77	6	Icefield, APCT-3
8H	28 Nov	0450	60.7	70.2	9.5	60.7	66.95	6.25	6.25	66	5	Icefield
9H	28 Nov	0550	70.2	79.7	9.5	70.2	80.13	9.93	9.93	105	8	Icefield, split liner
10H	28 Nov	0700	79.7	89.2	9.5	79.7	89.79	10.09	10.09	106	8	Icefield, APCT-3
11H	28 Nov	0755	89.2	98.7	9.5	89.2	99.20	10.00	10.00	105	8	Icefield
12H	28 Nov	0900	98.7	108.2	9.5	98.7	108.63	9.93	9.93	105	8	Icefield
13H	28 Nov	1010	108.2	117.7	9.5	108.2	118.31	10.11	10.11	106	8	Icefield, APCT-3
14H	28 Nov	1110	117.7	127.2	9.5	117.7	126.98	9.28	9.28	98	8	Icefield
151	28 Nov	1600	127.2	274.0	146.8	*****Drilled from 127.2 to 274.0 m DSF without coring*****						
16X	28 Nov	1720	274.0	283.7	9.7	274.0	283.71	9.71	9.71	100	8	
17X	28 Nov	1840	283.7	293.4	9.7	283.7	292.72	9.02	9.02	93	7	
18X	28 Nov	1950	293.4	303.1	9.7	293.4	302.78	9.38	9.38	97	7	
19X	28 Nov	2100	303.1	312.8	9.7	303.1	313.00	9.90	9.90	102	8	
20X	28 Nov	2205	312.8	322.5	9.7	312.8	322.22	9.42	9.42	97	7	
21X	28 Nov	2310	322.5	332.2	9.7	322.5	332.20	9.70	9.70	100	8	
22X	29 Nov	0015	332.2	341.9	9.7	332.2	339.21	7.01	7.01	72	6	
23X	29 Nov	0120	341.9	351.6	9.7	341.9	348.89	6.99	6.99	72	6	
24X	29 Nov	0225	351.6	361.3	9.7	351.6	361.24	9.64	9.64	99	8	
25X	29 Nov	0315	361.3	371.0	9.7	361.3	371.10	9.80	9.80	101	8	
26X	29 Nov	0410	371.0	380.7	9.7	371.0	378.14	7.14	7.14	74	6	
27X	29 Nov	0510	380.7	385.6	4.9	380.7	386.33	5.63	5.63	115	5	

which indicated we missed the mudline. Hole U1489B was cored with the APC system to 129.2 mbsf. We terminated coring in this hole because of coring difficulties that resulted in poor recovery and core disturbance. Hole U1489C was cored to 385.6 mbsf using a combination of APC, half-length advanced piston corer (HLAPC), and extended core barrel (XCB) coring, and Hole U1489D was cored with the APC system to 127.2 mbsf, drilled without coring to 274.0 mbsf, and then cored with the XCB system to 385.6 mbsf.

Hole U1489A was cored with the APC system using orientation and nonmagnetic hardware. Core 1H recovered a full core barrel, indicating that we had missed the mudline, so we terminated coring. We collected 9.53 m of core over 9.5 m of coring (100% recovery) in Hole U1489A.

Hole U1489B was cored to 129.2 mbsf with the APC system using orientation and nonmagnetic hardware (Cores 1H through 14H). Downhole formation temperature measurements using the advanced piston corer temperature tool (APCT-3) were taken on Cores 4H (34.2 mbsf), 7H (62.7 mbsf), 10H (91.2 mbsf), and 12H (110.2 mbsf); however, only one measurement was of good quality (Core 10H). The measurements taken while collecting Cores 4H and 7H showed possible movement related to heavy seas, and the measurement from Core 12H was of very poor quality. We also collected high-resolution interstitial water samples at a frequency of one (5–10 cm) whole-round sample per section over the entire cored succession in Hole U1489B. Coring difficulties included premature failure of the APC shear pins due to ship motion on Cores 3H and 8H, as well as one core with no recovery (Core 11H) and two cores requiring a second coring attempt to retrieve sediment (Cores 12H and 13H). As these cores appeared very disturbed, we opted to terminate coring in Hole U1489B. We collected 120.66 m of core over 129.2 m of coring (93% recovery) in Hole U1489B.

Hole U1489C was cored to 269.5 mbsf (Cores 1H through 29H) with the APC using orientation and nonmagnetic hardware. Core 29H required drillover to extract it from the formation, indicating APC refusal. We switched to the HLAPC system and cored only to 278.9 mbsf (Cores 30F and 31F) before excessive overpull indicated HLAPC refusal. We then switched to the XCB system to core to 385.6 mbsf (Cores 32X through 42X), where we terminated coring. We collected 376.35 m of core over 385.6 m of coring (98% recovery) in Hole U1489C.

Hole U1489D was cored to recover material for the splice over the upper ~120 mbsf interval that was heavily sampled for interstitial water in Hole U1489B and to collect a second copy of the deeper succession at Site U1489. Hole U1489D was cored with the APC system using orientation and nonmagnetic hardware to 127.2 mbsf (Cores 1H through 14H). Because several of the APCT-3 measurements provided spurious results in Hole U1489B, we opted to take additional measurements in Hole U1489D while collecting Cores 4H (32.2 mbsf), 7H (60.7 mbsf), 10H (89.2 mbsf), and 13H (117.7 mbsf). All four measurements provided good results. We drilled without coring from 127.2 to 274.0 mbsf and then cored using the XCB system to 385.6 mbsf (Cores 16X through 27X), where we terminated coring. We collected 229.24 m of core over 238.8 m of coring (96% recovery) in Hole U1489D.

Operations at Site U1489 ended at 0212 h on 30 November 2016. Total time spent at Site U1489 was 131.5 h (5.5 days). We collected a total of 58 APC cores, recovering 527.85 m of core over 535.4 m of coring (98.6% recovery). We also collected 2 HLAPC cores, recovering 9.05 m of core over 9.4 m of coring (96.3% recovery) and 23 XCB cores, retrieving 198.88 m of core over 218.3 m of coring (92.6% recovery). In total, we collected 735.78 m of sediment over 763.1 m of coring (96.4% recovery).

Hole U1489A

We prepared and spaced out the bottom-hole assembly (BHA), which consisted of an APC/XCB coring assembly with two stands of drill collars. We also drifted (checked the interior to make sure it was clear) and strapped (measured) 18 stands of 5 inch drill pipe prior to deployment. The seafloor depth was measured at 3436.4 meters below rig floor (mbrf) with the precision depth recorder (PDR), and we positioned the bit at 3431.0 mbrf to shoot the first core. Hole U1489A was spudded at 0035 h on 25 November 2016. Core 1H recovered 9.53 m of sediment with the APC system. Since we had a full core liner, indicating that we had missed the mudline, we terminated coring in Hole U1489A at 0100 h. Total time spent in the hole was 10.25 h (0.4 days).

One APC core was taken in Hole U1489A, recovering 9.53 m of sediment over 9.5 m of coring (100.3% recovery).

Hole U1489B

The vessel was offset 20 m east of Hole U1489A, and the drill string was spaced out with the bit at 3427.0 mbrf. Hole U1489B was spudded at 0145 h on 25 November 2016, with Core 1H recovering 5.76 m of sediment, establishing a seafloor depth of 3419.5 mbsl. Oriented APC coring using the Icefield MI-5 core orientation tool with nonmagnetic hardware continued to 129.20 mbsf (Cores 1H through 14H). Downhole formation temperature measurements using the APCT-3 were taken on Cores 4H (34.2 mbsf), 7H (62.7 mbsf), 10H (91.2 mbsf), and 12H (110.2 mbsf); however, only one measurement was of good quality (Core 10H). The measurements taken while collecting Cores 4H and 7H showed possible movement related to heavy seas, and the measurement from Core 12H was of very poor quality. We also collected high-resolution interstitial water samples at a frequency of one (5–10 cm) whole-round sample per section over the entire cored succession in Hole U1489B.

Coring in Hole U1489B was terminated early due to repeated coring problems. The shear pins failed prematurely due to ship motion on Cores 3H and 8H. Although both cores had full recovery, the majority of the sediment was highly disturbed. Core 6H had a split liner, although there appeared to be minimal drilling disturbance as a result. Core 11H had zero recovery. Core 12H also returned an empty core liner; however, the core barrel was lowered again and the core reshot from the same depth, returning a full core barrel on the second run. We then lowered an XCB core barrel to determine that the inner diameter of the BHA was clear. After retrieving the XCB core barrel, we continued coring with the APC system. Core 13H also returned an empty core liner on the first run, but material was recovered after shooting a second time from the same depth. Core 14H (129.20 mbsf) recovered a full core barrel, but an attempt to collect Core 15H once again resulted in an empty core barrel. At that point we terminated coring after noting the significant amount of drilling disturbance in Core 12H. The drill string was pulled out of the hole, with the bit clearing the seafloor at 2344 h on 25 November, ending operations in Hole U1489B. Total time spent in the hole was 23.0 h (1.0 day). While pulling the drill string, the drilling crew changed out as many components as possible in both core barrels in case the coring difficulties were related to a mechanical problem.

A total of 14 APC cores were taken in Hole U1489B. We recovered 120.66 m of sediment over 129.2 m of coring for a total recovery of 93.4%.

Hole U1489C

The vessel was offset 40 m south of Hole U1489B in case the coring difficulties encountered in Hole U1489B were related to the formation, and the drill string was spaced out with the bit at 3429.0 mbrf. Hole U1489C was spudded at 0235 h on 26 November 2016, with Core 363-U1489C-1H recovering 3.59 m of sediment, establishing a seafloor depth of 3423.7 mbsl. Oriented APC coring using the Icefield MI-5 core orientation tool with nonmagnetic hardware continued to 269.5 mbsf (Cores 1H through 29H). The shear pins again failed prematurely on Core 3H. The core liners of Cores 16H and 22H were both split throughout, and the bottom of the liner imploded on Core 21H. Core 29H had excessive overpull and required drillover to extract it from the formation, indicating APC refusal. We then switched to the HLAPC and cored to 278.9 mbsf (Cores 30F and 31F). Core 30F had to be pumped out of the core barrel, and Core 31F had excessive overpull and required drillover, indicating HLAPC refusal. We switched to the XCB and continued coring to 385.6 mbsf (Cores 32X through 42X). Core 33X had a shattered liner and had to be pumped out of the core barrel. We terminated coring at 385.6 mbsf after determining that the velocity model used to calculate the approval depth for the hole was incorrect. The drill string was pulled out of the hole, with the bit clearing the seafloor at 0500 h on 28 November, ending operations in Hole U1489C. Total time spent in the hole was 53.0 h (2.2 days).

A total of 29 APC cores were taken in Hole U1489C. We recovered 271.76 m of sediment over 269.5 m of coring for a total recovery of 100.8%. We collected 2 HLAPC cores, recovering 9.05 m of sediment over 9.4 m of coring (96.3% recovery). We also collected 11 XCB cores, recovering 95.54 m of sediment over 106.7 m of coring (89.5% recovery). Overall recovery for Hole U1489C was 376.35 m of sediment over 385.6 m of coring (97.6% recovery).

Hole U1489D

Hole U1489D was cored to recover material for the splice over the upper ~120 mbsf that was heavily sampled for interstitial water in Hole U1489B and to collect a second copy of the deeper succession at Site U1489. The vessel was offset 20 m west of Hole U1489C, and the drill string was spaced out with the bit at 3427.0 mbrf. Hole U1489D was spudded at 0640 h on 28 November 2016, with Core 363-U1489D-1H recovering 3.69 m of sediment, establishing a seafloor depth of 3421.6 mbsl. Oriented APC coring using the Icefield MI-5 core orientation tool with nonmagnetic hardware continued to 127.2 mbsf (Cores 1H through 14H). Core 9H had a split core liner. Because several of the APCT-3 measurements provided spurious results in Hole U1489B, we opted to take additional measurements in Hole U1489D while collecting Cores 4H (32.2 mbsf), 7H (60.7 mbsf), 10H (89.2 mbsf), and 13H (117.7 mbsf). All four measurements provided good results. After collecting Core 14H, we dropped the center bit and drilled ahead without coring to 274.0 mbsf. We then cored with the XCB to 385.6 mbsf (Cores 16X through 27X), where we terminated coring. The drill string was raised to 1926.6 mbrf, and 115 ft of drill line was slipped and cut before the drill string was recovered to the vessel. Both beacons were recovered during this operation. The rig was secured for transit, and the thrusters were raised, ending operations in Hole U1489D and at Site U1489 at 0212 h on 30 November. Total time spent in Hole U1489D was 45.25 h (1.9 days).

A total of 14 APC cores were taken in Hole U1489D. We recovered 125.90 m of sediment over 127.2 m of coring for a total recovery of 99.0%. We also collected 12 XCB cores, recovering 103.34 m of sediment over 111.6 m of coring (92.6% recovery). One drilled interval advanced the hole 146.8 m without coring. Total recovery for Hole U1489D was 229.24 m of sediment over 238.8 m of coring (96.0% recovery).

Core description

Site U1489 is located at ~3421 m water depth on the western slope of Eauripik Rise in the west Caroline Basin, ~81 km westnorthwest of Site U1488. Four holes were cored at Site U1489, with the deepest penetrating to 386.33 mbsf (Hole U1489D). The recovered succession consists of lower Miocene to recent nannofossil ooze and chalk with varying proportions of clay. Biosilica (especially radiolarians) is a major component in the lowermost part of the site. The recovered succession at Site U1489 is assigned to one lithologic unit divided into two subunits defined on the basis of visual core description, microscopic examination of smear slides, magnetic susceptibility, natural gamma radiation (NGR), color spectral observations, and bulk mineralogical analysis by X-ray diffraction (XRD) (see **Core description** and **Physical properties** in the Expedition 363 methods chapter [Rosenthal et al., 2018a]). The major characteristics of the two subunits at Site U1489 are summarized in Figure **F5**.

Unit description

Unit I

Intervals: 363-U1489A-1H-1, 0 cm, through 1H-CC, 16 cm; 363-U1489B-1H-1, 0 cm, through 14H-CC, 28 cm; 363-U1489C-1H-1, 0 cm, through 42X-CC, 43 cm; 363-U1489D-1H-1, 0 cm, through 27X-CC, 23 cm

Depths: Hole U1489A = 0–9.53 mbsf, Hole U1489B = 0–129.46 mbsf, Hole U1489C = 0–384.26 mbsf, Hole U1489D = 0–386.33 mbsf

Thickness: Hole U1489A = 9.53 m, Hole U1489B = 129.46 m, Hole U1489C = 384.26 m, Hole U1489D = 386.33 m

Age: early Miocene to recent

Lithology: foraminifer-bearing clay-rich nannofossil ooze, clay-rich diatom-rich nannofossil ooze, clay-rich foraminifer-rich nannofossil ooze, clay-bearing nannofossil ash, ash, clay-bearing foraminifer-rich nannofossil ooze, foraminifer ooze, diatom-bearing foraminifer-rich nannofossil ooze, foraminifer-bearing clay-rich chalk, clay-rich foraminifer-rich chalk, foraminifer-bearing radiolarian-rich chalk, and radiolarian-rich chalk

Unit I is composed mainly of light greenish gray (5GY 8/1) foraminifer-bearing clay-rich nannofossil ooze, white (N 8.5) clay-bearing foraminifer-rich nannofossil ooze, and light greenish gray (10Y 8/1) foraminifer-bearing clay-rich chalk (Figure **F5**). The unit is divided into two subunits. Subunit IA is characterized by alternations between light greenish gray and greenish gray (5GY 6/1) foraminifer-bearing clay-rich nannofossil ooze at centimeter to meter scale (Figure **F6**). The lower part of Subunit IA contains a series of large-scale soft-sediment deformation intervals intercalated with undisturbed sediment (Figure **F7**; Table **T2**). These intervals occasionally include layers with coarser-grained foraminifer ooze or homogeneous clay-bearing foraminifer-rich nannofossil ooze. Two tephra layers are found in Subunit IA (Figure **F8**; Table **T3**). Subunit IB mainly consists of white (N 8 or 10Y 8/1) foraminifer-bearing clay-rich chalk including pale yellow (2.5Y 8/2) foraminifer-bearing radiolarian chalk in the lower part (Figure **F9**). Compared to Sub-

Figure F5. Lithologic summary, Site U1489. cps = counts per second, MS = magnetic susceptibility, SHMSL = Section Half Multisensor Logger.

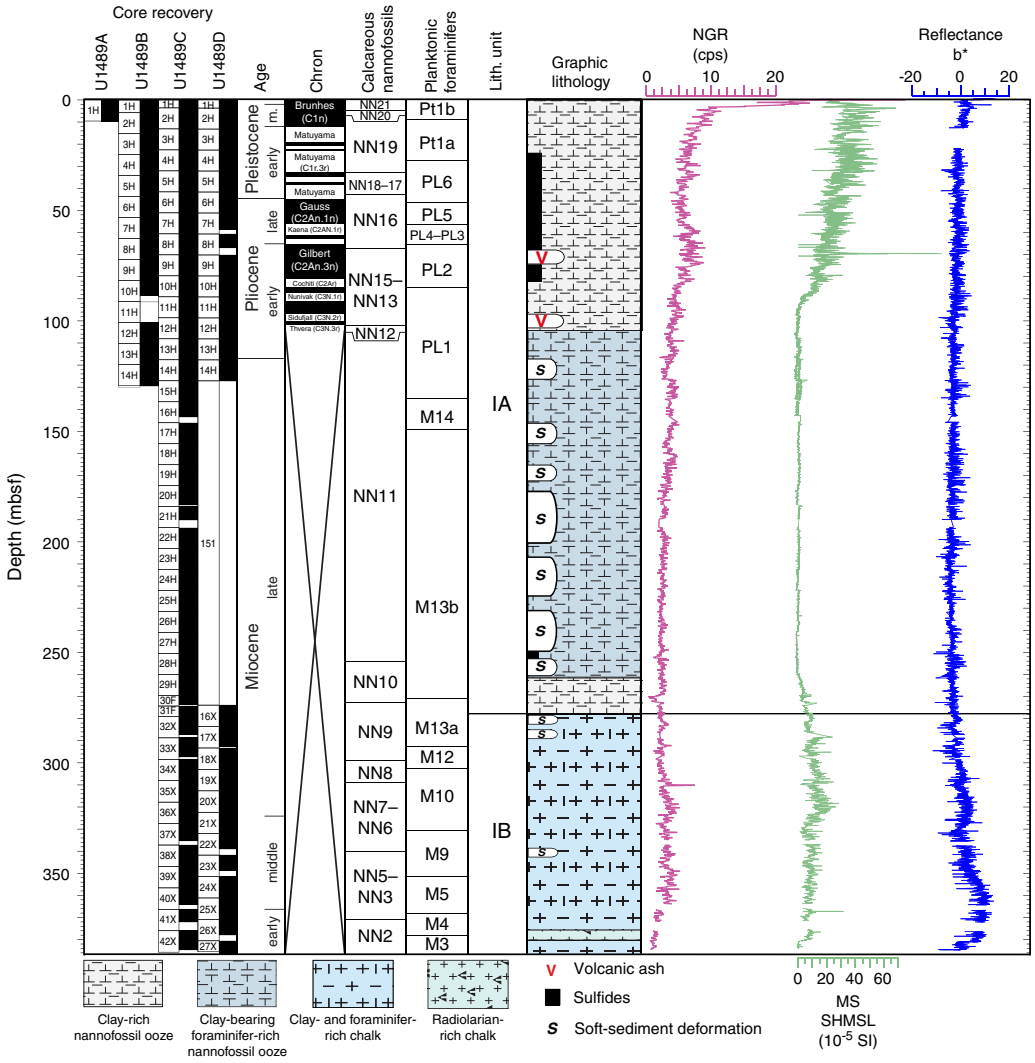

Figure F6. Color alternation in foraminifer-bearing clay-rich nannofossil ooze in Subunit IA, Site U1489. A, B. Alternation between light greenish gray and greenish gray sediment. C, D. Alternation between light greenish gray and pale yellow sediment.

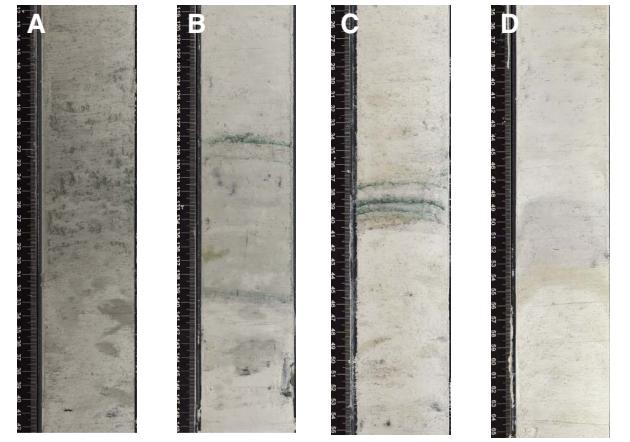

363-U1489C-4H-5A, 12–42 cm | 363-U1489C-9H-1A, 119–149 cm | 363-U1489B-6H-6A, 25–55 cm | 363-U1489C-10H-7A, 35–65 cm

Figure F7. Soft-sediment deformation in Subunit IA, Site U1489. A. Foraminifer ooze. B. Thick-bedded homogeneous sediment. C, D. Inclined layers.

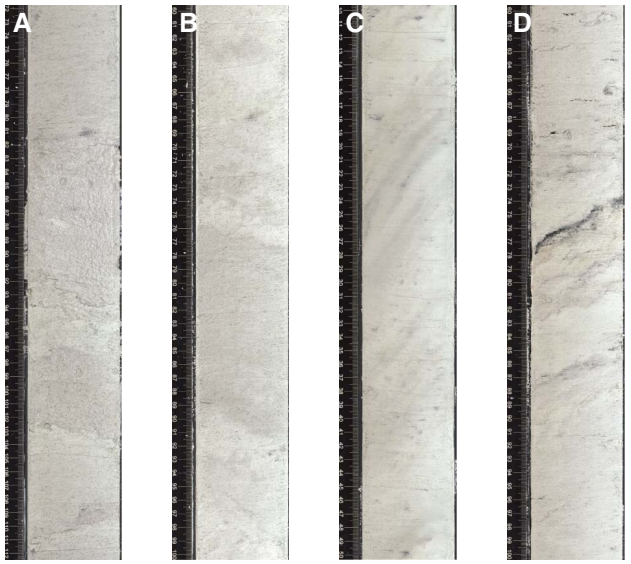

363-U1489C-13H-6A, 72–112 cm | 363-U1489C-14H-4A, 60–100 cm | 363-U1489C-17H-2A, 10–50 cm | 363-U1489C-26H-6A, 60–100 cm

Table T2. Soft-sediment deformation intervals, Hole U1489C. **Download table in CSV format.**

Top		Base		
Core, section, interval (cm)	Depth (mbsf)	Core, section, interval (cm)	Depth (mbsf)	Thickness (m)
363-U1489C-		363-U1489C-		
13H-7, 45	117.45	14H-6, 140	126.40	8.95
17H-1, 3	146.03	18H-1, 24	155.74	9.71
19H-1, 24	165.24	19H-5, 128	172.28	7.04
20H-2, 138	177.38	22H-5, 85	200.35	22.97
23H-3, 91	206.91	25H-2, 100	224.60	17.69
25H-7, 10	231.10	27H-7, 10	249.77	18.67
28H-2, 118	253.18	28H-CC, 26	260.46	7.28
32X-1, 0	278.90	32X-2, 125	281.65	2.75
32X-5, 30	285.20	33X-2, 20	289.16	3.96
38X-2, 65	339.25	38X-3, 50	342.10	2.85
42X-1, 0	375.90	42X-4, 23	380.63	4.73

Figure F8. Tephra layers, Site U1489.

363-U1489B-9H-1A, 91–97 cm | 363-U1489C-8H-7A, 28–43 cm | 363-U1489D-9H-2A, 23–35 cm

Table T3. Tephra layers, Site U1489. **Download table in CSV format.**

Top		Base		
Core, section, interval (cm)	Depth (mbsf)	Core, section, interval (cm)	Depth (mbsf)	Thickness (cm)
363-U1489B-		363-U1489B-		
9H-1, 91	73.11	9H-1, 97	73.17	6
363-U1489C-		363-U1489C-		
8H-7, 28	69.78	8H-7, 43	69.93	15
363-U1489D-		363-U1489D-		
9H-2, 23	71.99	9H-2, 35	72.05	12
12H-2, 137	101.57	12H-2, 139	101.59	2

unit IA, fewer and smaller intervals of small-scale soft-sediment deformation occur in Subunit IB (Table **T2**).

Subunit IA

Intervals: 363-U1489A-1H-1, 0 cm, through 1H-CC, 16 cm; 363-U1489B-1H-1, 0 cm, through 14H-CC, 28 cm; 363-U1489C-1H-1, 0 cm, through 32X-1, 0 cm; 363-U1489D-1H-1, 0 cm, through 14H-CC, 13 cm

Figure F9. Main lithologies in Subunit IB, Hole U1489C. A. Top of Subunit IB (32X-1, 0 cm). B. Alternation between white and light gray sediment. C. Inclined layers within soft-sediment deformation interval. D. Alternation between white and pale yellow sediment. E. Boundary of pale yellow foraminifer-bearing radiolarian-rich chalk and white foraminifer chalk.

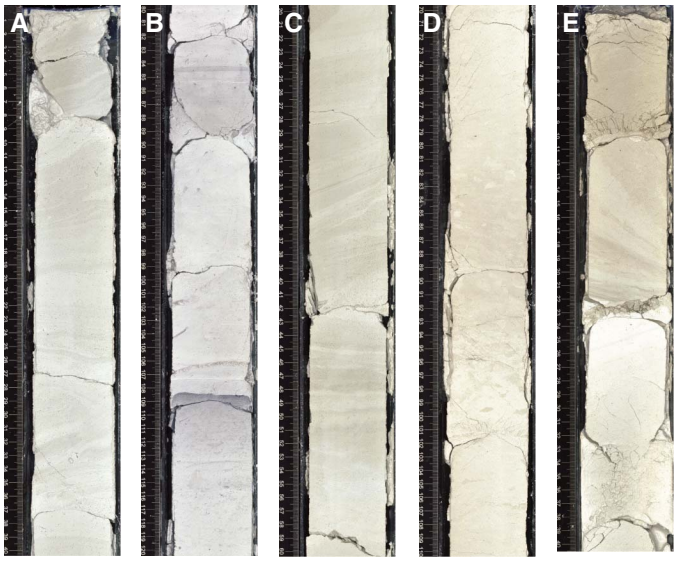

363-U1489C-32X-1A, 0–40 cm | 363-U1489C-32X-3A, 80–120 cm | 363-U1489C-38X-3A, 20–60 cm | 363-U1489D-27X-3A, 70–110 cm | U1489C-42X-4A, 0–40 cm

Depths: Hole U1489A = 0–9.53 mbsf (total depth), Hole U1489B = 0–129.46 mbsf (total depth), Hole U1489C = 0–278.90 mbsf, Hole U1489D = 0–126.98 mbsf

Thickness: Hole U1489A = 9.53 m (minimum thickness), Hole U1489B = 129.46 m (minimum thickness), Hole U1489C = 278.90 m, Hole U1489D = 126.98 m (minimum thickness)

Age: late Miocene to recent

Lithology: foraminifer-bearing clay-rich nannofossil ooze, clay-rich diatom-rich nannofossil ooze, clay-rich foraminifer-rich nannofossil ooze, clay-bearing foraminifer-rich nannofossil ooze, foraminifer ooze, diatom-bearing foraminifer-rich nannofossil ooze, clay-bearing nannofossil ash, and ash

Subunit IA is mainly composed of light greenish gray (5GY 8/1) foraminifer-bearing clay-rich nannofossil ooze. The uppermost ~35 cm consists of light brown (7.5YR 6/4) foraminifer-bearing diatom-rich nannofossil ooze. A second ~10 cm thick grayish brown foraminifer-bearing diatom-rich nannofossil ooze occurs between ~2.35 and 2.45 mbsf in all holes (Figure **F10**). These brown sediments contain abundant amounts of diatoms, sponge spicules, and silicoflagellate fragments, as well as iron oxides (Figure **F11A, F11B**). Clay minerals are most abundant in the upper part of Subunit IA and decrease downhole, which is reflected in concomitant decreases in NGR and magnetic susceptibility over the upper 100 mbsf (Figure **F5**). Below ~110 mbsf, clay minerals represent only a minor component of the sediment in Subunit IA. In the upper ~50 m of the subunit, the alternations between the darker layers, which are composed of relatively larger amounts of clay and coarser detrital minerals, and the lighter layers, which have higher abundances of nannofossils, are clearly correlated to downhole variability in both magnetic susceptibility and NGR (see **Physical properties**). The two parameters increase systematically in the darker clay-rich layers and decrease in the lighter ones.

Figure F10. Light brown foraminifer-bearing diatom-rich nannofossil ooze in Subunit IA, Site U1489. A. Thick-bedded light brown sediment. B. Thin-bedded light brown sediment.

363-U1489B-1H-1A, 0–40 cm

363-U1489D-1H-3A, 5–45 cm

Figure F11. Sedimentary components in two of the primary lithologies, Site U1489. D = diatom, Sp = sponge spicule, Sf = silicoflagellate, R = radiolarian. A, B. Light brown foraminifer-bearing diatom-rich nannofossil ooze. C, D. Pale yellow clay-rich foraminifer-rich chalk.

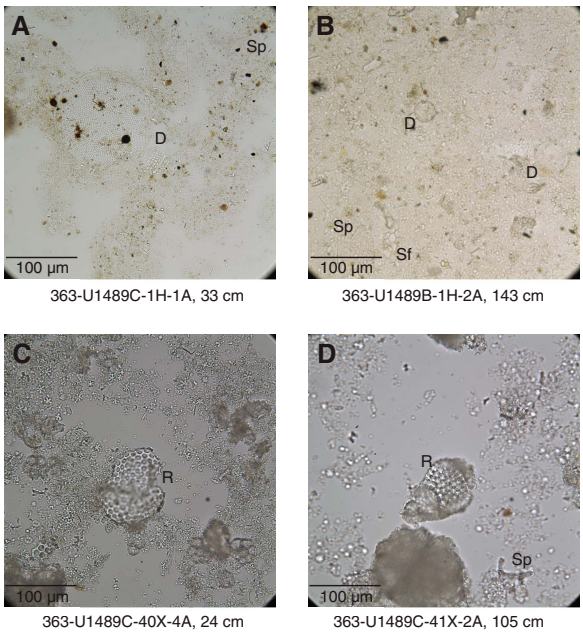

363-U1489C-1H-1A, 33 cm

363-U1489B-1H-2A, 143 cm

363-U1489C-40X-4A, 24 cm

363-U1489C-41X-2A, 105 cm

Subunit IA is also characterized by extensive color banding due to the alternation between layers having different colors. For example, thin-bedded (less than ~5 cm thick) pale yellow layers alternate with light greenish gray layers, and grayish green layers alternate with pale purplish layers (Figure **F6**). Coarser-bedded centimeter- to meter-scale alternations between light greenish gray and greenish gray (5GY 6/1) foraminifer-rich clay-rich nannofossil ooze occur throughout much of the subunit (Figure **F6**). Color variations (light greenish gray, greenish gray, and pale yellow) in the sediment are associated with variations in magnetic susceptibility and NGR values. Greenish gray sediment has higher magnetic susceptibility and higher NGR (6.5 counts/s) values (Figure **F12A**) than pale yellow sediment (NGR = 5.6–6.0 counts/s) (Figure **F12B**), whereas white and pale yellow sediments exhibit very low magnetic susceptibility and NGR (4.4–4.7 counts/s) values (Figure **F12C**). XRD analysis of samples from these different-colored layers indicates that they have similar mineral compositions but in slightly different proportions depending on the sediment color (Figure **F13**). For instance, the light greenish and greenish gray sediment has higher clay mineral content compared with the grayish green sediment.

Two tephra layers were found in Subunit IA (Figure **F8**; Table **T3**). One tephra layer with very high magnetic susceptibility values occurs between 70 and 73 mbsf in Holes U1489B–U1489D (Figure **F5**). The other tephra layer was only found between 137 and 139 mbsf in Hole U1489D. These tephra layers mainly consist of glass shards and are slightly bioturbated.

The lower part of Subunit IA is characterized by large-scale soft-sediment deformation (Figure **F7**). The deformed sediment contains predominantly inclined layers, microfaults, and fluid escape structures. These intervals are frequently accompanied by very thick bedded homogeneous sediment (Figure **F7B**) or coarse-grained foraminifer ooze (Figure **F7A**). Intervals of soft-sediment deformation found in Hole U1489C are listed in Table **T2**. The soft-sediment deformation intervals correspond to high *P*-wave velocity (see **Physical properties**). The top of Subunit IB is recognized by the first appearance of chalk at intervals 363-U1489D-32X-1, 0 cm (278.9 mbsf), and 16X-1, 0 cm (274.0 mbsf) (Figure **F9A**).

Subunit IB

Intervals: 363-U1489C-32X-1, 0 cm, through 42X-CC, 43 cm; 363-U1489D-16X-1, 0 cm, through 27X-CC, 23 cm
Depths: Hole U1489C = 278.90–384.26 mbsf, Hole U1489D = 274.0–386.33 mbsf
Thickness: Hole U1489C = 105.36 m, Hole U1489D = 112.33 m
Age: early Miocene to late Miocene
Lithology: foraminifer-bearing clay-rich chalk, clay-rich foraminifer-rich chalk, foraminifer-bearing radiolarian-rich chalk, and radiolarian-rich chalk

Subunit IB is mainly composed of light greenish gray (10Y 8/1) foraminifer-bearing clay-rich chalk and clay-rich foraminifer-rich chalk, pale yellow (2.5Y 8/3) foraminifer-bearing radiolarian-rich chalk, and light gray (5Y 7/2) radiolarian-rich chalk (Figures **F9**, **F11C, F11D**). Alternations between white and light gray (N 7) foraminifer-bearing clay-rich chalk occur at centimeter to meter scale in Cores 363-U1489C-32X through 37X and in Cores 363-U1489D-16X through 23X (Figure **F9B**). The light gray sediment is characterized by millimeter-scale laminae with sharp upper and lower boundaries. Various types of burrows are common in the lighter sediment. White (N 9) foraminifer-bearing clay-rich chalk gradually changes downhole to pale yellow (2.5Y 8/2) foraminifer-bearing clay-rich chalk starting from Cores 363-U1489C-37X and 363-U1489D-24X. Pale yellow foraminifer-bearing clay-rich chalk changes to pale yellow foraminifer-bearing radiolarian-rich chalk in Core 363-U1489C-42X. The lower boundary of pale yellow foraminifer-bearing radiolarian-rich chalk is marked by an abrupt change to white sediment (N 8.5) at interval 363-U1489C-42X-4, 23 cm (Figure **F9E**).

Figure F12. Comparison of MS and NGR in different colored sediments of Subunit IA, Site U1489. cps = counts per second. A. Light greenish gray and greenish gray. B. Light greenish gray and pale yellow. C. White.

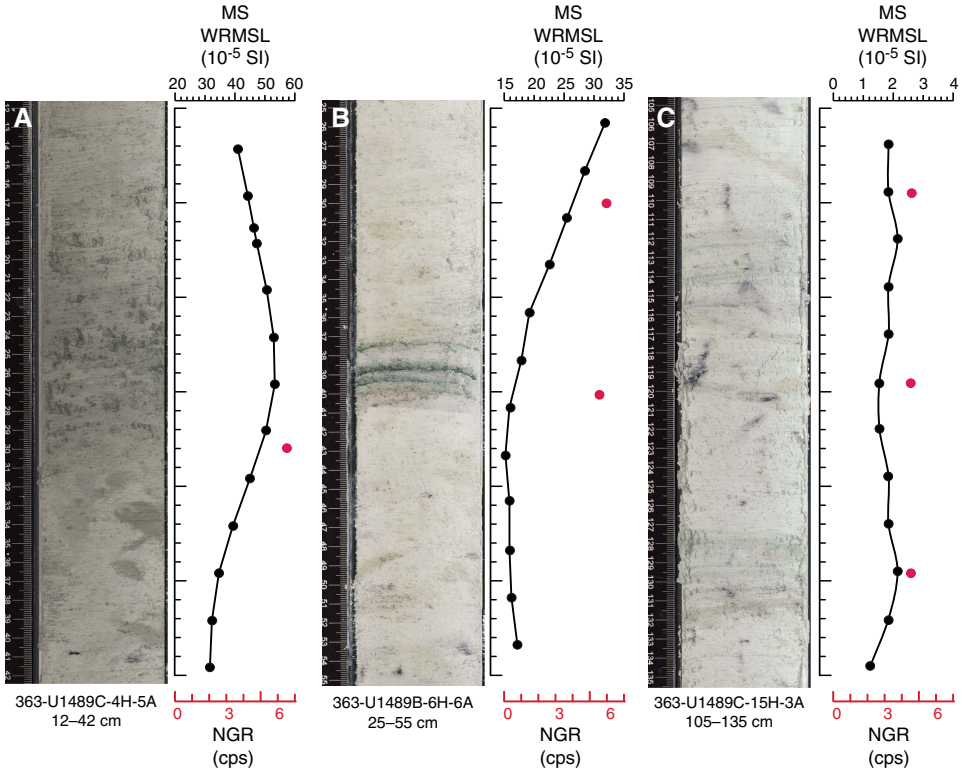

Figure F13. Core image with XRD results from different colored sediment in Subunit IA, Site U1489.

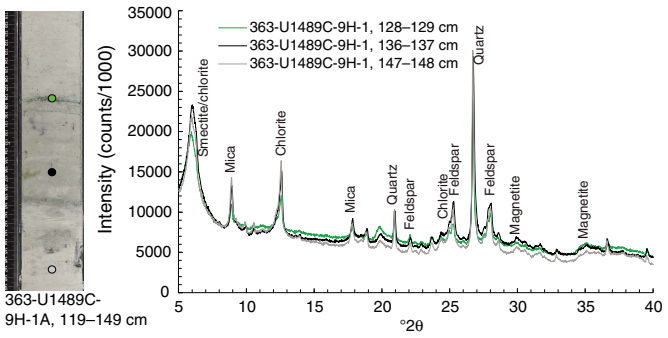

Subunit IB is characterized by small-scale soft-sediment deformation and alternations between light and dark foraminifer-bearing clay-rich chalk and clay-rich foraminifer-rich chalk (Figure **F9**). The soft-sediment deformation intervals contain inclined and convolute layers and microfaults. The intervals in which we identified soft-sediment deformation in Hole U1489C are summarized in Table **T2**.

Discussion

Cyclic sedimentation and soft-sediment deformation

Subunit IA is characterized by decimeters-thick alternations between darker and lighter greenish gray sediment layers. The darker layers are composed of relatively larger amounts of clay minerals (smectite and chlorite) and detrital minerals (quartz, feldspar, mica, and magnetite) compared with the lighter layers, which have higher abundances of nannofossils. These alternations suggest cyclic changes in the supply of fine-grained terrigenous sediments and, given the open-ocean setting of the site, could reflect changes in strength/importance of eolian input to the site. Alternatively, the cyclic variations in siliciclastic content could be a diagenetic feature due to carbonate dissolution. The greenish gray sediment is only present in the upper ~80–90 mbsf of the site and corresponds to clay-rich nannofossil ooze. The disappearance of this greenish gray clay-rich sediment corresponds to a drop in NGR and magnetic susceptibility below ~90 mbsf (Figure **F5**). This decrease in clay content, NGR, and magnetic susceptibility in the upper part of the sedimentary section at Site U1489 is similar to that seen at Site U1488 (see **Comparison to Site U1488** below).

The lower part of Subunit IA is characterized by frequent soft-sediment deformation. The total thickness of the soft-sediment deformation interval is ~85 m (Table **T2**) in Hole U1489C. In the lower part of Subunit IA (117–253 mbsf), sedimentation rates abruptly increase from ~2 to ~5 cm/ky (see **Biostratigraphy**). The increased sediment accumulation rates in this interval may be due to the following factors:

- The addition of sediment as a result of the deformation process (i.e., slumping),
- Changes in postdepositional alteration and dissolution of primary sediments, or
- A combination of factors.

Sediment deformation can also be triggered by excess pore fluid pressure with enhanced supply of coarse-grained sediment (Mills, 1983). Higher sediment supply during deposition can act as a trigger for a gravitational slump. The soft-sediment deformation in

Subunit IB is much smaller in scale than in Subunit IA and constitutes only ~14 m of section (Table **T2**).

Comparison to Site U1488

Sites U1488 and U1489 show several similarities but also differences that reflect their depositional settings and postdepositional histories. Site U1489 is located at ~3421 m water depth on the western flank of Eauripik Rise, ~81 km west-northwest of Site U1488, which is located at shallower water depth (~2604 mbsl) on the top of the rise. The total recovered sediment thickness at Sites U1488 and U1489 is ~314.5 and ~386.33 mbsf, respectively. The two sites are characterized by different sedimentation rates, possibly because of differences in sedimentary processes and/or differences in the postdepositional history (including both dissolution and lithification). Site U1488 mainly consists of clay-rich foraminifer-rich nannofossil ooze, foraminifer-bearing nannofossil ooze, and radiolarian-bearing foraminifer-nannofossil ooze, indicating pelagic sedimentation from the late Miocene to recent. The sediments at Sites U1488 and U1489 are generally similar; however, Site U1489 exhibits higher clay mineral content and detrital components in the lower Pliocene to Pleistocene interval, whereas at Site U1488 the interval with higher clay content is restricted to the Pleistocene. Downhole trends in magnetic susceptibility and NGR are also similar between sites (cf. Figure **F5** in the Site U1488 chapter [Rosenthal et al., 2018c] and Figure **F5**). However, the depth at which the two physical property records decrease is different. This depth is shallower at Site U1488 and corresponds to the drop in clay content in the sediment. One tephra layer with high magnetic susceptibility and platy glass shards was found at ~92 mbsf at Site U1488 and ~73 mbsf at Site U1489. These tephra layers can be correlated to a tephra layer reported from DSDP Site 62 on the Eauripik Rise (interval 7-62-10H-5, 137–143 cm; 98 mbsf) (Shipboard Scientific Party, 1971).

A key difference between sites is the extensive occurrence of soft-sediment deformation in the middle part of Site U1489 that is absent at Site U1488. The location of Site U1489 on the slope of the Eauripik Rise likely played a role in the development of soft-sediment deformation, whereas Site U1488 is in a more stable setting at the top of this physiographic feature. Another major difference is the shift from nannofossil ooze to chalk at Site U1489 (~278 mbsf; top of Subunit IB), whereas at Site U1488 chalk was not recovered at that depth or to the bottom of the site at ~308 mbsf.

Greenish layers and bands of different colors, which are interpreted as indicators of early diagenesis influenced by differences in clay mineral content, and small compositional differences in biogenic content (see **Core description** in the Site U1488 chapter [Rosenthal et al., 2018c]), are common features at both sites.

Biostratigraphy

We cored a 385 m thick succession of clay-bearing foraminifer-rich nannofossil ooze at Site U1489 (see **Core description**). Calcareous microfossil assemblages and preservation are typical of a pelagic, relatively deep water bathyal environment throughout the recorded succession. Biostratigraphic results from each fossil group (calcareous nannofossils, planktonic foraminifers, and benthic foraminifers) are presented in the sections below, followed by a detailed characterization of benthic and planktonic foraminifer preservation state using the shipboard scanning electron microscope (SEM). An integrated bio- and magnetostratigraphy and preliminary age model are presented in the final section. Shipboard taxon occurrence data are available for download from the IODP Laboratory Information Management System (LIMS) database (**http://web.iodp.tamu.edu/LORE/**).

Calcareous nannofossils

Calcareous nannofossil biostratigraphy is based primarily on Hole U1489C, from which core catcher (CC) samples and two or three samples per core were taken, providing ~3 m resolution. Depth positions and age estimates of biohorizons are given in Table **T4**. Observations were undertaken using plane- (PPL), cross- (XPL), and circular-polarized light (CPL), as well as the shipboard desktop SEM (Hitachi TM3000) to confirm the presence of *Emiliania huxleyi* and to check preservation state.

At Site U1489, the preservation of calcareous nannofossils is generally very good, becoming moderate deeper than 280 mbsf (Figures **F14**, **F15**). Below that depth, discoasters show significant traces of overgrowth, with complete recrystallization deeper than 350 mbsf as evidenced by high birefringence. However, the placoliths, helicoliths, and sphenoliths are surprisingly well preserved in the same interval that discoasters are poorly preserved. Intact coccospheres are observed sporadically throughout Hole U1489C. Reworked calcareous nannofossils occur very rarely, such as occasional specimens of *Cyclicargolithus, Discoaster,* and *Sphenolithus*, especially in the upper part of the hole.

Pleistocene

The Pleistocene stratigraphy is well constrained by 10 calcareous nannofossil biohorizons (Table **T4**). Because of the low sedimentation rates at Site U1489 and the shipboard sampling resolution, biohorizons corresponding to abundance fluctuations of certain taxa (e.g., *E. huxleyi* and *Gephyrocapsa caribbeanica*) were not observed in the samples. Biohorizon base *E. huxleyi* (0.29 Ma; base of Zone NN21) occurs between Samples 363-U1489C-1H-CC and 2H-2, 60 cm (3.54–5.60 mbsf), and biohorizon top *Pseudoemiliania lacunosa* (0.44 Ma; base of Zone NN20) between Samples 2H-2, 60 cm, and 2H-4, 60 cm (5.60–8.60 mbsf). The Brunhes/Matuyama boundary (0.781 Ma) is located at 11.93 mbsf (see **Paleomagnetism**), which is below biohorizon top *Reticulofenestra asanoi* (0.91 Ma) between Samples 2H-4, 60 cm, and 2H-6, 60 cm (8.60–11.60 mbsf), and thus not in the expected order.

The base of Zone NN19 is defined by biohorizon top *Discoaster brouweri* (1.93 Ma) between Samples 363-U1489C-4H-CC and 5H-2, 60 cm (32.34–34.10 mbsf), at the same level as biohorizon top *Discoaster triradiatus* (1.95 Ma). Biohorizons top *Discoaster pentaradiatus* (2.39 Ma; base of Zone NN18) and top *Discoaster surculus* (2.49 Ma; base of Zone NN17) are both observed between Samples 5H-CC and 6H-2, 60 cm (41.61–43.60 mbsf). The Matuyama/Gauss boundary (2.581 Ma) is identified at 44.81 mbsf (see **Paleomagnetism**). This lies between the biohorizon top *D. surculus* and biohorizon top *Discoaster tamalis* (2.80 Ma) between Samples 6H-4, 60 cm, and 6H-6, 60 cm (46.60–49.60 mbsf).

Pliocene

Seven nannofossil biohorizons are identified in the Pliocene interval. Biohorizon top *Sphenolithus abies* (3.54 Ma) occurs between Samples 363-U1489C-8H-2, 60 cm, and 8H-4, 60 cm (62.60–65.60 mbsf). The base of Zone NN16 is defined by the biohorizon top *Reticulofenestra pseudoumbilicus* (3.70 Ma) between Samples 8H-4, 60 cm, and 8H-6, 60 cm (65.60–68.60 mbsf). *Amaurolithus tricorniculatus*, whose biohorizon top (3.92 Ma) defines the base of Zone NN15, was only observed in one sample (11H-6, 60 cm; 97.10 mbsf). As a result, Zone NN15 is difficult to recognize in Hole

Table T4. Calcareous nannofossil bioevents, Site U1489. B = base, T = top, Bc = base common, Tc = top common, Bpa = base paracme. **Download table in CSV format.**

Bioevent number	Marker species	Age (Ma)	Zone base	Top core, section, interval (cm)	Bottom core, section, interval (cm)	Top depth (mbsf)	Bottom depth (mbsf)	Midpoint depth (mbsf)	± (m)
				363-U1489C-	363-U1489C-				
3	B *Emiliania huxleyi*	0.29	NN21	1H-CC	2H-2, 60	3.54	5.60	4.57	1.03
4	T *Pseudoemiliania lacunosa*	0.44	NN20	2H-2, 60	2H-4, 60	5.60	8.60	7.10	1.50
6	T *Reticulofenestra asanoi*	0.91		2H-4, 60	2H-6, 60	8.60	11.60	10.10	1.50
8	T *Gephyrocapsa* >5.5 µm	1.25		3H-6, 90	3H-CC	21.40	22.85	22.13	0.73
9	T *Helicosphaera sellii*	1.26		3H-CC	4H-2, 60	22.85	24.60	23.73	0.88
10	T *Calcidiscus macintyrei*	1.60		4H-2, 60	4H-4, 60	24.60	27.60	26.10	1.50
11	T *Discoaster brouweri*	1.93	NN19	4H-CC	5H-2, 60	32.34	34.10	33.22	0.88
	T *Discoaster triradiatus*	1.95		4H-CC	5H-2, 60	32.34	34.10		
14	T *Discoaster pentaradiatus*	2.39	NN18	5H-CC	6H-2, 60	41.61	43.60	42.61	1.00
15	T *Discoaster surculus*	2.49	NN17	5H-CC	6H-2, 60	41.61	43.60	42.61	1.00
	Pliocene/Pleistocene boundary	2.58							
16	T *Discoaster tamalis*	2.80		6H-4, 60	6H-6, 60	46.60	49.60	48.10	1.50
17	T *Sphenolithus* spp.	3.54		8H-2, 60	8H-4, 60	62.60	65.60	64.10	1.50
18	T *Reticulofenestra pseudoumbilicus*	3.70	NN16	8H-4, 60	8H-6, 60	65.60	68.60	67.10	1.50
19	T *Amaurolithus tricorniculatus* (/*delicatus*)	3.92	NN15	11H-4, 60	11H-6, 60	94.10	97.10	95.60	1.50
23	T *Ceratolithus armatus*	5.04		12H-2, 60	12H-4, 60	100.60	103.60	102.10	1.50
24	B *Ceratolithus cristatus*	5.12	NN13–NN14	12H-2, 60	12H-4, 60	100.60	103.60	102.10	1.50
25	T *Orthostylus rugosus*	5.28		13H-4, 60	13H-6, 60	113.10	116.10	114.60	1.50
	Miocene/Pliocene boundary	5.33							
27	B *Ceratolithus armatus*	5.35		13H-CC	14H-2, 61	117.95	119.61	118.78	0.83
28	T *Discoaster quinqueramus*	5.59	NN12	12H-4, 60	12H-6, 60	103.60	106.60	105.10	1.50
29	T *Nicklithus amplificus*	5.98		16H-3, 41	16H-CC	139.96	143.41	141.69	1.72
30	B *Nicklithus amplificus*	6.91		19H-6, 61	19H-CC	173.11	174.46	173.79	0.67
31	B *Amaurolithus* spp.	7.42		23H-CC	24H-CC	212.84	222.41	217.63	4.78
34	B *Discoaster quinqueramus*	8.12		27H-CC	28H-2, 60	250.55	252.60	255.00	1.02
35	B *Discoaster berggrenii*	8.29	NN11	28H-2, 60	28H-4, 60	252.60	255.60	254.10	1.50
38	Bpa *Reticulofenestra pseudoumbilicus*	8.79		29H-4, 60	29H-6, 60	265.10	268.10	266.60	1.50
40	Bc *Discoaster pentaradiatus*	9.37		30F-3, 60	30F-CC	271.31	273.54	272.43	1.12
41	T *Discoaster hamatus*	9.53	NN10	30F-3, 60	30F-CC	271.31	273.54	272.43	1.12
42	T *Catinaster calyculus*	9.67		30F-3, 60	30F-CC	271.31	273.54	272.43	1.12
43	T *Catinaster coalitus*	9.69		30F-CC	31F-CC	273.54	279.11	276.33	2.78
46	B *Discoaster neohamatus*	10.52		32X-CC	33X-CC	287.06	297.82	292.44	5.38
47	B *Discoaster hamatus*	10.55	NN9	33X-CC	34X-2, 75	297.82	300.55	299.19	1.37
48	T *Coccolithus miopelagicus*	10.61		34X-6, 60	34X-CC	306.40	307.97	307.19	0.79
49	Bc *Helicosphaera stalis*	10.71		35X-2, 75	35X-4, 75	310.25	313.25	311.75	1.50
50	Tc *Helicosphaera walbersdorfensis*	10.74		35X-2, 75	35X-4, 75	310.25	313.25	311.75	1.50
51	B *Discoaster brouweri*	10.76		34X-CC	35X-CC	307.97	317.58	312.78	4.80
52	B *Catinaster calyculus*	10.79		33X-CC	34X-2, 75	297.82	300.55	299.19	1.37
53	B *Catinaster coalitus*	10.89	NN8	34X-CC	35X-2, 75	307.97	310.25	309.11	1.14
54	T *Calcidiscus premacintyrei*	11.241		37X-5, 75	37X-CC	334.15	334.79	334.47	0.32
57	T *Cyclicargolithus floridanus*	12.07		37X-5, 75	37X-CC	334.15	334.79	334.47	0.32
58	T *Coronocyclus nitescens*	12.12		37X-CC	38X-2, 40	334.79	339.00	336.90	2.10
60	B *Orthorhabdus rugosus*	13.27		38X-2, 40	38X-4, 40	339.00	342.00	340.50	1.50
61	Tc *Cyclicargolithus floridanus*	13.28		39X-2, 75	39X-4, 75	349.05	352.05	350.55	1.50
62	T *Sphenolithus heteromorphus*	13.53	NN6	38X-2, 40	38X-4, 40	339.00	342.00	340.50	1.50
64	Tc *Discoaster deflandrei* group	15.80		40X-2, 75	40X-4, 75	358.75	361.75	360.25	1.50
67	B *Sphenolithus heteromorphus*	17.71		41X-CC	42X-3, 60	371.98	379.50	375.74	3.76
68	T *Sphenolithus belemnos*	17.95	NN4	41X-3, 100	41X-CC	370.20	371.98	371.09	0.89
69	T *Triquetrorhabdulus carinatus*	18.28	NN3	41X-3, 100	41X-CC	370.20	371.98	371.09	0.89
70	B *Sphenolithus belemnos*	19.03		42X-4, 20	42X-4, 30	380.60	380.70	380.65	0.05

U1489C, similar to Site U1488, where Zones NN13–NN15 are undifferentiated (see **Biostratigraphy** in the Site U1488 chapter [Rosenthal et al., 2018c]). Biohorizon base *Ceratolithus cristatus* (5.12 Ma), which defines the base of Zone NN13–NN14, occurs between Samples 12H-2, 60 cm, and 12H-4, 60 cm (100.60–103.60 mbsf).

Miocene

The stratigraphy of the Miocene is constrained by 32 calcareous nannofossil biohorizons (Table **T4**). The Miocene/Pliocene boundary (5.33 Ma) is located just above biohorizon base *Ceratolithus armatus* (5.35 Ma), which occurs between Samples 363-U1489C-13H-CC and 14H-2, 61 cm (117.95–119.61 mbsf). Zone NN12 is problematic because the marker that defines its base, biohorizon top *Discoaster quinqueramus* (5.59 Ma), occurs between Samples 12H-4, 60 cm, and 12H-6, 60 cm (103.60–106.60 mbsf), which is well above the biohorizon base of *Ceratolithus armatus*, and therefore in the Pliocene. This may be due to reworking related to the uppermost of several intervals of disturbed sediment observed between 105 and 175 mbsf (see **Core description**). Planktonic foraminifers also show evidence of reworking at this level pointing to

Figure F14. Calcareous nannofossils, Site U1489 (XPL). A. *Calcidiscus leptoporus* (U1489C-1H-CC). B, C. *Cyclicargolithus floridanus* (B: U1489C-38X-6, 40 cm; C: 41X-CC). D. *Coccolithus pelagicus* (U1489C-4H-CC). E. *Coronocyclus nitescens* (U1489C-42X-4, 30 cm). F. *Gephyrocapsa* >5.5 µm (U1489B-3H-CC). G, H. *Pseudoemiliania lacunosa* (G: U1489B-2H-6, 75 cm; H: U1489C-2H-6, 60 cm). I. *Reticulofenestra asanoi* (U1489C-2H-CC). J. *Reticulofenestra pseudoumbilicus* (U1489B-10H-CC). K. *Ceratolithus cristatus* (U1489B-3H-CC). L. *Helicosphaera* sp. (U1489B-3H-CC). M. *Helicosphaera granulata* (U1489C-19H-CC). N. *Minylitha convallis* (U1489C-29H-CC). O. *Triquetrorhabdulus carinatus* (U1489C-41X-CC). P. *Scyphosphaera tubifera* (U1489C-38X-6, 40 cm). Q. *Scyphosphaera pulcherrima* (U1489B-5H-CC). R. *Sphenolithus belemnos* (U1489C-41X-CC). S, T. *Sphenolithus heteromorphus* (S: U1489C-41X-CC; T: U1489C-38X-4, 40 cm). All photos are at same magnification (scale bar in A).

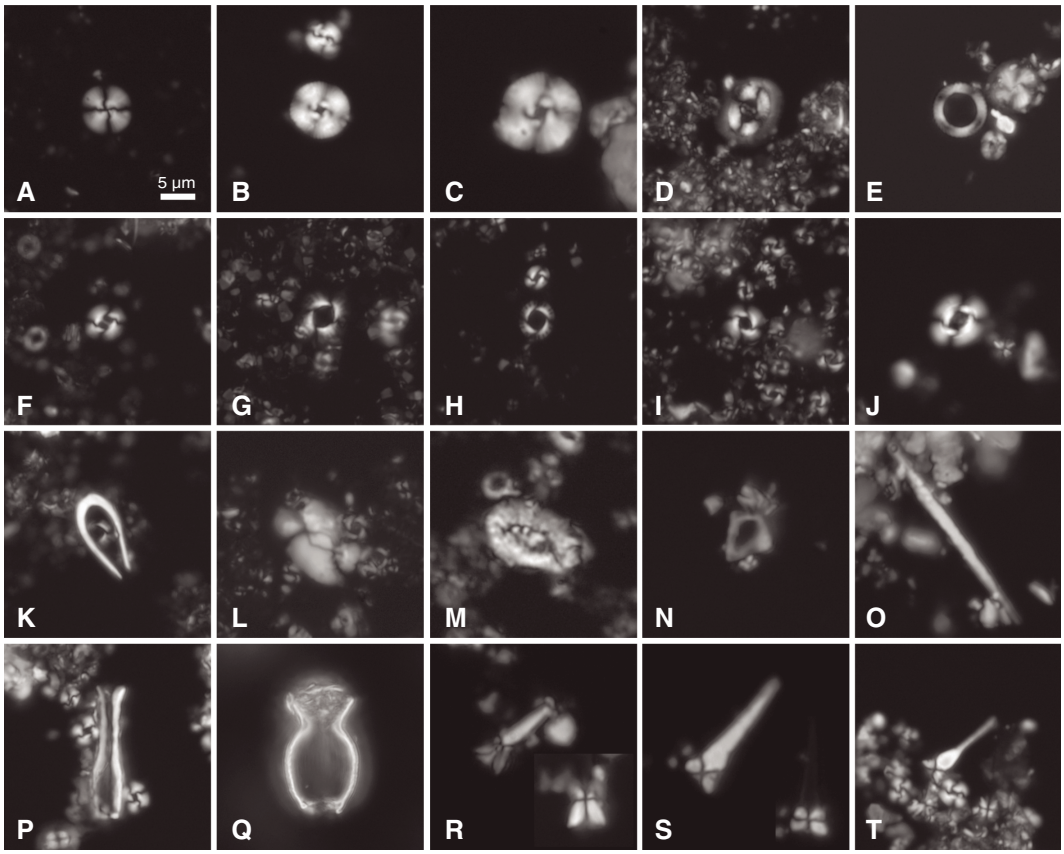

possible sedimentary redeposition. Below this level, biohorizons are in their expected stratigraphic order.

The base of Zone NN11 is defined by biohorizon base *Discoaster berggrenii* (8.29 Ma) between Samples 363-U1489C-28H-2, 60 cm, and 28H-4, 60 cm (252.60–255.60 mbsf). The base of Zone NN10 is defined by biohorizon top *Discoaster hamatus* (9.53 Ma) between Samples 30F-3, 60 cm, and 30F-CC (271.31–273.54 mbsf), which occurs at the same level as biohorizons base common *D. pentaradiatus* (9.37 Ma) and top *Catinaster calyculus* (9.66 Ma). The base of Zone NN9 is defined by biohorizon base *D. hamatus* (10.55 Ma) between Samples 33X-CC and 34X-2, 75 cm (297.82–300.55 mbsf). Biohorizon base *Catinaster coalitus* (10.89 Ma), which defines the base of Zone NN8, was observed between Samples 34X-CC and 35X-2, 75 cm (307.97–310.25 mbsf). Biohorizon base common *Discoaster kugleri* (11.90 Ma), which marks the base of Zone NN7 near the middle/upper Miocene boundary, is not recognized in Hole U1489C. Although *D. kugleri* specimens were observed in Samples 35X-CC (317.58 mbsf) and 36X-CC (327.18 mbsf), the preservation state of discoasters below makes identification to species level difficult.

The middle Miocene biohorizon top *Sphenolithus heteromorphus* (13.53 Ma) occurs between Samples 363-U1489C-38X-2, 40 cm, and 38X-4, 40 cm (339.00–342.00 mbsf), and marks the base of Zone NN6. The base of Zone NN4 is defined by biohorizon top *Sphenolithus belemnos* (17.95 Ma) between Samples 41X-3, 100 cm, and 41X-CC (370.20–371.98 mbsf). Zone NN5 was not recognized in Hole U1489C due to the absence of *Helicosphaera ampliaperta*, whose biohorizon top (14.91 Ma) marks the base of the zone. Biohorizon top *Triquetrorhabdulus carinatus* (18.28 Ma), which defines the base of Zone NN3, occurs in the same level as *S. belemnos*. The stratigraphy of the base of Hole U1489C is constrained by biohorizon base *S. belemnos* (19.03 Ma) between Samples 42X-4, 20 cm, and 42X-4, 30 cm (380.60–380.70 mbsf).

Planktonic foraminifers

Planktonic foraminifers are diverse and abundant throughout the succession at Site U1489. Preservation is generally very good (although sometimes quite fragmented) from the seafloor downhole to ~270 mbsf. Below that depth, sample processing was difficult because the sediment is hard and cemented, and preservation varies from poor (heavily cemented) to good (mostly free of infilling). More detailed observations are described in **Foraminifer preservation**.

Biostratigraphy was conducted on three sample sets:

1. All core catcher samples from Hole U1489B,
2. All core catcher samples from Hole U1489C supplemented by up to three additional samples per core from Cores 363-U1489C-13H through 31F, and

Figure F15. Calcareous nannofossils, Site U1489 (PPL). A. *Amaurolithus primus* (U1489C-22H-CC). B. *Amaurolithus delicatus* (U1489C-23H-CC). C–E. *Nicklithus amplificus* (U1489B-12H-CC). F. *Orthorhabdus rugosus* (U1489B-12H-CC). G. *Catinaster calyculus* (U1489C-30F-CC). H. *Discoaster triradiatus* (U1489B-10H-CC). I. *Discoaster tamalis* (U1489B-6H-CC). J. *Discoaster brouweri* (U1489B-5H-CC). K, L. *Discoaster quinqueramus* (U1489C-24H-CC). M. *Discoaster berggrenii* (U1489B-14H-CC). N–P. *Discoaster variabilis* (N, O: U1489B-12H-CC; P: U1489C-25H-CC). Q, R. *Discoaster neohamatus* (Q: U1489B-14H-CC; R: U1489C-28H-CC). S, T. *Discoaster surculus* (U1489B-12H-CC). All photos are at same magnification (scale bar in A).

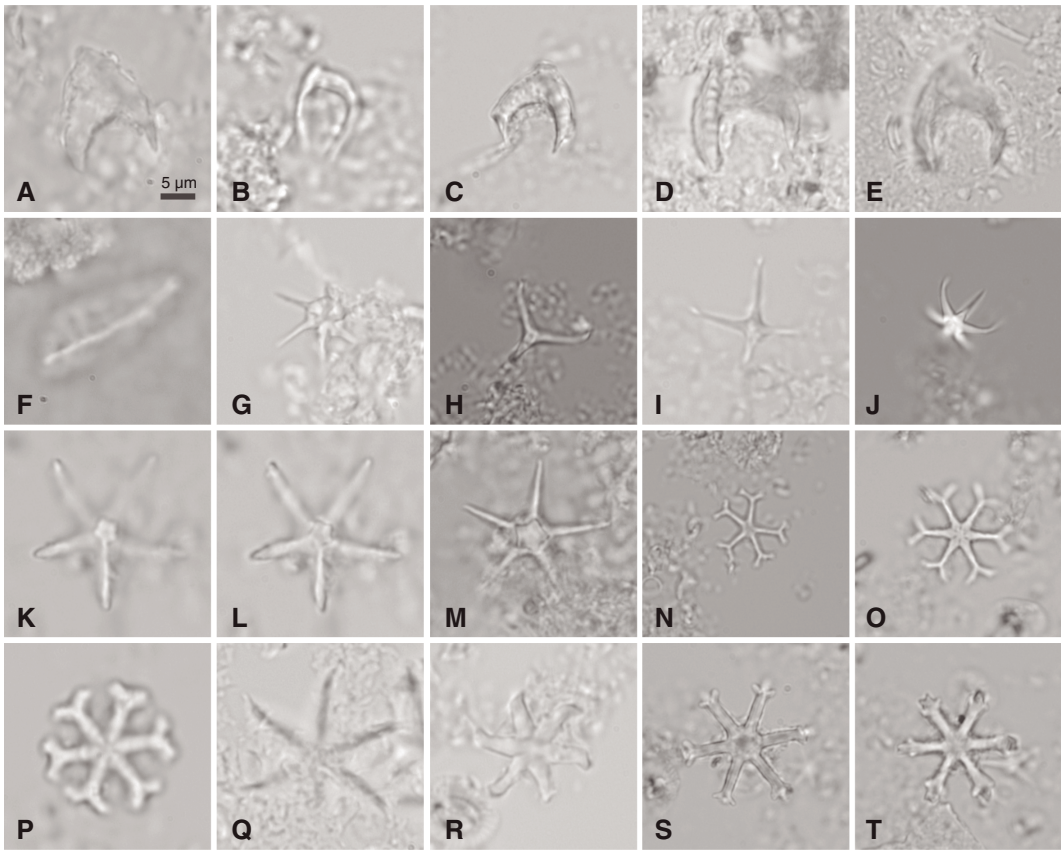

3. Core catcher samples from Cores 363-U1489D-16X through 27X.

Lists of biohorizons for these intervals are presented in Table **T5**. Here we focus on the record from Hole U1489C with additional observations from the other holes added where appropriate.

The topmost sample examined, Sample 363-U1489C-1H-CC (3.54 mbsf) contains *Globorotalia flexuosa, Globigerinoides ruber* (pink), and *Globigerinella calida* and is assigned to the upper part of Subzone Pt1b, between 0.12 and 0.22 Ma. These species are absent from Sample 2H-CC (13.31 mbsf), which contains *Globorotalia tosaensis* and is assigned to Subzone Pt1a (0.61–1.88 Ma).

Coiling directions in *Pulleniatina* were measured at low resolution (only core catchers were examined) in Holes U1489B and U1489C from the top of the hole to below the level of Saito's (1976) L9 excursion. Data are given in Table **T6** and plotted in Figure **F16**. The uppermost two samples in both holes contain predominantly dextral *Pulleniatina*. The L1 coiling change excursion (0.80 Ma) is observed between Samples 363-U1489C-2H-CC and 3H-CC (13.31–22.85 mbsf).

Biohorizon top *Globigerinoidesella fistulosa* (1.88 Ma), which marks the base of Subzone Pt1a, occurs between Samples 363-U1489C-3H-CC and 4H-CC (22.90–32.34 mbsf). At some levels at Site U1489, *G. fistulosa* has quite extreme morphologies, including forms with up to four distinctly fistulose (i.e., having hollow, pipe-like extensions) chambers; up to nine distinct protuberances on a single chamber; and/or unusually long, branching, or crenulated protuberances (Figure **F17**). Detailed study of these variations might provide future biostratigraphic potential if fully documented.

Biohorizon top *Globorotalia pseudomiocenica* (2.30 Ma), which marks the base of Zone PL6, is identified on the basis of just two individuals in Sample 363-U1489C-6H-CC (51.40 mbsf). This biohorizon occurs above biohorizon top *Globorotalia limbata* (calibrated at 2.39 Ma, which is probably slightly too old) between Samples 6H-CC and 7H-CC. Two additional events occur between the same samples: biohorizons top *Dentoglobigerina altispira* (3.13 Ma), which marks the base of Zone PL5, and base *G. fistulosa* (3.33 Ma).

Biohorizon top *Sphaeroidinellopsis seminulina* (3.59 Ma), which marks the base of Zone PL4, and biohorizon top *Globorotalia margaritae* (3.60 Ma), which marks the base of Zone PL3, both occur between Samples 363-U1489C-7H-CC and 8H-CC (60.87–70.75 mbsf). These biohorizons also occur together in Hole U1489B. The absence of an identified stratigraphic interval corresponding to Zone PL3 at Site U1489 may be a function of its extremely short duration (3.59–3.60 Ma) and the sparse sampling and is not evidence of a hiatus.

The L9 coiling reversal in *Pulleniatina* (4.08 Ma) occurs between Samples 363-U1489C-8H-CC and 9H-CC (70.75–79.94 mbsf) (Figure **F16**). This occurs above biohorizon top *Pulleniatina spectabilis* (4.21 Ma), which is in the same sampling interval as bio-

Table T5. Planktonic foraminifer bioevents, Site U1489. * = biohorizon follows Chaisson and Pearson (1997), † = biohorizon follows Berggren et al. (1995). B = base, T = top, X = coiling reversal, s = sinistral, d = dextral. **Download table in CSV format.**

Biohorizon number	Marker species	Age (Ma)	Zone base	Top core, section, interval (cm)	Bottom core, section, interval (cm)	Top depth (mbsf)	Bottom depth (mbsf)	Midpoint depth (mbsf)	± (m)
				363-U1489C-	363-U1489C-				
1	T *Globorotalia flexuosa*	0.07			1H-CC		3.54	1.77	1.77
2	T *Globigerinoides ruber* (pink)	0.12			1H-CC		3.54	1.77	1.77
3	B *Globigerinella calida*	0.22			1H-CC		3.54	1.77	1.77
4	B *Globorotalia flexuosa*	0.40		1H-CC	2H-CC	3.54	13.31	8.43	4.89
6	T *Globorotalia tosaensis*	0.61	Pt1b	1H-CC	2H-CC	3.54	13.31	8.43	4.89
8	X *Pulleniatina* s to d "L1"	0.80		2H-CC	3H-CC	13.31	22.85	18.08	4.77
11	T *Globigerinoidesella fistulosa*	1.88	Pt1a	3H-CC	4H-CC	22.85	32.34	27.60	4.75
14	B *Pulleniatina finalis*	2.04		4H-CC	5H-CC	32.34	41.61	36.98	4.63
17	T *Globorotalia pseudomiocenica*	2.30	PL6	5H-CC	6H-CC	41.61	51.40	46.51	4.89
18	T *Globorotalia limbata*	2.39		6H-CC	7H-CC	51.40	60.87	56.14	4.74
	Pliocene/Pleistocene boundary	2.58							
21	B *Globigerinoidesella fistulosa*	3.33		6H-CC	7H-CC	51.40	60.87	56.14	4.74
23	T *Dentoglobigerina altispira*	3.13*	PL5	6H-CC	7H-CC	51.40	60.87	56.14	4.74
25	T *Sphaeroidinellopsis seminulina*	3.59	PL4	7H-CC	8H-CC	60.87	70.75	65.81	4.94
28	T *Globorotalia margaritae*	3.60†	PL3	7H-CC	8H-CC	60.87	70.75	65.81	4.94
29	X *Pulleniatina* s to d "L9"	4.08		8H-CC	9H-CC	70.75	79.94	75.35	4.59
30	T *Pulleniatina spectabilis*	4.21		9H-CC	10H-CC	79.94	89.39	84.67	4.72
32	T *Globoturborotalita nepenthes*	4.37	PL2	9H-CC	10H-CC	79.94	89.39	84.67	4.72
34	T *Sphaeroidinellopsis kochi*	4.53		10H-CC	11H-CC	89.39	98.83	94.11	4.72
35	T *Globorotalia cibaoensis*	4.61		10H-CC	11H-CC	89.39	98.83	94.11	4.72
	Miocene/Pliocene boundary	5.33							
36	B *Sphaeroidinella dehiscens* s.l.	5.53		15H-CC	16H-1, 40–42	136.11	136.90	136.51	0.39
37	B *Globorotalia tumida*	5.57	PL1	15H-6, 60–62	15H-CC	135.10	136.11	135.61	0.51
39	T *Globoquadrina dehiscens*	5.92		11H-CC	12H-CC	98.83	108.44	103.64	4.80
40	B *Globorotalia margaritae*	6.08		17H-4, 40–42	17H-6, 40–42	150.90	153.90	152.40	1.50
41	T *Globorotalia lenguaensis*	6.13	M14	17H-2, 40–42	17H-4, 40–42	147.90	150.90	149.40	1.50
43	X *Neogloboquadrina acostaensis* s to d	6.34		19H-6, 60–62	19H-CC	173.10	174.46	173.78	0.68
44	B *Pulleniatina primalis*	6.60		20H-6, 60–62	20H-CC	182.60	183.28	182.94	0.34
45	X *Neogloboquadrina acostaensis* d to s	6.77		20H-CC	21H-2, 50–52	183.28	186.00	184.64	1.36
47	B *Globorotalia plesiotumida*	8.58	M13b	29H-CC	30F-3, 58–60	269.93	271.29	270.61	0.68
51	B *Neogloboquadrina acostaensis*	9.83	M13a	32X-CC	33X-CC	287.06	297.22	292.14	5.08
52	T *Paragloborotalia mayeri*	10.46	M12	33X-CC	34X-CC	297.22	307.97	302.60	5.38
53	B *Globorotalia limbata*	10.64		34X-CC	35X-CC	307.97	317.58	312.78	4.80
54	T *Cassigerinella chipolensis*	10.89		33X-CC	34X-CC	297.22	307.97	302.60	5.38
57	T *Globigerinoides subquadratus*	11.54		35X-CC	36X-CC	317.58	327.35	322.47	4.89
59	T *Fohsella fohsi*	11.79	M10	36X-CC	37X-CC	327.35	335.15	331.25	3.90
60	B *Fohsella robusta*	13.13	M9b	38X-CC	39X-CC	346.95	356.63	351.79	4.84
61	B *Fohsella fohsi*	13.41	M9a	38X-CC	39X-CC	346.95	356.63	351.79	4.84
63	T *Fohsella peripheroronda*	13.80		38X-CC	39X-CC	346.95	356.63	351.79	4.84
68	T *Praeorbulina sicana*	14.53		38X-CC	39X-CC	346.95	356.63	351.79	4.84
69	T *Globigerinatella insueta*	14.66		39X-CC	40X-CC	356.63	364.00	360.32	3.69
74	B *Praeorbulina glomerosa*	16.27		40X-CC	41X-CC	364.00	371.98	367.99	3.99
75	B *Praeorbulina sicana*	16.38	M5a	40X-CC	41X-CC	364.00	371.98	367.99	3.99
78	T *Catapsydrax dissimilis*	17.54	M4a	41X-CC	42X-CC	371.98	384.21	378.10	6.12
79	B *Globigerinatella insueta* s.s.	17.59		41X-CC	42X-CC	371.98	384.21	378.10	6.12
81	T *Dentoglobigerina binaiensis*	19.09		41X-CC	42X-CC	371.98	384.21	378.10	6.12
83	B *Globigerinoides altiaperturus*	20.03		41X-CC	42X-CC	371.98	384.21	378.10	6.12
83	T *Tenuitella munda*	20.78		> Total depth		>384.21			

Table T6. Coiling count data for *Pulleniatina*, Holes U1489B and U1489C. **Download table in CSV format.**

horizon top *Globoturborotalita nepenthes* (4.37 Ma), marking the base of Zone PL2, between Samples 9H-CC and 10H-CC (79.94–89.39 mbsf).

Globoquadrina dehiscens appears to have an anomalous stratigraphic range at Site U1489, occurring as high as Sample 363-U1489C-12H-CC (108.44 mbsf), and almost as high in Hole U1489B (Sample 363-U1489B-13H-CC, 119.21 mbsf). This bioevent is known to be diachronous, occurring later in the tropics than at higher latitudes (Hodell and Kennett, 1986). High-resolution sampling of Sites U1482, U1489, and U1490 will be conducted postcruise to better calibrate this biohorizon for the low latitudes.

Biohorizon base *Globorotalia tumida* (5.57 Ma), which marks the base of Zone PL1, occurs between Samples 363-U1489C-15H-6, 60–62 cm, and 15H-CC (135.10–136.11 mbsf). The top of *Globorotalia lenguaensis* (6.13 Ma), which marks the base of Zone M14, is tentatively identified between Samples 17H-2, 40–42 cm, and 17H-4, 40–42 cm (147.90–150.90 mbsf), based on the occurrence of very rare globorotaliids with an almost circular periphery and no keel but with a faster rate of chamber expansion than seen in the holotype of Bolli (1957). Taxonomic concepts in the literature seem quite divergent, and it is doubtful whether the holotype is conspe-

Figure F16. Coiling patterns in *Pulleniatina*, Holes U1489B and U1489C.

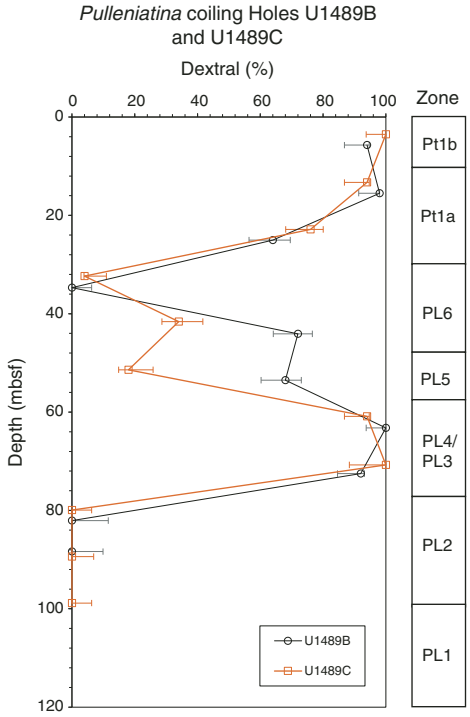

cific with either of our specimens or the specimen illustrated by Kennett and Srinivasan (1983). More thorough investigations post-cruise may help clarify these issues.

Zone M13 (6.13–10.47 Ma) is a long and problematic interval for planktonic foraminifer biostratigraphy with few reliable marker events and is complicated further at Site U1489 by the presence of a stratigraphic succession between ~150 and 250 mbsf characterized by soft-sediment deformation that may indicate transport and redeposition of sediment with the possibility of associated erosional events and missing stratigraphy (see **Core description**). One clear biohorizon in the upper part of the zone is base *Pulleniatina primalis* (6.60 Ma) between Samples 363-U1489C-20H-6, 60–62 cm, and 20H-CC (182.60–183.28 mbsf). This species is common in the lowermost sample in which it is observed and shows no indication of intergradation with its presumed ancestor, *Neogloboquadrina acostaensis*. The base of Subzone M13a is marked by biohorizon base *Globorotalia plesiotumida* (8.58 Ma), which is tentatively identified between Samples 29-CC and 30F-3, 58–60 cm (269.11–271.29 mbsf). This event should supposedly occur close to biohorizon base *Neogloboquadrina humerosa* (8.56 Ma), but this biohorizon is not securely identified at Site U1489 because of the rarity of the marker species in the lower part of its stratigraphic range.

To further understand the stratigraphy of this interval and the correlation with Site U1488, which is located 81 km to the east (see **Biostratigraphy** in the Site U1488 chapter [Rosenthal et al., 2018c]), we measured coiling directions in *N. acostaensis* in the stratigraphic interval between 119 and 287 mbsf in Hole U1489C. The data are given in Table **T7** and plotted in Figure **F18**, which compares the Site U1489 coiling data with those from Site U1488 together with two reliable nannofossil biohorizons in this interval (see **Calcareous nannofossils**). The records at Sites U1488 and U1489 have various features in common and also significant differences. Biohorizon base *P. primalis* occurs between two sinistral excursions that can be tentatively correlated with those indicated in

Figure F17. *Globigerinoidesella fistulosa* whole tests and individual chambers (U1489C-6H-CC).

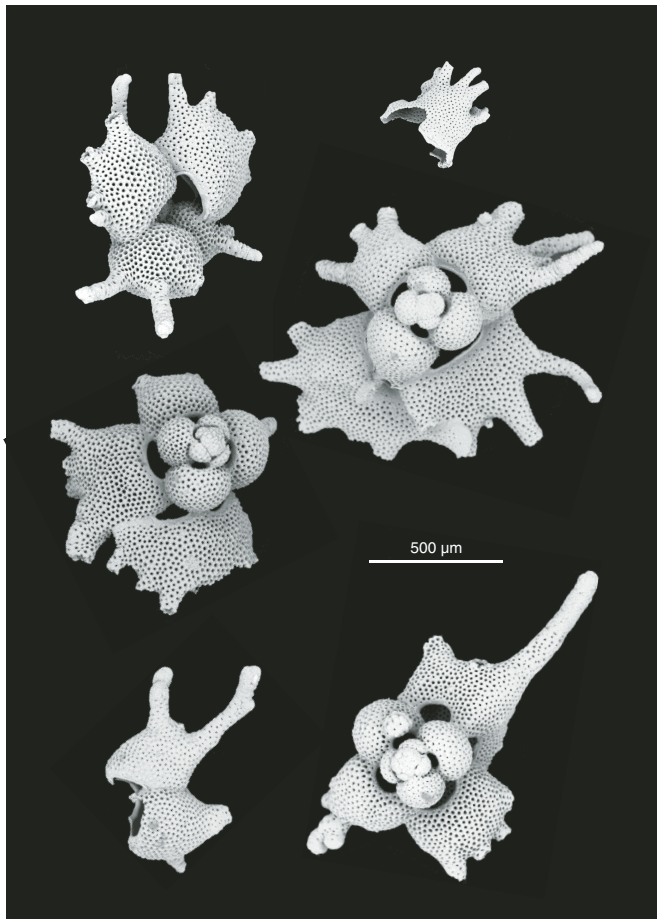

Table T7. Coiling count data for *Neogloboquadrina acostaensis*, Hole U1489C. **Download table in CSV format.**

Wade et al. (2011) at 6.34 and 6.77 Ma, respectively. Below this at both sites is an interval of ~30 m in which the coiling ratio is typically 90%–100% dextral. At Site U1488, one isolated sinistral (0% dextral) excursion occurs at ~224.76 mbsf, which may correlate with one of two strongly sinistral excursions at 217.59 and 224.09 mbsf at Site U1489. Below that, correlation of the records is helped by consideration of biohorizons base *Discoaster quinqueramus* (8.12 Ma) and base paracme *Reticulofenestra pseudoumbilicus* (8.79 Ma), which may indicate that Site U1489 is expanded relative to Site U1488 in the 220–250 mbsf interval but condensed and/or incomplete in the 250–270 mbsf interval.

Below 270 mbsf, following a lithologic change to much more indurated sediment (see **Core description**), a more readily interpretable biostratigraphy resumes to the base of Holes U1489C and U1489D, as determined through core catcher samples from the XCB cores. Biohorizon base *N. acostaensis* (9.83 Ma), which demarcates the base of Subzone M13a, is observed between Samples 363-U1489C-32X-CC and 33X-CC (287.06–297.22 mbsf). In Hole U1489D, this biohorizon occurs at a comparable depth (283.66–292.67 mbsf) between Samples 363-U1489D-16X-CC and 17X-CC.

The base of Zone M12 is marked by biohorizon top *Paragloborotalia mayeri* (10.46 Ma) between Samples 363-U1489C-33X-CC and 34X-CC (297.22–307.97 mbsf). Biohorizon top *Cassi-*

Figure F18. Comparison of coiling patterns in *Neogloboquadrina acostaensis*, Sites U1488 and U1489. Tie points: blue lines = planktonic foraminifer biohorizons, red lines = calcareous nannofossil biohorizons.

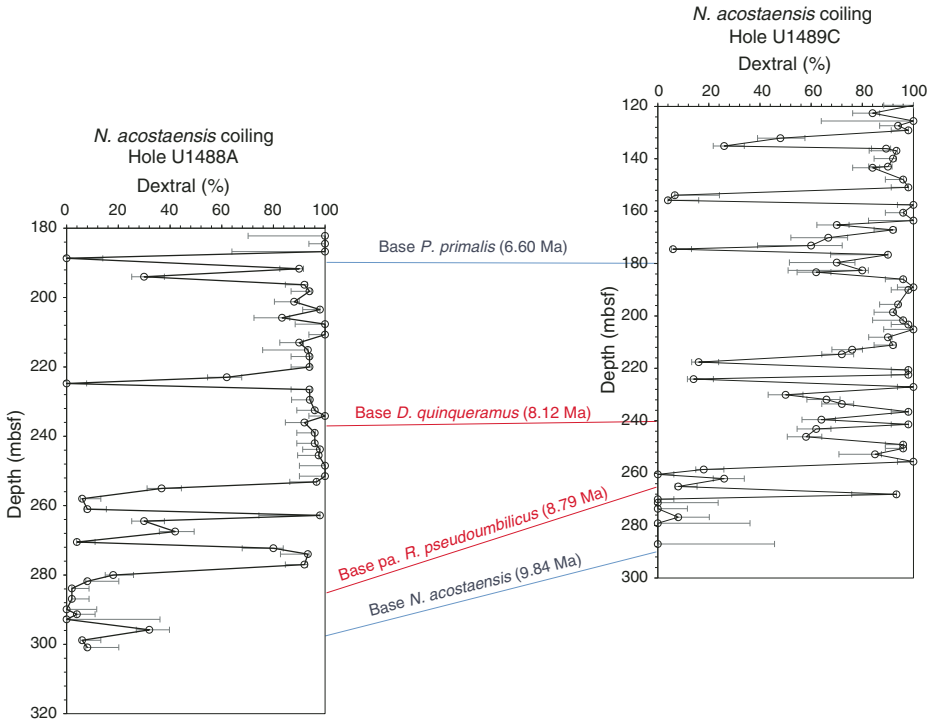

gerinella chipolensis (10.89 Ma) is also observed between these samples; this species unexpectedly co-occurs with *Globorotalia limbata*, the biohorizon base of which (10.64 Ma) is between Samples 34X-CC and 35X-CC (307.97–317.58 mbsf).

The base of Zone M11 could not be determined due to the absence of *G. nepenthes* near the base of its expected stratigraphic range; therefore, Zones M10 and M11 are undifferentiated. Division of the interval is achieved by biohorizon top *Globigerinoides subquadratus* (11.54 Ma) between Samples 363-U1489C-35X-CC and 36X-CC (317.58–327.35 mbsf).

Biohorizon top *Fohsella fohsi* (11.79 Ma) occurs between Samples 363-U1489C-36X-CC and 37X-CC (327.35–335.15 mbsf). Also occurring in Sample 37X-CC are *Fohsella robusta* (indicating Subzone M9b) and *Fohsella lobata*. A similar assemblage occurs in Sample 38X-CC (346.95 mbsf), although both samples are indurated and foraminifers are poorly preserved. Samples 39X-CC (356.63 mbsf) and 40X-CC (364.00 mbsf) contain better preserved assemblages lacking *F. fohsi* but including *Fohsella peripheroronda* and *Praeorbulina glomerosa* and therefore are assigned to Subzone M5b (13.80–14.22 Ma). Sample 40X-CC also contains the distinctive species *Mutabella mirabilis* and *Globigerinatella insueta* (the latter with multiple areal apertures). Sample 41X-CC (371.98 mbsf) lacks *Praeorbulina* and *Catapsydrax* and therefore is assigned to Zone M4 (undifferentiated). However, the sample does contain the index fossil *Globigerinatella* sp. (i.e., the form lacking areal apertures; see Pearson, 1995, for discussion).

The lowermost sample in Hole U1489C, Sample 363-U1489C-42X-CC (384.21 mbsf) lacks *Globigerinatella* sp. and *Paragloborotalia kugleri* and therefore is assigned to Zone M2. The age range is constrained to the upper part of that zone by the presence of *Dentoglobigerina binaiensis* (>19.30 Ma) and the absence of *Globigerinoides altiaperturus* (>20.03 Ma) and *Tenuitella munda* (<20.78 Ma). The lowermost sample in Hole U1489D, Sample 363-U1489D-27X-CC (386.28 mbsf), contains *D. binaiensis* (>19.30 Ma) with *G. altiaperturus* (<20.03) and so appears to be from a higher level in Zone M2 than the lowest sample in Hole U1489C.

Table T8. Benthic foraminifer distribution, Hole U1489C. **Download table in CSV format.**

Benthic foraminifers

Benthic foraminifers were studied in 37 core catcher samples from Hole U1489C (Samples 363-U1489C-1H-CC [3.54 mbsf] to 42X-CC [384.21 mbsf]). Census count data are presented in Table **T8**. The benthic foraminifer assemblages at Site U1489 are characteristic of deep bathyal to abyssal depths (van Morkhoven et al., 1986). The planktonic:benthic foraminifer ratio is ~99:1 throughout Hole U1489C. *Planulina wuellerstorfi* and/or *Cibicidoides mundulus* are present in most of the samples examined from the top to the base of the hole, and other common taxa include *Laevidentalina* spp.

Foraminifer preservation

Five core catcher samples from Hole U1489C were selected to assess foraminifer preservation and diagenesis. These range in age from the late Pleistocene (0.12 Ma) to middle Miocene (~19.09–20.78 Ma). The upper four samples (Samples 363-U1489C-1H-CC [3.54 mbsf], 12H-CC [108.44 mbsf], 23H-CC [212.84 mbsf]), and 34X-CC [307.97 mbsf] are spaced at ~100 m intervals, and the lower sample (Sample 42X-CC [384.26 mbsf]) was taken from the bottom of the hole. As at other Expedition 363 sites, typical specimens of the planktonic foraminifer *Trilobatus trilobus* and benthic foraminifer *P. wuellerstorfi* were selected for detailed investigation, but *P. wuellerstorfi* is absent in the lowermost sample (Sample 42X-CC) so *Cibicidoides* sp. was selected instead.

Foraminifer preservation, as assessed visually in the core catcher samples, varies from very good to good for most of the succession but is moderate to poor for Cores 363-U1489C-31F to 42X. Even where preservation is very good, foraminifers are typically white and opaque rather than glassy and translucent. Recrystallization, overgrowth, and cementation become progressively more severe at greater depth. Dissolution and minor infilling of the planktonic foraminifer *T. trilobus* and incipient recrystallization of the benthic foraminifers *P. wuellerstorfi* and *Cibicidoides* sp. occurs throughout the site. Images of selected specimens are shown in Figure **F19**. The full set of images is available in the LIMS database.

Sample 363-U1489C-1H-CC (3.54 mbsf, late Pleistocene to latest middle Pleistocene, 0.12–0.22 Ma) shows excellent to very good preservation. Foraminifers have a glassy appearance under the light microscope (LM). In *T. trilobus*, the outer wall surfaces show minor evidence of abrasion and dissolution. The wall cross sections show microgranular textures and other typical biogenic features. Evidence of very minor dissolution is observed near the level of the primary organic membrane in some places. The inner wall surfaces exhibit minor calcite overgrowth layers <1 µm thick, with small amounts of unconsolidated and/or consolidated sediment infill. The wall cross sections of *P. wuellerstorfi* specimens show evidence of minor but pervasive textural alteration, which may be evidence of incipient recrystallization. *P. wuellerstorfi* also exhibits smooth inner wall surfaces. There is no evidence of cementation.

Sample 363-U1489C-12H-CC (108.44 mbsf, early Pliocene to latest Miocene, ~5.28–5.35 Ma) shows very good preservation. Wall cross sections of *T. trilobus* show the biogenic microgranular textures typical of the species and inorganic calcite overgrowth in pore channels with minor evidence of dissolution. In *P. wuellerstorfi*, the wall cross sections show evidence of very minor textural alteration in places indicating incipient recrystallization. The inner wall surfaces of *T. trilobus* and *P. wuellerstorfi* exhibit minor calcite overgrowth layers <1 µm thick without evidence of infilling and cementation.

Sample 363-U1489C-23H-CC (212.84 mbsf, late Miocene, ~6.77–8.58 Ma) shows very good to good preservation. Wall cross sections of *T. trilobus* show minor textural alteration in places indicating incipient recrystallization and dissolution. The wall cross sections of *P. wuellerstorfi* show widespread evidence of early stage recrystallization in which the microgranular texture is modified, showing slightly larger and better separated granular crystals, particularly toward the inner surfaces. The inner wall surfaces of *T. trilobus* and *P. wuellerstorfi* exhibit minor calcite overgrowth layers as thick as 1 µm. *P. wuellerstorfi* also shows calcite overgrowth on external surfaces. There is no evidence of infilling and cementation.

Sample 363-U1489C-34X-CC (307.97 mbsf; late Miocene; ~10.47–10.65 Ma) shows moderate to poor preservation. Foraminifers are generally opaque under the light microscope and exhibit strong cementation. Wall cross sections of *T. trilobus* show evidence of early stage recrystallization and stronger dissolution along internal layers, but other parts of the wall cross sections, especially the gametogenic calcite, are well preserved, showing the typical microgranular texture of the species. Wall cross sections of *P. wuellerstorfi* also show obvious evidence of incipient recrystallization. The inner wall surfaces of *T. trilobus* and *P. wuellerstorfi* exhibit minor calcite overgrowth layers as thick as 1 µm, which also occur on outer surfaces. There is no evidence of infilling.

Sample 363-U1489C-42X-CC (384.26 mbsf; early Miocene; ~19.09–20.78 Ma) shows poor preservation. Foraminifers are generally opaque under the light microscope and exhibit strong cementation. In SEM there is abundant evidence of dissolution, infilling, overgrowth, recrystallization, and cementation. Both *T. trilobus* and *Cibicidoides* sp. show evidence of incipient recrystallization with more solid patches developing within the wall. Wall cross sections of *T. trilobus* show evidence of dissolution near spine holes and internal wall layers. The inner wall surfaces of *T. trilobus* and *Cibicidoides* sp. are strongly overgrown with calcite and/or dolomite, with minor infilling of unconsolidated sediment (coccoliths) in some specimens. *Cibicidoides* sp. also shows calcite overgrowth on external surfaces.

Shipboard age model

Integrated calcareous nannofossil and planktonic foraminifer biostratigraphy is shown on an age-depth plot (Figure **F20**), together with magnetostratigraphic horizons for the Pliocene and Pleistocene (see **Paleomagnetism**). Planktonic foraminifer and calcareous nannofossil bioevents typically show excellent congruence.

Long-term average sedimentation rates through early to middle Miocene from the base of the hole to ~345 mbsf are low (~0.3 cm/ky). Between 345 and 275 mbsf, average sedimentation rates in the late Miocene increased to ~2 cm/ky. In the latest Miocene and earliest Pliocene (100–275 mbsf), average sedimentation rates apparently increased to greater than ~5 cm/ky. However, this interval is complicated by soft-sediment deformation, which may locally repeat and extend the stratigraphic sequence (see **Core description**), and the estimated rate is based on sparse bioevents (and no magnetostratigraphic events) that may not be reliable. Above this interval with deformed sediment, Pliocene and Pleistocene (0–100 mbsf) sedimentation rates were ~2 cm/ky, which is comparable to the late Miocene.

Figure F19. Downhole foraminifer preservation states, Site U1489. A. Light microscope images to assess the extent of fragmentation and staining and whether the tests are glassy or opaque. B. SEM images of selected specimens (*T. trilobus, P. wuellerstorfi*, and *Cibicidoides* sp.) as whole tests, umbilical side upward. C. High-magnification images of outer wall surfaces to examine additional features such as spine holes, pustules, etc. D. High-magnification images of wall cross sections to find original microgranules or diagenetic crystallites. E. High-magnification images of inner wall surfaces focusing on evidence for internal overgrowth and cementation.

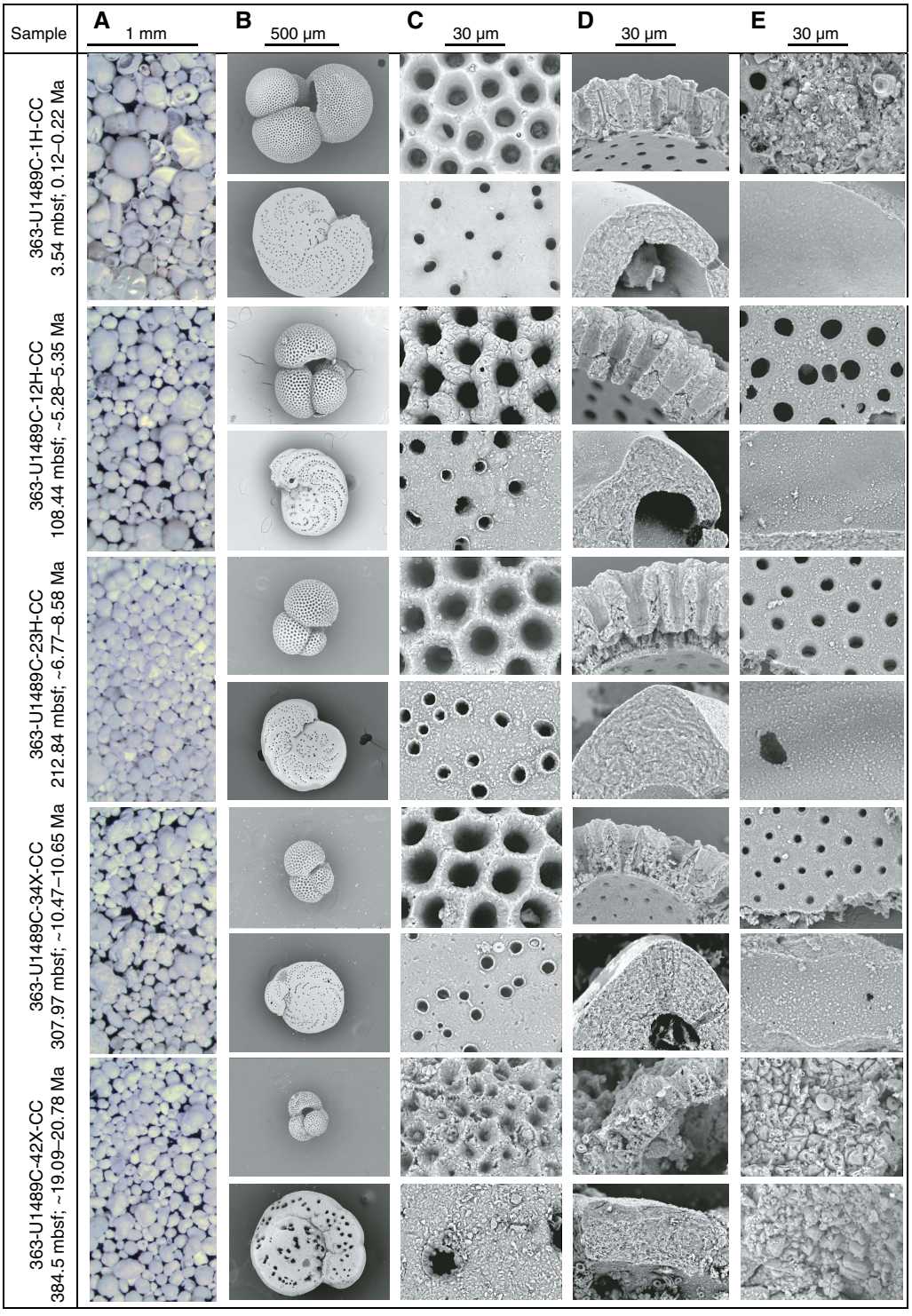

Figure F20. Age-depth plot for Site U1489 showing integrated biomagnetochronology in Hole U1489C with additional paleomagnetic data from Hole U1489D. Data plotted on the mbsf depth scales for Holes U1489C and U1489D account for the difference in the measured depths of paleomagnetic reversals in the two holes. The stratigraphy of the base of Hole U1489C is constrained by biohorizon base *Sphenolithus belemnos* (19.03 Ma) and by the presence of *Dentoglobigerina binaiensis* (>19.30 Ma) and absence of *Globigerinoides altiaperturus* (>20.03 Ma) and *Tenuitella munda* (<20.78 Ma) at ~380 mbsf. Average sedimentation rates vary from ~0.3 to 5 cm/ky. PF = planktonic foraminifer.

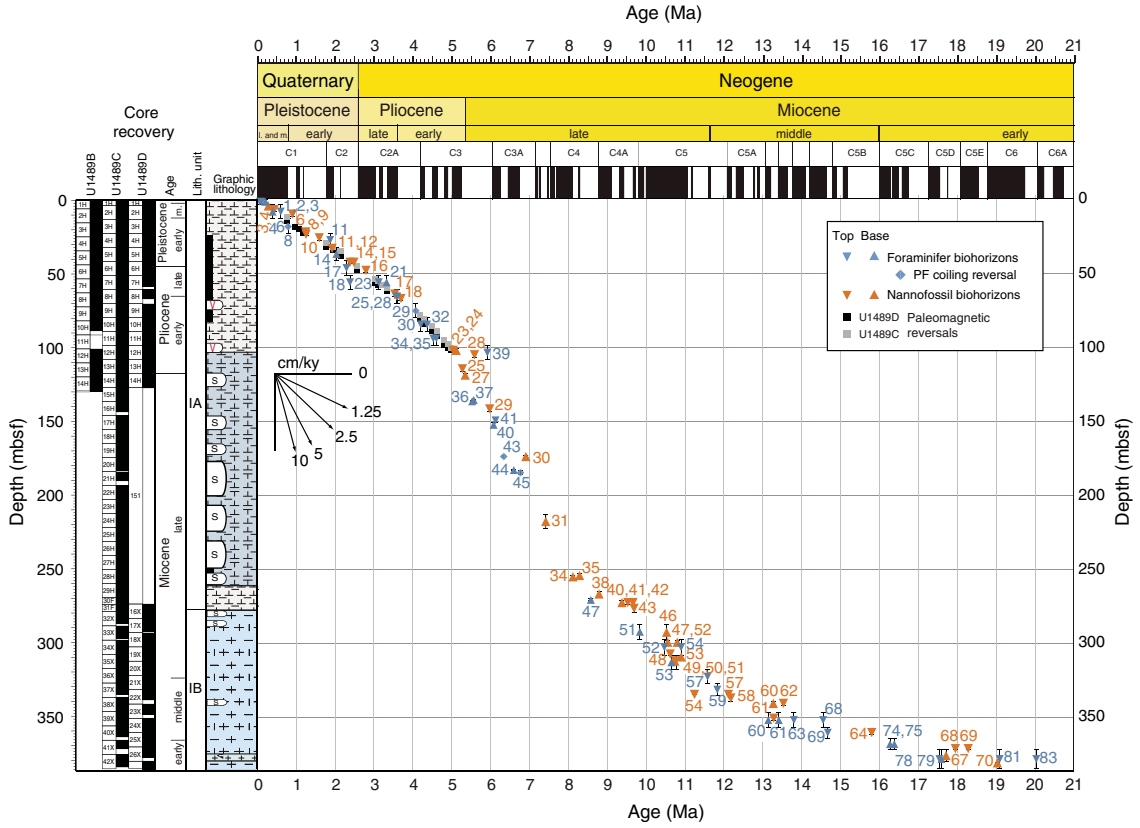

Paleomagnetism

Measurements summary

Paleomagnetic investigations at Site U1489 involved measurement of the natural remanent magnetization (NRM) of APC and HLAPC archive-half cores from Holes U1489A–U1489D before and after alternating field (AF) demagnetization. We employed a four-step NRM and AF demagnetization procedure (NRM and 10, 15, and 20 mT) to the first four sections of Core 363-U1489A-1H to determine the single peak AF field (15 mT) with which to demagnetize all sections from Holes U1489B–U1489D. In addition to measuring 358 core sections, we took one to two discrete samples per core from Holes U1489B (25 samples) and U1489C (42 samples) to characterize the NRM demagnetization behavior and to investigate the rock magnetic properties of the sediment. The NRM of discrete samples was measured before and after AF demagnetization in peak fields of 5, 10, 15, 20, 30, and 40 mT. Rock magnetic investigations comprised measurements of magnetic susceptibility (χ), susceptibility of anhysteretic remanent magnetization (χARM) imparted using a 100 mT AF demagnetization and 0.05 mT direct current bias field, and isothermal remanent magnetization (IRM) acquired in 300 mT and 1000 mT (saturation IRM [SIRM]) fields. All sample measurements were mass corrected. The Icefield MI-5 core orientation tool was deployed with nonmagnetic hardware for all APC cores, which permitted azimuthal correction of declination. Azimuthally corrected declination is largely coherent between cores; however, absolute values in Hole U1489B cluster around 90°–120° for intervals of normal polarity and around 270°–300° for reversed polarity, whereas in Holes U1489C and U1489D declinations cluster around 270° during periods of normal polarity and 90° for periods of reversed polarity. An absolute offset in azimuthally corrected declination is a common feature of Expedition 363 cores (see **Paleomagnetism** in the Expedition 363 methods chapter [Rosenthal et al., 2018a]); however, the baseline offset was relatively consistent at ~180° until an ~90° offset developed at Site U1488. This ~90° offset appears to have continued during operations at Site U1489. As with other sites cored during Expedition 363, we leave declination uncorrected for these additional offsets in the plotted figures, so care should be employed for future calculations of virtual geomagnetic poles using these data.

Rock magnetic characterization

In the upper ~90 mbsf, Whole-Round Multisensor Logger (WRMSL) magnetic susceptibility values average 29×10^{-5} SI (see **Physical properties**) and, when coupled with average χ ($2.1 \times 10^{-7} \pm 1.8 \times 10^{-7}$ m^3/kg as 2 standard deviations [2σ]) and SIRM ($2.4 \times 10^{-3} \pm 2.1 \times 10^{-3}$ Am^2/kg as 2σ) values, suggest moderately low (ferri)magnetic mineral concentration in the sediments deposited at Site U1489 (Figure **F21**). In the upper ~90 mbsf, all samples acquire >97% of their SIRM remanence in a field of 300 mT, suggesting that ferrimagnetic minerals (e.g., [titano]magnetite [$Fe_xTi_xO_4$] and/or maghemite [γ-Fe_2O_3]) control the remanence-carrying properties of

Figure F21. Archive-half NRM intensity after 15 mT AF demagnetization, discrete sample χ and SIRM, and discrete sample χARM/SIRM and IRM_{300mT}/IRM_{1000mT} ratios, Holes U1489B and U1489C.

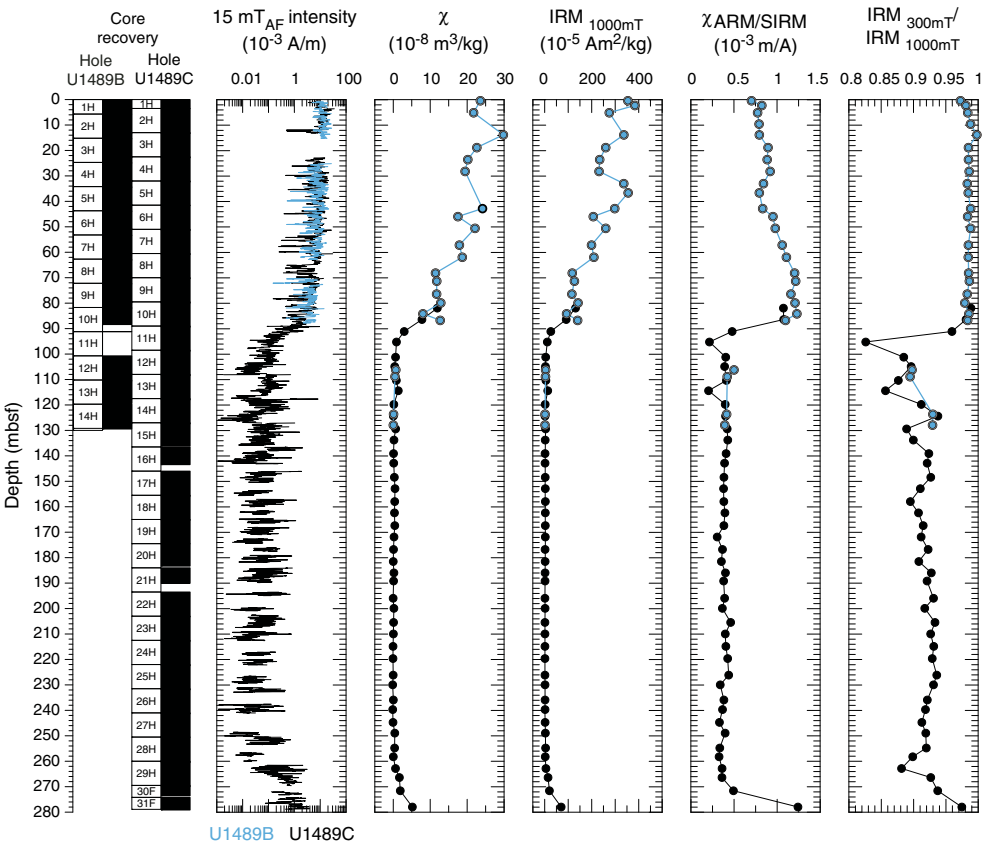

the sediment. From the top of the hole to ~90 mbsf, magnetic concentration steadily declines (lower values of χ and SIRM) and magnetic grain size fines (higher values of χARM/SIRM). Between ~90 and 100 mbsf, NRM_{15mT}, χ, SIRM, and χARM/SIRM values decrease sharply, and below ~100 mbsf, NRM_{15mT}, magnetic susceptibility, and SIRM values are approximately one to two orders of magnitude lower than in the upper ~90 mbsf, indicating a significant reduction in magnetic mineral concentration and a coarsening of magnetic grain size below ~100 mbsf. Low magnetic concentration and lower IRM_{300mT}/IRM_{1000mT} values below ~100 mbsf likely reflect the almost total absence of magnetite rather than an increase in the relative proportions of higher coercivity components (e.g., hematite [Fe_2O_3] and goethite [FeO(OH)]). Reduced concentration of ferrimagnetic minerals and a coarser ferrimagnetic grain size assemblage downhole, coupled with observations of secondary iron sulfides (e.g., pyrite [FeS_2]) in all lithologic subunits at Site U1489 (see **Core description**), suggest sediment diagenesis (e.g., Karlin and Levi, 1983; Rowan et al., 2009) may have strongly influenced the primary magnetic mineral assemblage below ~90 mbsf at Site U1489.

Paleomagnetic data and core orientation

NRM demagnetization behavior and IRM_{300mT}/IRM_{1000mT} ratios in the upper ~90 mbsf are consistent with (titano)magnetite being the primary remanence-carrying mineral species in sediments deposited at Site U1489 (Figures **F21**, **F22A–F22D**). In this uppermost interval, the drill string overprint is effectively removed after AF demagnetization in a 5–15 mT field, and following exposure to higher AF demagnetization steps, inclination and declination stabilize and trend to the origin on Zijderveld diagrams (Zijderveld, 1967), indicating a single component to the magnetization. Excluding a relatively high value at ~62 mbsf, origin-anchored maximum angular deviation values of the principal component analysis (PCA) calculated over the 15–40 mT range average 1.7° (range = 0.8°–5.1°) for the upper ~90 mbsf of Hole U1489B (Figures **F22A–F22D**, **F23**), suggesting paleomagnetic directions are stable and well resolved and should yield reliable estimates for magnetostratigraphy (Stoner and St-Onge, 2007). Below ~90 mbsf, maximum angular deviation values are slightly higher (average = 3.1°; range = 0.8°–13.3°) and are associated with decreased ferrimagnetic concentration, coarser ferrimagnetic grain sizes, and higher coercivity components that do not demagnetize linearly toward the origin (Figures **F22E, F22F**, **F24**), suggesting that paleomagnetic directions below 100 mbsf likely do not reflect geomagnetic field behavior.

For all APC cores from Site U1489, declination was corrected using the Icefield MI-5 tool (see **Operations**). Azimuthally corrected declination is consistent between adjacent cores within each hole, and absolute values cluster around 90°–120° and 270°–300° (Figures **F23**, **F24**, **F25**). However, assuming the uppermost sediment in each hole was deposited during normal polarity associated with the Brunhes Chron (see **Biostratigraphy**), declination values in Hole U1489B experience an offset of ~90°–120° in absolute terms because declination should cluster around 0° (180°) during periods of normal (reversed) polarity; in Holes U1489C and U1489D the absolute offset is ~270°. Although an ~180° offset was a persistent issue during Expedition 363, ~90° offsets were previously restricted to Icefield tool #2007 (which was no longer used after Site U1485) and Icefield tool #2052, which developed the issue during operations at Site U1488. All three holes at Site U1489 show evidence of a

Figure F22. A–F. Discrete sample AF demagnetization results, Site U1489. Left plots: intensity variation through progressive demagnetization steps. Middle and right plots: NRM vector measurements after each AF demagnetization treatment on orthogonal (Zijderveld; blue = horizontal projections, red = vertical projections) and stereographic (solid squares = positive inclination, open squares = negative inclination) projections, respectively. MAD = maximum angular deviation.

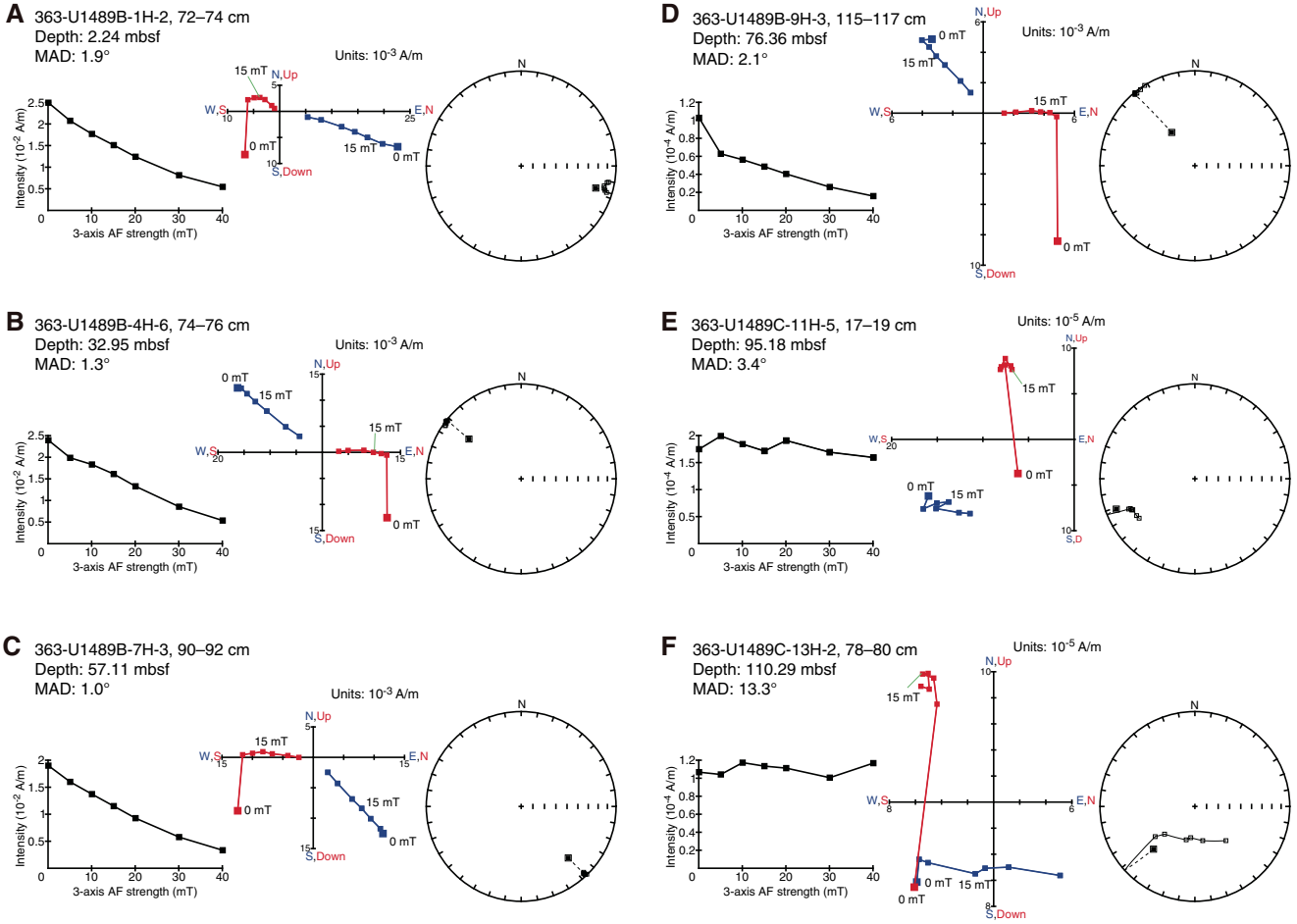

Figure F23. NRM intensities before and after 15 mT AF demagnetization, WRMSL MS, maximum angular deviation (MAD), and inclination (dashed lines = predicted values assuming a geomagnetic axial dipole [GAD] field for normal [4°] and reversed [–4°] polarity for the site latitude) and azimuthally corrected declination after 15 mT AF demagnetization, Hole U1489B. Black squares = discrete samples. Magnetostratigraphy and GPTS shown at right. Question marks at major chron boundaries reflect depth uncertainties for boundaries that were not observed in Hole U1489B. Black = normal polarity, white = reversed polarity.

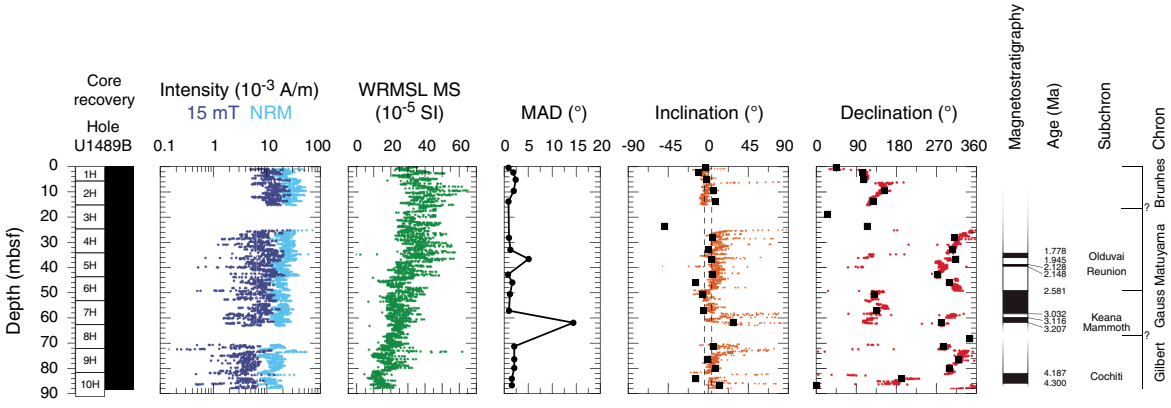

90° offset. Absolute orientation offsets appear related to specific tools because Hole U1489B was oriented using Icefield tool #2043 and Holes U1489C and U1489D were oriented using Icefield tool #2052. The origin of this offset is not immediately clear, but because it appears systematic (the two declination clusters are ~180° offset to each other during deployment of each tool respectively) we assume that declination values rotated 180° relative to the uppermost sediment values reflect periods of reversed polarity in the sediment recovered from Site U1489. Orientation tools cannot be deployed with the HLAPC coring system, and because of the low ferri-

Figure F24. NRM intensities before and after 15 mT AF demagnetization, WRMSL MS, maximum angular deviation (MAD) (black = Hole U1489C, gray = Hole U1489B), and inclination (dashed lines = predicted values assuming a GAD field for normal [4°] and reversed [−4°] polarity for the site latitude) and declination (red = azimuthally corrected values, dark red = uncorrected HLAPC cores) after 15 mT AF demagnetization, Hole U1489C. Black squares = discrete samples. Magnetostratigraphy and GPTS shown at right. Black = normal polarity, white = reversed polarity, gray = no magnetostratigraphic interpretation made from the data.

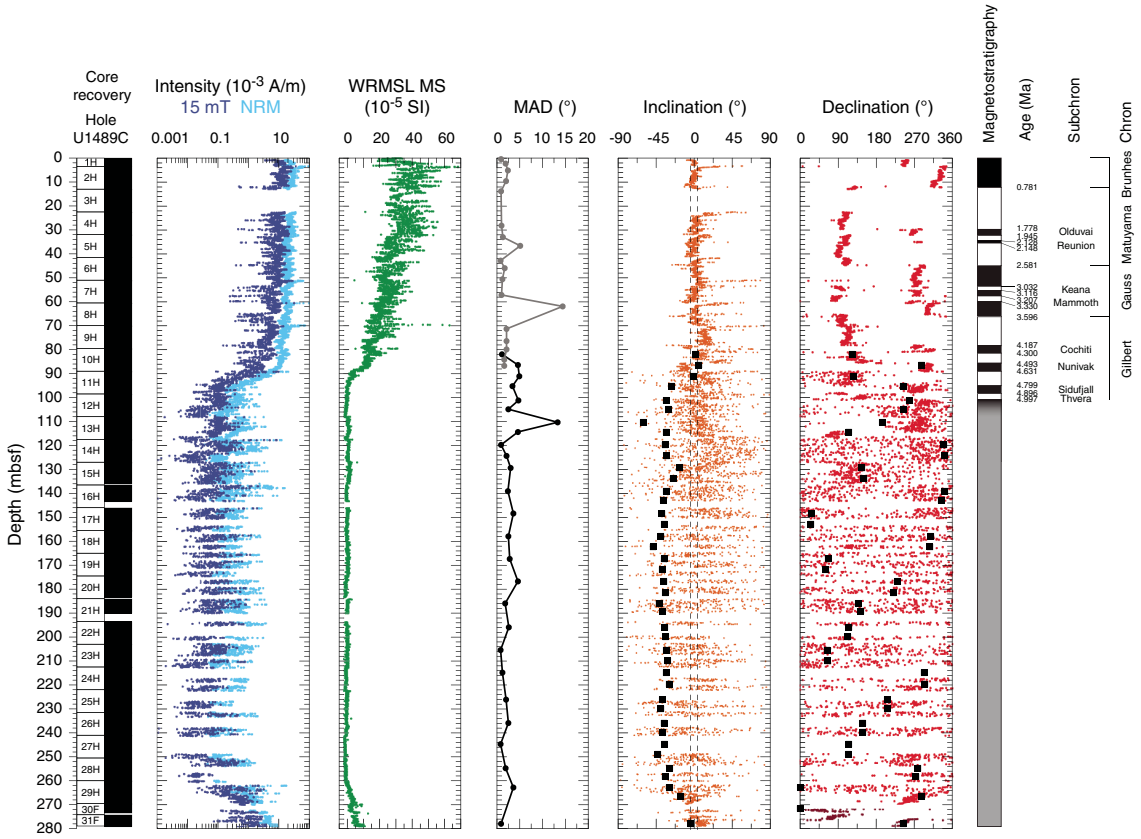

magnetic concentration and highly scattered nature of the declination of HLAPC Cores 363-U1489C-30F and 31F, we leave measured declination values uncorrected and highlight these data using dark red symbols in Figure **F24**.

NRM intensity before and after 15 mT AF demagnetization, WRMSL magnetic susceptibility, and inclination and azimuthally corrected declination after 15 mT AF demagnetization are shown for Holes U1489B, U1489C, and U1489D in Figures **F23**, **F24**, and **F25**, respectively. Displayed inclination and declination values were cleaned of visibly disturbed intervals and voids (see **Paleomagnetism** in the Expedition 363 methods chapter [Rosenthal et al., 2018a]). Flux jumps on the *y*-axis superconducting quantum interference device (SQUID) of the superconducting rock magnetometer (SRM) were a common occurrence during measurement of the magnetically weak sediments below ~140 mbsf in Hole U1489C. The lack of plotted NRM and NRM_{15mT} data in this interval reflects removal of these affected data from the displayed data set (Figure **F24**). Inclination and declination measured on discrete samples in the upper ~90 mbsf are generally in excellent agreement with those measured on the archive-half sections (Figures **F23**, **F24**). Below ~90 mbsf, discrete inclination is generally steeper and more negative than its SRM-measured counterpart. In the upper ~90 mbsf, SRM- and discrete-measured inclination plot around the expected values of ±4° for the site latitude assuming a geocentric axial dipole (GAD) field. Declination shows a similar, relatively stable pattern with data points clustering around values of inferred normal and reversed polarity. Below ~95 mbsf, inclination shows more scatter, with discrete values significantly steeper than a GAD-predicted field (Figure **F24**). Coupled with highly scattered declination values, decreased magnetic mineral concentration, and higher magnetic coercivity (Figures **F21**, **F22**, **F24**, **F25**), sediment diagenesis has likely severely altered the primary magnetic assemblage below ~100 mbsf at Site U1489; the paleogeomagnetic record is not interpretable in this deeper section.

Magnetostratigraphy

Sediments in the upper ~115 mbsf of Site U1489 appear to have been deposited (quasi)continuously with no major hiatuses; below ~115 mbsf, soft-sediment deformation results in a rapid acceleration of sedimentation rate and discontinuous sedimentation (see **Core description** and **Biostratigraphy**). Across Holes U1489B–U1489D we observed up to 22 coeval and distinct ~180° changes in declination downhole (Figures **F23**, **F24**, **F25**). Interpretation of these horizons as reversals of the geomagnetic field allows correlation to the geomagnetic polarity timescale (GPTS; Cande and Kent, 1995) of the geologic timescale (Hilgen et al., 2012) and assignment of age. The Matuyama/Brunhes boundary (0.781 Ma) is identified in Holes U1489B (11.9–11.95 mbsf) and U1489C (14.6–14.75 mbsf), the Gauss/Matuyama boundary (2.581 Ma) is identified in all three holes between 44.75 and 49.1 mbsf (note that this range encompasses the minimum and maximum mbsf depths across all three holes), and the Gilbert/Gauss boundary (3.596 Ma) is identified in Hole U1489C at 65.3–65.45 mbsf. The depths of all observed reversal horizons in each hole are listed in Table **T9**. The last observed

Figure F25. NRM intensities before and after 15 mT AF demagnetization, WRMSL MS, and inclination (dashed lines = predicted values assuming a GAD field for normal [4°] and reversed [–4°] polarity for the site latitude) and azimuthally corrected declination after 15 mT AF demagnetization, Hole U1489D. Magnetostratigraphy and GPTS shown at right. Black = normal polarity, white = reversed polarity, gray = no magnetostratigraphic interpretation made from the data.

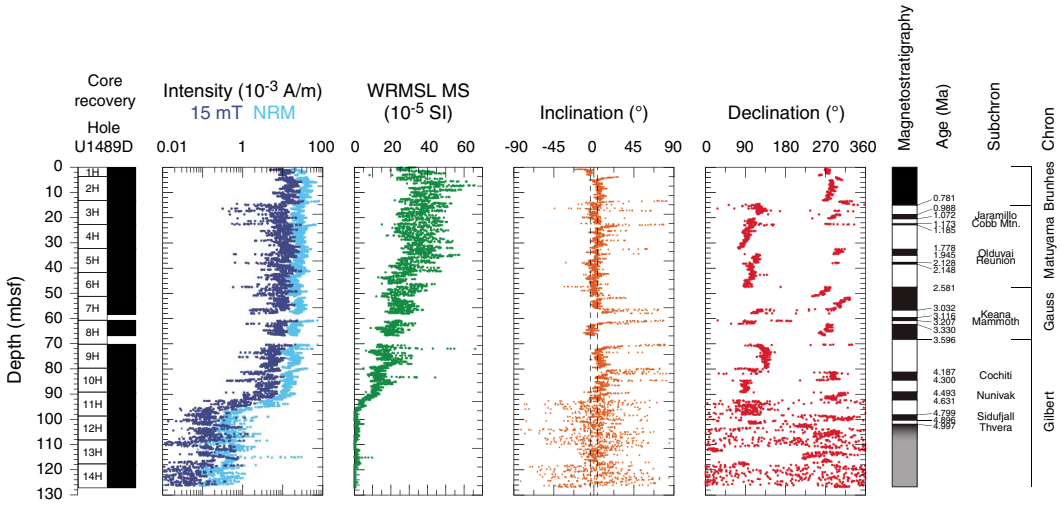

Table T9. Top and base depths of identified reversal boundaries determined from last and first points of stable polarity in Holes U1489B, U1489C, and U1489D. NO = not observed, NA = not applicable. The midpoint (arithmetic mean) and range are also shown. Ages are determined using the geologic timescale of Hilgen et al. (2012). **Download table in CSV format.**

Horizon	Chron	Age (Ma)	Top depth (mbsf)	Base depth (mbsf)	Midpoint depth (mbsf)	Range (m)	Avg. sed rate (cm/ky)
Hole U1489B							
Brunhes/Matuyama	C1n	0.781	NO	NO	NA	NA	NA
Upper Jaramillo	C1r.1r	0.988	NO	NO	NA	NA	NA
Lower Jaramillo	C1r.1n	1.072	NO	NO	NA	NA	NA
Upper Cobb Mtn.	C1r.2r	1.173	NO	NO	NA	NA	NA
Lower Cobb Mtn.	C12r.2n	1.185	NO	NO	NA	NA	NA
Upper Olduvai	C1r.3r	1.778	34.28	34.65	34.46	0.19	1.9
Lower Olduvai	C2n	1.945	36.03	36.10	36.06	0.04	1.0
Upper Reunion	C2r.1r	2.128	39.45	39.50	39.48	0.02	1.9
Lower Reunion	C2r.1n	2.148	39.73	39.78	39.75	0.02	1.4
Matuyama/Gauss	C2r.2r	2.581	48.98	49.10	49.04	0.06	2.1
Upper Keana	C2An.1n	3.032	58.03	58.13	58.08	0.05	2.0
Lower Keana	C2An.1r	3.116	59.70	59.75	59.73	0.02	2.0
Upper Mammoth	C2An.2n	3.207	61.83	62.03	61.93	0.09	2.4
Lower Mammoth	C2An.2r	3.330	NO	NO	NA	NA	NA
Gauss/Gilbert	C2An.3n	3.596	NO	NO	NA	NA	NA
Upper Cochiti	C2Ar	4.187	81.85	83.43	82.64	0.79	2.1
Lower Cochiti	C3n.1n	4.300	85.94	86.28	86.11	0.17	3.1
Hole U1489C							
Brunhes/Matuyama	C1n	0.781	11.90	11.95	11.93	0.02	1.5
Upper Jaramillo	C1r.1r	0.988	NO	NO	NA	NA	NA
Lower Jaramillo	C1r.1n	1.072	NO	NO	NA	NA	NA
Upper Cobb Mtn.	C1r.2r	1.173	NO	NO	NA	NA	NA
Lower Cobb Mtn.	C12r.2n	1.185	NO	NO	NA	NA	NA
Upper Olduvai	C1r.3r	1.778	29.70	29.78	29.74	0.04	1.8
Lower Olduvai	C2n	1.945	32.10	32.23	32.16	0.07	1.4
Upper Reunion	C2r.1r	2.128	34.95	35.08	35.01	0.07	1.6
Lower Reunion	C2r.1n	2.148	35.30	35.33	35.31	0.02	1.5
Matuyama/Gauss	C2r.2r	2.581	44.75	44.88	44.81	0.06	2.2
Upper Keana	C2An.1n	3.032	53.60	53.65	53.63	0.02	2.0
Lower Keana	C2An.1r	3.116	55.23	55.35	55.29	0.06	2.0
Upper Mammoth	C2An.2n	3.207	57.50	57.75	57.63	0.12	2.6
Lower Mammoth	C2An.2r	3.330	59.68	60.05	59.86	0.19	1.8
Gauss/Gilbert	C2An.3n	3.596	65.30	65.45	65.38	0.07	2.1
Upper Cochiti	C2Ar	4.187	78.05	78.25	78.15	0.10	2.2
Lower Cochiti	C3n.1n	4.300	80.63	81.18	80.90	0.27	2.4
Upper Nunivak	C3n.1r	4.493	85.43	85.78	85.60	0.18	2.4
Lower Nunivak	C3n.2n	4.631	89.03	89.50	89.26	0.24	2.7
Upper Sidufjall	C3n.2r	4.799	94.48	95.38	94.93	0.44	3.4
Lower Sidufjall	C3n.3n	4.896	97.83	98.05	97.94	0.11	3.1
Upper Thvera	C3n.3r	4.997	100.43	101.13	100.78	0.34	2.8
Hole U1489D							
Brunhes/Matuyama	C1n	0.781	14.60	14.75	14.68	0.07	1.9
Upper Jaramillo	C1r.1r	0.988	18.75	18.83	18.79	0.04	2.0
Lower Jaramillo	C1r.1n	1.072	20.38	20.43	20.40	0.03	1.9
Upper Cobb Mtn.	C1r.2r	1.173	22.45	22.53	22.49	0.04	2.1
Lower Cobb Mtn.	C12r.2n	1.185	22.80	23.05	22.93	0.12	3.7
Upper Olduvai	C1r.3r	1.778	32.28	32.45	32.36	0.09	1.6
Lower Olduvai	C2n	1.945	34.50	34.55	34.53	0.02	1.3
Upper Reunion	C2r.1r	2.128	37.88	37.93	37.90	0.02	1.8
Lower Reunion	C2r.1n	2.148	38.13	38.25	38.19	0.06	1.5
Matuyama/Gauss	C2r.2r	2.581	47.48	47.56	47.51	0.04	2.2
Upper Keana	C2An.1n	3.032	56.30	56.48	56.39	0.09	2.0
Lower Keana	C2An.1r	3.116	57.90	58.03	57.96	0.06	1.9
Upper Mammoth	C2An.2n	3.207	NO	NO	NA	NA	NA
Lower Mammoth	C2An.2r	3.330	62.13	62.25	62.19	0.06	2.0
Gauss/Gilbert	C2An.3n	3.596	NO	NO	NA	NA	NA
Upper Cochiti	C2Ar	4.187	80.98	81.25	81.11	0.14	2.2
Lower Cochiti	C3n.1n	4.300	84.48	84.60	84.54	0.06	3.0
Upper Nunivak	C3n.1r	4.493	89.20	89.30	89.25	0.05	2.4
Lower Nunivak	C3n.2n	4.631	92.08	92.43	92.25	0.17	2.2
Upper Sidufjall	C3n.2r	4.799	98.13	98.45	98.29	0.16	3.6
Lower Sidufjall	C3n.3n	4.896	100.40	100.73	100.56	0.16	2.3
Upper Thvera	C3n.3r	4.997	101.63	101.80	101.71	0.09	1.1

reversal horizon before magnetic concentration reaches minimum values and the paleomagnetic data become increasingly scattered and uninterpretable is the upper boundary of the Thvera normal (C3n.3r; 4.997 Ma) at 100.425–101.125 mbsf in Hole U1489C and 101.625–101.8 mbsf in Hole U1489D (Table **T9**). The paleomagnetic reversals correlate well with the calcareous nannofossil and planktonic foraminifer datums (Figure **F20**). These data imply sedimentation rates of ~2 cm/ky for the Pliocene and Pleistocene.

Physical properties

Physical properties were measured on whole-round cores, split cores, and discrete samples from all holes drilled at Site U1489 to provide basic information for characterizing the core sections. Core 363-U1489A-1H missed the mudline, so Hole U1489A was terminated after only one core. Subsequently, gamma ray attenuation (GRA) bulk density and magnetic susceptibility were measured on all core sections for Holes U1489C and U1489D with the Special Task Multisensor Logger (STMSL) immediately after the cores were brought onboard to enable fast stratigraphic correlation between holes. Core sections were measured with the GRA bulk densitometer, the magnetic susceptibility loop, and the *P*-wave logger (PWL) on the WRMSL after equilibration. PWL measurements were discontinued after Cores 363-U1489C-31F and 363-U1489D-16X when XCB coring started because data became unreliable. As soon as possible, NGR was measured on all whole-round sections (10 cm resolution for Holes U1489A and U1489B and Cores 363-U1489C-8H through 42X and 363-U1489D-16X through 27X; 20 cm resolution on Cores 363-U1489C-1H through 7H and 363-U1489D-1H through 14H (see **Physical properties** in the Expedition 363 methods chapter [Rosenthal et al., 2018a]). Point-sensor magnetic susceptibility and color spectrophotometry (color reflectance) were measured on split-core sections using the Section Half Multisensor Logger. Discrete thermal conductivity was measured on whole-round sections for Cores 363-U1489B-1H through 14H and 363-U1489C-15H through 30F and on split core sections for Cores 363-U1489C-31F through 42X. Moisture and density (MAD) measurements were made on split-core sections from Cores 363-U1489B-1H through 14H and 363-U1489C-8H through 42X. Discrete *P*-wave measurements (*z*- and *x*-axes) were made using the *P*-wave caliper (PWC) system on the Section Half Measurement Gantry for Cores 363-U1489B-1H through 14H for both *x*-axis and *z*-axis, for Cores 363-U1489C-3H and 8H through 42X for the *x*-axis, and until Core 32F for the *z*-axis. Preconditioning treatments were applied to the records to aid in interpretation of noisy or spiky data (for details, see **Physical properties** in the Expedition 363 methods chapter [Rosenthal et al., 2018a]). All data shown in figures are from the preconditioned data sets. Tables presented in this section contain raw and treated data for NGR, WRMSL GRA bulk density, magnetic susceptibility, and *P*-wave velocity. Raw data for all data sets are available from the LIMS database.

GRA bulk density

GRA bulk density is generally reproducible across holes with the exception of some intervals disturbed by coring difficulties in Hole U1489B (see **Operations**; Table **T10**). Because Holes U1489C and U1489D are the deepest holes at this site, we use them as representative for description purposes (Figure **F26**; Tables **T11**, **T12**). GRA bulk density increases rapidly over the upper 8 mbsf from ~1.3 to ~1.55 g/cm^3, similar to Site U1488. Between 8 and 220 mbsf, GRA bulk density increases from ~1.5 to ~1.8 g/cm^3. Below 100 mbsf, 10 m scale variations of ~0.15 g/cm^3 are superimposed upon the long-term downhole increasing trend. These variations co-vary with similar scale changes in *P*-wave velocity, with both GRA bulk density and *P*-wave velocity increasing downhole to 220 mbsf. These 10 m scale variations seem to correspond with the occurrence of thick homogeneous layers characterized by coarser grained foraminifer-rich sediments (see **Core description**). The variations in GRA bulk density and *P*-wave velocity could also relate to changes in sediment texture, although this relationship cannot be confirmed. Between 220 and 270 mbsf, GRA bulk density decreases to 1.5 g/cm^3 with 10 m scale variations of ~0.15 g/cm^3 superimposed. Below 270 mbsf, variability increases to ~0.30 g/cm^3 with an average of ~1.65 g/cm^3. Long-term variability is difficult to identify below 270 mbsf due to increased short-term variability, which coincides with the interval cored with the XCB system. As at Site U1488, the short-term variations in GRA bulk density do not generally correspond to sediment color variations (Figure **F27**).

Table T10. Raw, cleaned, and detrended Whole-Round Multisensor Logger gamma ray attenuation (GRA) bulk density data, Hole U1489B. **Download table in CSV format.**

Magnetic susceptibility

Magnetic susceptibility reproducibility is generally good among holes, although the magnetic susceptibility data from Hole U1489B are noisier, probably caused by sediment disturbance as a result of coring difficulties (see **Operations**) (e.g., Cores 363-U1489B-3H, 8H, and 11H through 14H). For description purposes, Holes U1489C and U1489D are used as representative (Figure **F26**; Tables **T13**, **T14**, **T15**). Magnetic susceptibility is ~30 × 10^{-5} SI near the seafloor, decreasing to ~20 × 10^{-5} SI between 0.5 and 0.6 mbsf. From 0.6 to 4 mbsf, magnetic susceptibility values increase to a maximum of 60 × 10^{-5} SI. Between 4 and 21 mbsf, average magnetic susceptibility decreases from ~40 × 10^{-5} to ~35 × 10^{-5} SI, with superimposed 1–3 m scale cyclicity, which correlates strongly with light–dark cycles in the sediment. At 21 mbsf, the dominant short-term cyclicity has distinct 0.4–0.6 m cycles, which become less distinct below ~60 mbsf but continue to ~88 mbsf. These high-frequency cycles co-vary with light–dark cycles in the sediment (Figure **F27**) and are superimposed on a decreasing downhole trend in magnetic susceptibility from ~35 × 10^{-5} to ~13 × 10^{-5} SI. The generally high magnetic susceptibility values over the upper ~100 mbsf correspond to lithologic Subunit IA. The highest magnetic susceptibility value for this site is also found within Subunit IA at ~70 mbsf, which corresponds to a tephra layer (see **Core description**). Between 88 and 94 mbsf, magnetic susceptibility decreases to 1.3 × 10^{-5} SI and remains low (0.1 × 10^{-5} ± 0.8 × 10^{-5} SI) to ~260 mbsf. At ~260 mbsf, magnetic susceptibility increases to a maximum of ~25 × 10^{-5} SI at ~319 mbsf and then decreases to ~5 × 10^{-5} SI by 330 mbsf. From 330 mbsf to the bottom of the hole (~385 mbsf), magnetic susceptibility values are ~7 × 10^{-5} ± 3 × 10^{-5} SI.

Natural gamma radiation

NGR reaches ~40 counts/s by 0.3 mbsf before rapidly decreasing to 10 count/s by 5 mbsf and then gradually decreasing further to ~5 counts/s by 54 mbsf. Between 54 and 84 mbsf, average NGR values increase slightly to 6 counts/s before decreasing to 2 counts/s at 300 mbsf (Figure **F26**; Tables **T16**, **T17**, **T18**). As at Site U1488, the decreasing NGR at Site U1489 probably reflects decreasing clay content and increasing carbonate content downhole (see **Core description** and **Geochemistry**). A maximum in NGR of 8 counts/s at 310 mbsf in Hole U1489C and at ~291 mbsf in Hole U1489D corresponds to a minimum in magnetic susceptibility (~2 × 10^{-5} SI). These coeval extreme values in NGR and magnetic susceptibility coincide with fracture arrays observed by the sedimentologists in Sections 363-U1489C-35X-2 and 363-U1489D-17X-5 (see **Core description**). It is unclear why high NGR and low magnetic susceptibility coincide with these fractures because other fracture arrays occur without a comparable change in NGR or magnetic susceptibility. Between 310 and 360 mbsf, mean NGR values are ~3 count/s,

Figure F26. Physical property measurements, Holes U1489C and U1489D. GRA bulk density, magnetic susceptibility, and *P*-wave data were measured on the WRMSL. cps = counts per second.

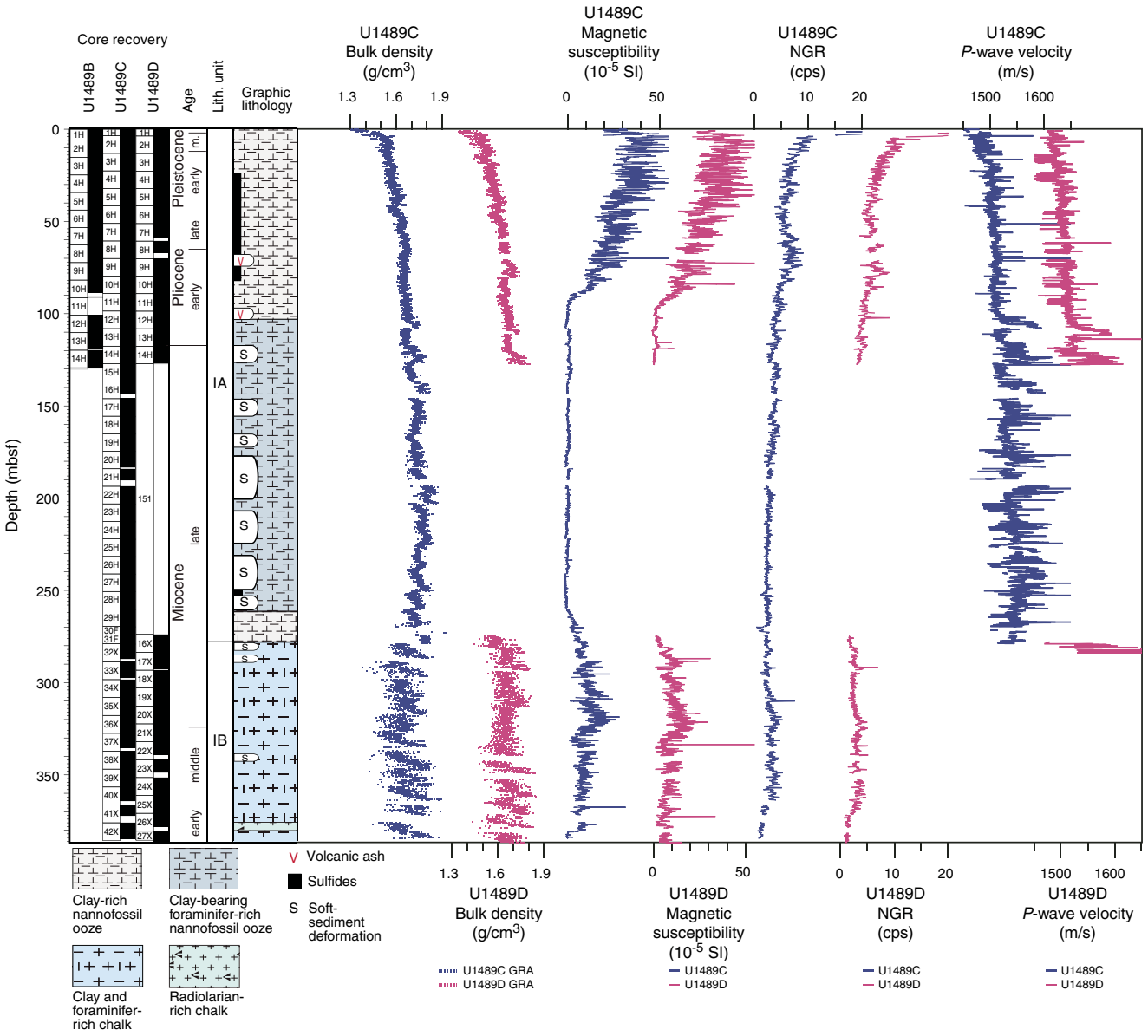

Table T11. Raw, cleaned, and detrended Whole-Round Multisensor Logger gamma ray attenuation (GRA) bulk density data, Hole U1489C. **Download table in CSV format.**

Table T12. Raw, cleaned, and detrended Whole-Round Multisensor Logger gamma ray attenuation (GRA) bulk density data, Hole U1489D. **Download table in CSV format.**

dropping to <1 count/s between 360 mbsf and the base of the hole. Although short-term 1–3 m variations in NGR are not strong, they are in phase with magnetic susceptibility and color variations, with higher NGR and magnetic susceptibility occurring in darker layers. This relationship is particularly prevalent in the upper 90 mbsf (Figure **F27**) and between 290 and 370 mbsf.

P-wave velocity

Measurements of PWL *P*-wave velocity were carried out for all holes at Site U1489. Because Holes U1489B and U1489C have continuous records with corresponding discrete samples, the PWL velocity data from these holes are used as representative for description purposes. PWL velocity data from Holes U1489B and U1489C increase downhole from 1480 to 1500 m/s over the upper 20 mbsf and from 1500 to 1520 m/s for the interval between 20 and 100 mbsf (Figure **F28**; Tables **T19**, **T20**, **T21**). Deeper than 100 mbsf, *P*-wave velocity shows ~10 m scale cycles, similar to those observed in GRA bulk density (Figure **F26**). In Hole U1489C, these ~10 m cycles start in Core 363-U1489C-12H and correspond to intervals of soft-sediment deformation (see **Core description**). In particular, these cycles, also observed in GRA density, occur in thick

Figure F27. WRMSL GRA bulk density, MS, NGR, and *P*-wave velocity overlaid on core photos (generated using Code for Ocean Drilling Data [CODD] [Wilkens et al., 2017]) from Hole U1489C between 18 and 58 mbsf. cps = counts per second.

Table T13. Raw and cleaned Whole-Round Multisensor Logger magnetic susceptibility (MS) data, Hole U1489B. **Download table in CSV format.**

Table T14. Raw and cleaned Whole-Round Multisensor Logger magnetic susceptibility (MS) data, Hole U1489C. **Download table in CSV format.**

Table T15. Raw and cleaned Whole-Round Multisensor Logger magnetic susceptibility (MS) data, Hole U1489D. **Download table in CSV format.**

Table T16. Raw and cleaned Natural Gamma Radiation Logger natural gamma radiation (NGR) data, Hole U1489B. **Download table in CSV format.**

Table T17. Raw and cleaned Natural Gamma Radiation Logger natural gamma radiation (NGR) data, Hole U1489C. **Download table in CSV format.**

Table T18. Raw and cleaned Natural Gamma Radiation Logger natural gamma radiation (NGR) data, Hole U1489D. **Download table in CSV format.**

homogeneous layers containing coarser grained foraminifer-rich sediment.

In general, PWC *x*-axis measurements reproduce the PWL measurements for both holes (Figure F28). PWC *x*-axis measurements extend the *P*-wave velocity record in Hole U1489C through the XCB

Figure F28. Comparison of discrete and whole-round *P*-wave velocity measurements, Holes U1489B and U1489C.

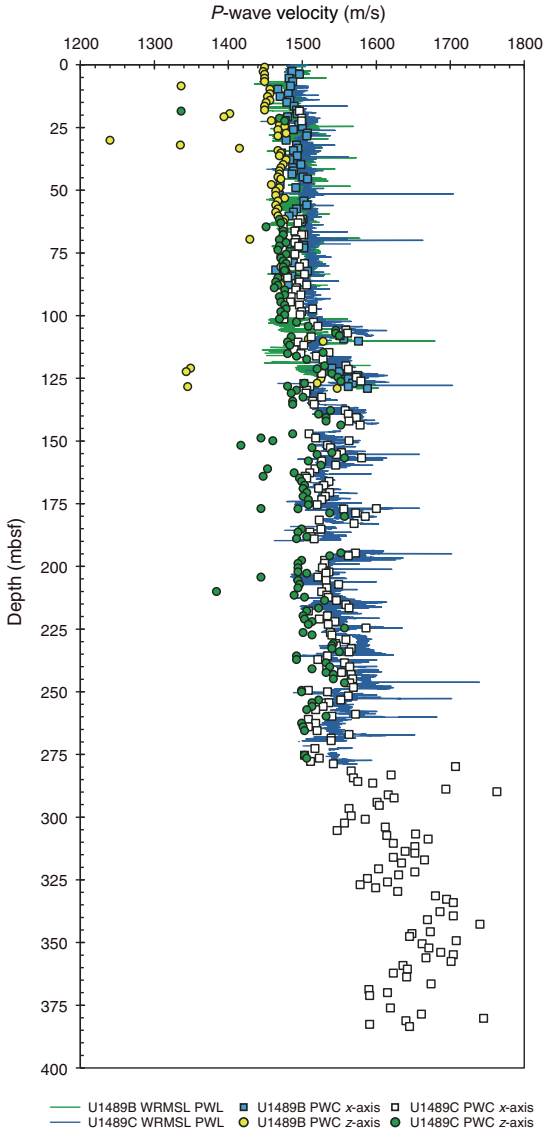

Table T19. Raw and cleaned Whole-Round Multisensor Logger *P*-wave logger data, Hole U1489B. **Download table in CSV format.**

Table T20. Raw and cleaned Whole-Round Multisensor Logger *P*-wave logger data, Hole U1489C. **Download table in CSV format.**

Table T21. Raw and cleaned Whole-Round Multisensor Logger *P*-wave logger data, Hole U1489D. **Download table in CSV format.**

cores, which exhibit distinctively high values mainly >1600 m/s, possibly caused by increased induration of the sediment. Below 100 mbsf, the 10 m scale variations observed in the PWL *P*-wave velocity and GRA bulk density records from Hole U1489C are also mostly captured in the PWC *x*- and *z*-axis *P*-wave velocity data. The PWC *z*-axis velocity record includes some outliers with velocities <1440 m/s for the upper 100 mbsf and <1480 m/s deeper than 100 mbsf.

Figure F29. MAD dry, bulk, and grain densities and porosity, WRMSL GRA bulk density, and thermal conductivity, Holes U1489B and U1489C. Yellow shading = interval in both holes disturbed by mechanical shearing of the shear pins prior to shooting the cores (see Operations).

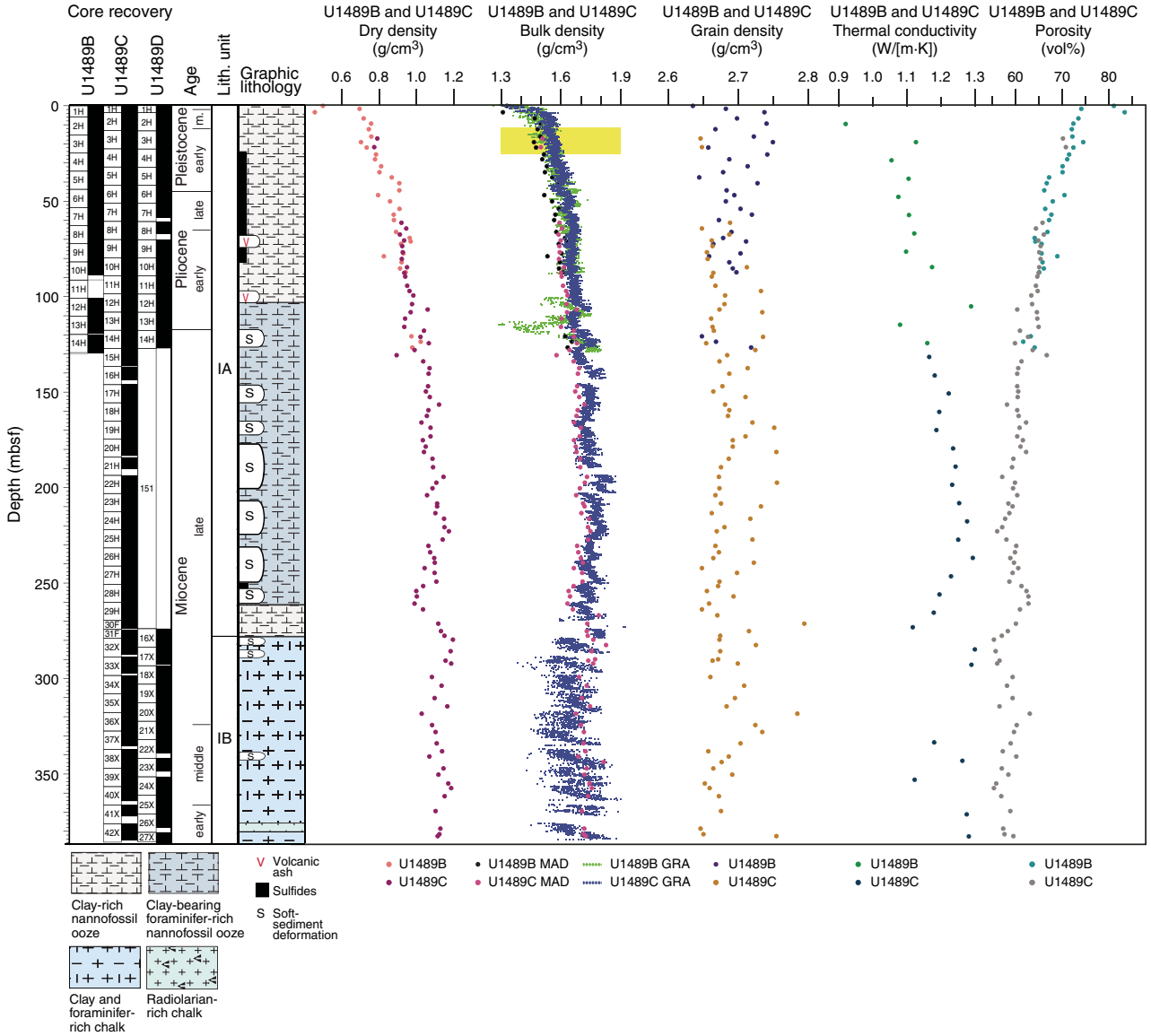

Moisture and density

Dry density, bulk density, and grain density curves show opposing trends to porosity in Holes U1489B and U1489C (Figure **F29**). Discrete MAD samples were measured in Hole U1489B for the upper ~130 mbsf and in Hole U1489C from ~70 mbsf to the bottom of the hole (~375 mbsf). Where measurements were obtained in both Holes U1489B and U1489C, the data show good reproducibility with the exception of the interval from Core 3H (~22–24 mbsf), which was affected by coring disturbance in both holes (yellow box in Figure **F29**) (see **Operations**).

The trends and variations in MAD and GRA bulk densities correspond well to each other, although MAD bulk density is offset from GRA bulk density by ~0.05 g/cm^3 in the upper 270 mbsf, comparable to the offset seen at Site U1488. Deeper than 270 mbsf (lithologic Subunit IB), the variability in GRA bulk density increases and MAD bulk density values correspond to the highest GRA bulk density values. As this interval consisted of indurated sediment cored with the XCB system, MAD bulk density probably reflects true bulk density, whereas GRA bulk density underestimates it because values were not corrected for the smaller diameter of XCB cores (see **Physical properties** in the Site U1482 chapter and **Physical properties** in the Expedition 363 methods chapter [Rosenthal et al., 2018b, 2018a]).

Following the same general trend as GRA and MAD bulk density, dry density increases from ~0.7 g/cm^3 just below the mudline to 1.2 g/cm^3 at 265 mbsf in Hole U1489C and then remains stable at ~1.2 g/cm^3 from 265 mbsf to the base of the hole. This higher density could correspond to a change in sediment compaction or lithification or potentially reflect a lithologic change shortly after XCB coring commenced. In general, porosity shows a decreasing trend with depth from 75% to 50%, whereas dry density increases with depth; this is similar to the relationship between porosity and density observed at previous sites and is associated with the compaction effect. The decreasing downhole trend in porosity is more

variable below 265 mbsf, coincident with the strongest changes in dry and bulk density. Grain density at Site U1489 has an average of ~2.7 g/cm^3 and ranges from 2.63 to 2.77 g/cm^3 deeper than 265 mbsf with no downhole trend.

Thermal conductivity

A thermal conductivity profile (Figure **F29**) was obtained at ~10 m resolution using a needle probe for the upper ~280 mbsf (Cores 363-U1489B-1H through 14H and Core 363-U1489C-15H through 30F. When the recovered material became indurated at ~280 mbsf (Core 363-U1489C-31F), a puck probe was used on split core sections (see **Physical properties** in the Expedition 363 methods chapter [Rosenthal et al., 2018a]). Thermal conductivity increases with depth from ~0.9 W/(m·K) at the seafloor to 1.3 W/(m·K) at ~265 mbsf, with an average value of 1.17 W/(m·K). From 265 mbsf to the bottom of the hole, values are more variable, with a relatively high average of ~1.3 W/(m·K). The relatively high thermal conductivity below ~280 mbsf corresponds to the interval where the sediment became too indurated and the puck method was required. However, because the increase occurred between two consecutive needle probe measurements, it most likely reflects a change in thermal conductivity caused by a change in the lithification of the sediment instead of an increase caused by different measurement methods. Thermal conductivity correlates with dry density and is inversely correlated with porosity (Figure **F29**) due to compaction. As at Site U1488, thermal conductivity exhibits a trend similar to that of luminosity (L*).

Downhole temperature measurements

Four downhole temperature measurements were collected using the advanced piston corer temperature tool (APCT-3) on Cores 363-U1489B-4H (34.2 mbsf), 7H (62.7 mbsf), 10H (91.2 mbsf), and 12H (110.2 mbsf). The downhole temperature values are generally very low: 2.57°–5.2°C (Figure **F30A**). Because of one anomalous measurement (Core 12H) and uncertainty regarding two others (Cores 4H and 7H), we collected additional downhole temperature measurements in Hole U1489D on Cores 363-U1489D-4H (32.2 mbsf), 7H (60.7 mbsf), 10H (89.2 mbsf), and 13H (117.7 mbsf). Temperature values are relatively low, with temperatures ranging from 2.51° to 4.16°C, which confirm the measurements obtained in Hole U1489B (Figure **F30B**). An exponential decrease in temperature was observed between 60 and 600 s after penetration and was used to estimate ambient temperature (unshaded area in Figure **F30**). The reproducibility in both profiles is good except for Core 363-U1489B-12H, which shows disturbance and was overestimated (Figures **F30A**, **F31A**). Because values in Hole U1489D remain more stable and show a very good correlation between the four downhole temperatures and depth (R^2 = 0.997), all subsequent calculations were made using the Hole U1489D downhole temperature measurements.

Figure F30. Comparison of APCT-3 temperature-time series. Unshaded area = time interval with exponential decrease in temperature. A. Hole U1489B. B. Hole U1489D.

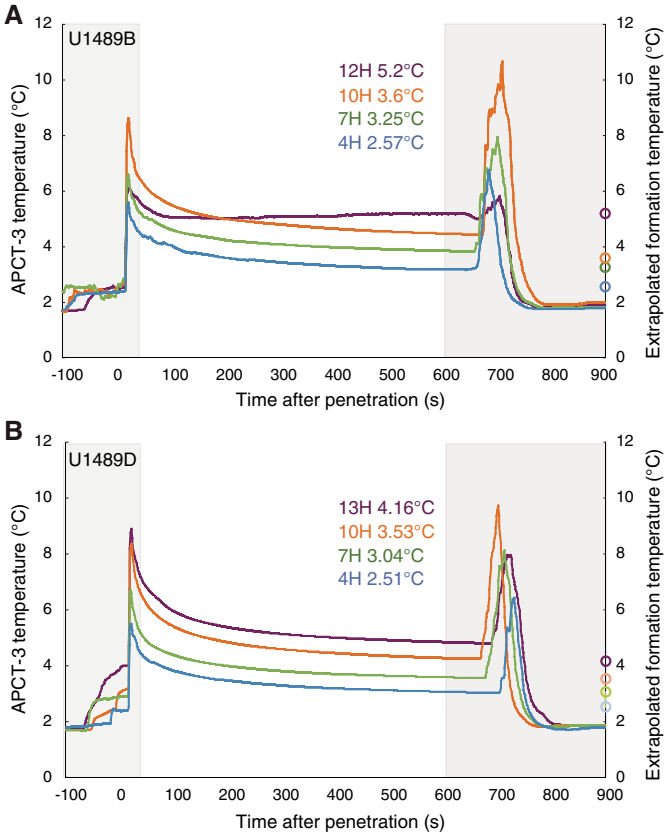

Using the slope of the temperature-depth relationship, we estimate that the bottom water temperature in Hole U1489D is 1.88°C, yielding a geothermal gradient of 19°C/km (Figure **F31B**). We generated a thermal conductivity profile with a resolution of ~10 m (Figure **F31C**) and calculated thermal resistance and an average corrected thermal conductivity of 1.17 W/(m·K) in Hole U1489D following the "average approach" outlined in Pribnow et al. (2000). The corrected thermal conductivity is lower than uncorrected values with an offset of ~0.04 W/(m·K) at the top and a decreasing offset with depth. The slope of the linear fit between temperature and thermal resistance indicates a heat flow of 22 mW/m^2 at Site U1489. As at Site U1488, the classic approach for calculating the ocean-crust age is inappropriate. The observed conductive heat flow in such areas must therefore be adjusted upward to be indicative of the true crustal heat flow; however, this calculation was not performed here.

Figure F31. Heat flow calculations, Holes U1489B and U1489D. A. Sediment temperature profile, Hole U1489B. The anomalous measurement for Core 12H is circled. B. Sediment temperature profile, Hole U1489D. C. Thermal conductivity data from Holes U1489B and U1489C. Green line = calculated thermal resistance; gray vertical line = average thermal conductivity value used for calculation of thermal resistance; black diamonds and dashed line = corrected thermal conductivity; open, light blue, and dark blue diamonds = uncorrected thermal conductivity.

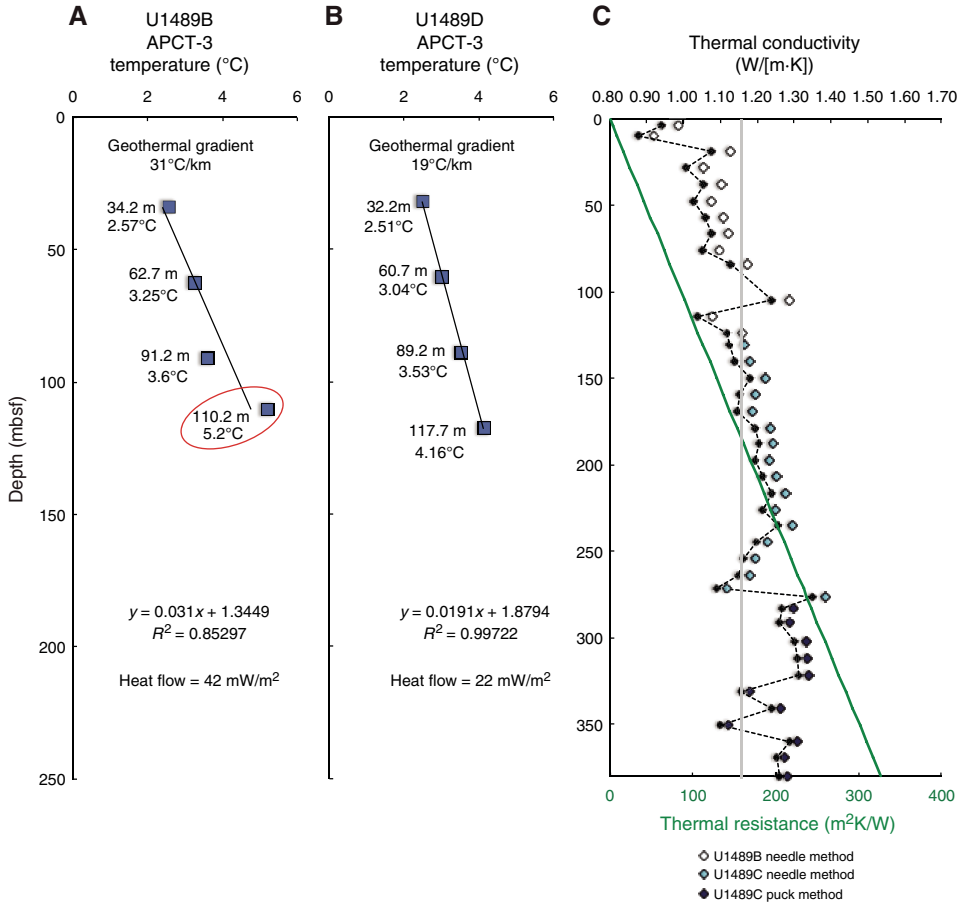

Stratigraphic correlation

Correlations between holes at Site U1489 were accomplished using Correlator software (version 2.1). Tie points were established mainly using WRMSL magnetic susceptibility data (Figure **F32**; Table **T22**). In addition, we used WRMSL GRA bulk density and PWL data, NGR data, and luminosity (L*) data. We constructed a splice for the site using Holes U1489A, U1489B, U1489C, and U1489D (Table **T23**; Figures **F32**, **F33**). The splice is continuous and well constrained from 0 to 140.95 m core composite depth below seafloor (CCSF). There is an interval from 140.95 to 305.70 m CCSF without a splice because it was recovered only in Hole U1489C. In Hole U1489D, there was a drilled interval with no recovery from 137.87 to 305.70 m CCSF, which was followed by coring below that depth over the same interval cored in Hole U1489C. This allowed us to construct a splice from 305.70 to 371.25 m CCSF using cores from Holes U1489C and U1489D, although there are tentative tie points (Table **T22**) that should be verified during postcruise research. Below the bottom of the splice (371.25 m CCSF), core offsets from Hole U1489C were set using a growth factor, and several cores in Hole U1489D could be tied to Hole U1489C, as explained below.

The CCSF scale is anchored to the mudline of Core 363-U1489D-1H, which is assigned a depth of 0 m CCSF. From this anchor, we worked downhole, using Correlator to establish a composite stratigraphy on a core-by-core basis. In the upper part of the splice we primarily used magnetic susceptibility to establish tie points; however, the amplitude of the magnetic susceptibility variations greatly diminished below about 100 m CCSF, and GRA bulk density, PWL, L*, and NGR data were needed to correlate between holes (Tables **T22**, **T23**).

Hole U1489B, which spans the interval from 0 to ~129 mbsf (equivalent to 0 to ~140 m CCSF), was heavily sampled (one 5 or 10 cm whole-round sample per section) for high-resolution interstitial water analysis, so our general approach was to avoid using material from Hole U1489B. In the upper spliced interval (0–140.95 m CCSF), we used cores from Hole U1489D as the "backbone" of the splice and then used smaller intervals from Hole U1489C to cover the core gaps in Hole U1489D. However, because of coring disturbance in Core 363-U1489C-3H, we decided not to include it in the splice and had to use a small portion of Core 363-U1489B-3H instead. In addition, core gaps resulting from poor recovery in Cores 363-U1489D-7H and 8H were covered by large portions of Cores 363-U1489C-7H and 8H (Table **T22**; Figure **F32**).

From 140.95 to 305.70 m CCSF, the interval in which cores were recovered only in Hole U1489C, core offsets were determined using 1.124, the average growth factor of Cores 363-U1489C-10H through 14H, which are part of the overlying spliced interval. We applied

Figure F32. WRMSL MS data for Holes U1489A–U1489D divided into 50 m intervals. The MS vertical scale varies between the 50 m graph segments. Upper panel shows the MS splice constructed by combining data from all holes for the upper and lower splice intervals. (Continued on next two pages.)

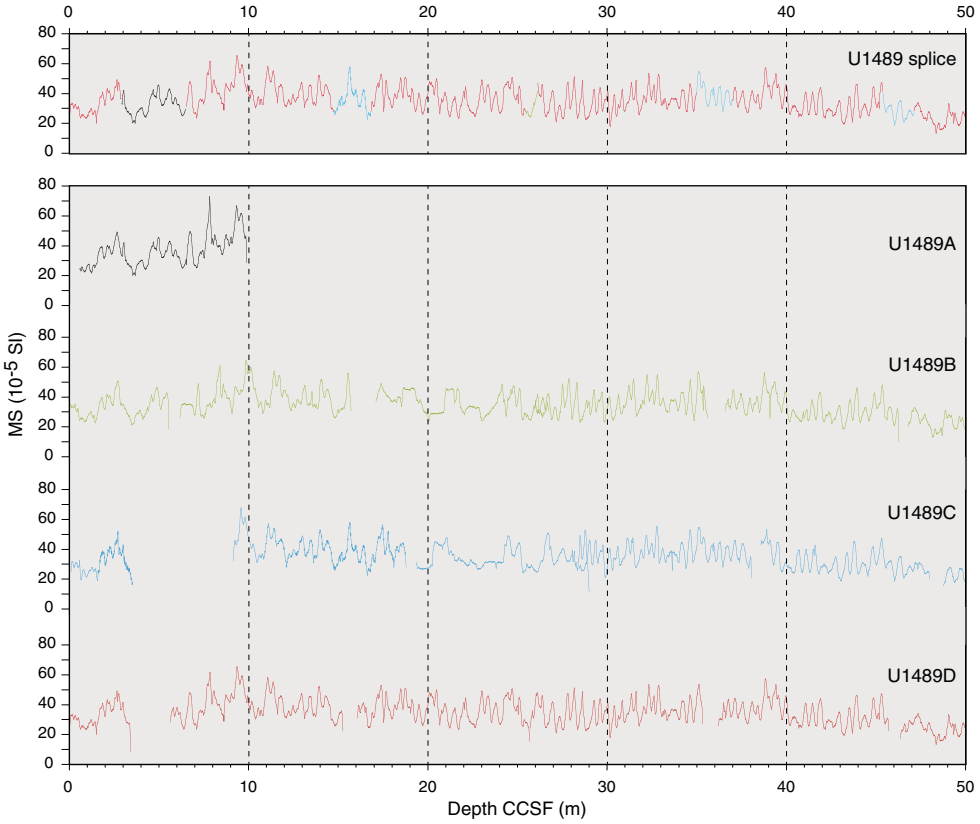

this same growth factor to Cores 363-U1489C-15H through 31F. The offset for Core 363-U1489D-16X, the first core recovered after drilling down to 274 mbsf in Hole U1489D, was determined by correlating it to Core 363-U1489C-31F. Thus, the top of Core 363-U1489D-16X is the top of the second spliced interval that extends from 305.70 to 371.25 m CCSF. The tie points between holes used to construct the splice in this interval were very difficult to determine. Magnetic susceptibility and L* were primarily used to determine the tie points in this interval, although NGR and GRA bulk density were helpful in some intervals. Several of the tie points are tentative (Table **T22**) and should be verified during postcruise research. Below 371.25 m CCSF, which is the bottom of Core 363-U1489D-22X, there are core gaps, and thus this depth marks the bottom of the spliced interval. Offsets for cores below 371.25 m CCSF were determined as follows: offsets for Cores 363-U1489C-38X through 42X were determined using a growth factor of 1.104, which is the growth factor of Core 363-U1489C-37X. The offsets for Cores 363-U1489D-23X through 27X were determined by correlating them to Cores 363-U1489C-38X through 42X.

The splice interval table (Table **T23**) is intended to provide a sampling plan that can be used to generate high-resolution continuous records with minimal gaps; however, an "off-splice" sampling plan was also designed, mainly for low-resolution studies. An explanation of the strategy used to determine the off-splice sampling plan and a table of core intervals that should be used for off-splice sampling can be found in OFFSPLICE in **Supplementary material**.

The cumulative offset between mbsf and CCSF depth scales is nearly linear (Figure **F34A**). The growth factor is relatively low (8%–9%), as expected in sediment that expands due to the release of overburden and has minimal gas expansion due to low concentrations of methane and other gases (see **Geochemistry**). There are marked changes in the growth factor, and therefore in the cumulative offset with depth (Figure **F34B**), in the interval cored with the XCB system deeper than ~274 mbsf. These changes are probably due to soft-sediment deformation rather than coring (see **Core description**), which caused hole-to-hole differences in the thickness of sediment packages. Calculation of mass accumulation rates based on the CCSF scale should account for differential expansion by dividing apparent depth intervals by the appropriate growth factor.

Figure F32 (continued). (Continued on next page.)

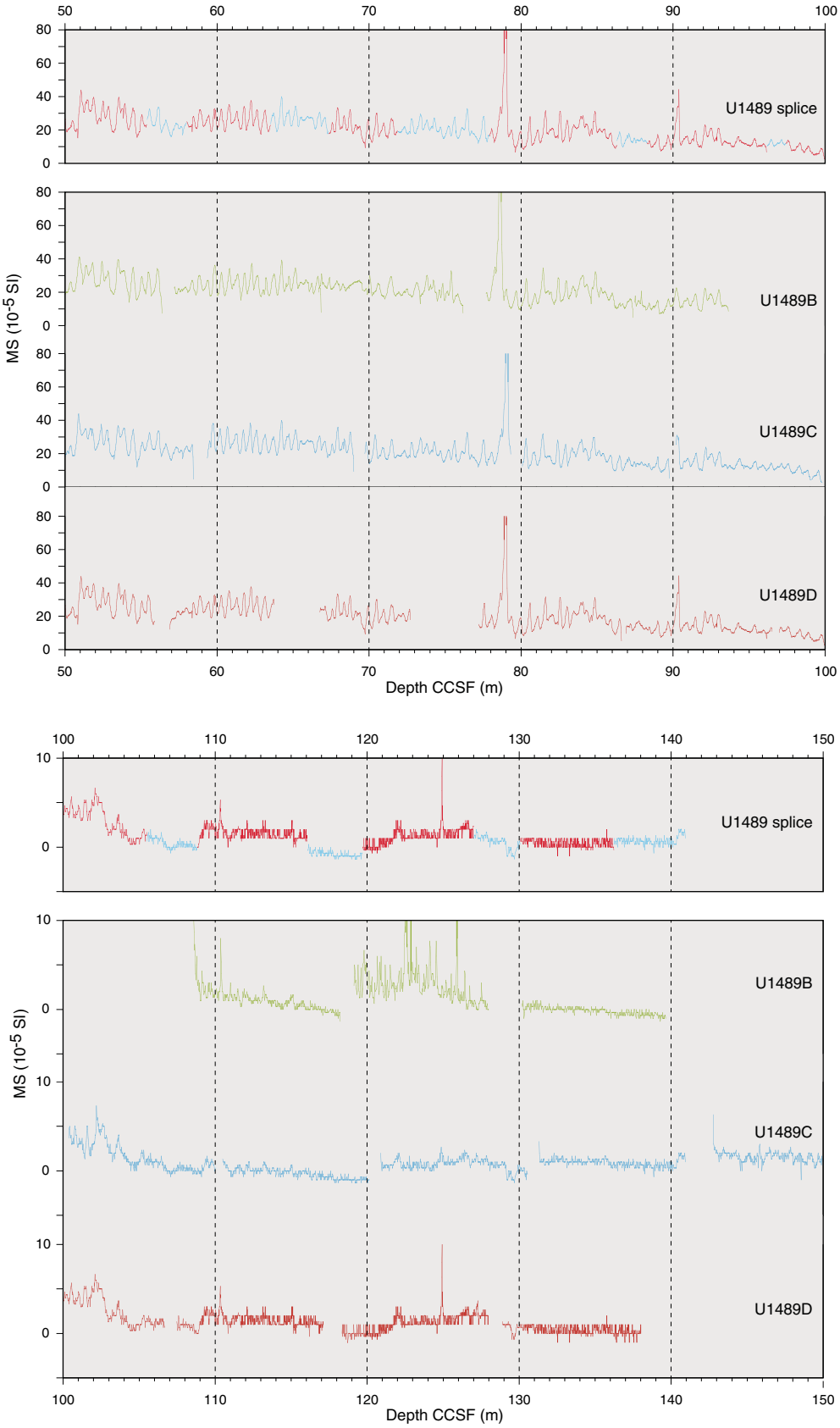

Figure F32 (continued).

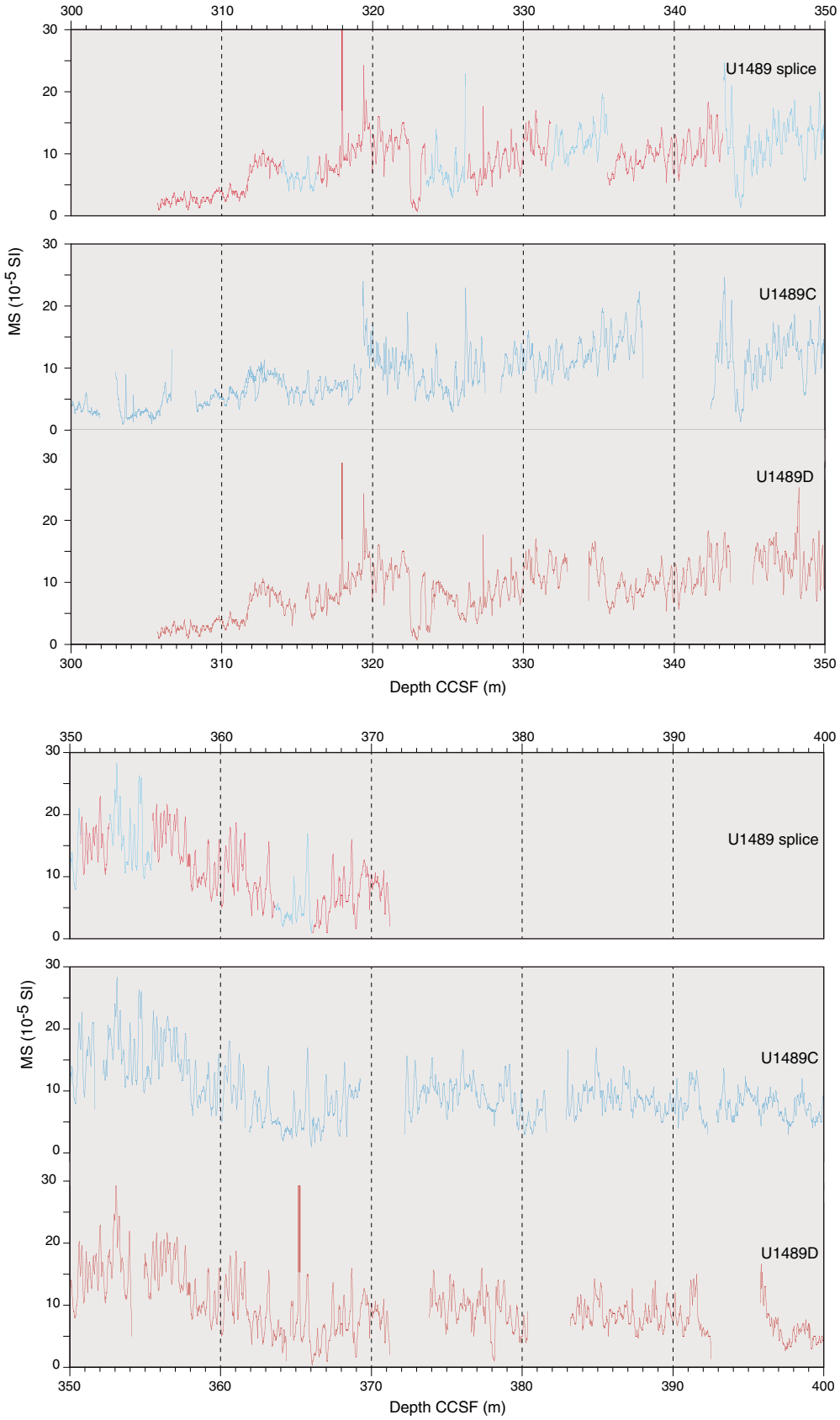

Table T22. Affine table, Site U1489. * = uncertain tie point. GF = growth factor. GRA = gamma ray attenuation, MS = magnetic susceptibility. **Download table in CSV format.**

Core	Depth (mbsf)	Depth CCSF (m)	Offset (m)	Tied to point depth CCSF (m)	Shift type	Data used	Reference hole, core
363-U1489A-							363-
1H	0.00	0.54	0.54	2.887	Set	MS	U1489D-1H
363-U1489B-							
1H	0.00	−0.02	−0.02	2.887	Tied to	MS	U1489D-1H
2H	5.70	6.14	0.44	14.760	Tied to	MS	U1489D-2H
3H	15.20	17.08	1.88	34.977	Tied to	MS	U1489D-3H
4H	24.70	25.95	1.25	45.392	Tied to	MS	U1489D-4H
5H	34.20	36.60	2.40	55.388	Tied to	MS	U1489D-5H
6H	43.70	46.78	3.08	63.521	Tied to	MS	U1489D-6H
7H	53.20	57.16	3.96	63.521	Tied to	MS	U1489D-7H
8H	62.70	66.65	3.95	71.871	Tied to	MS	U1489D-8H
9H	72.20	77.67	5.47	83.981	Tied to	MS	U1489D-9H
10H	81.70	87.46	5.76	88.285	Tied to	MS	U1489C-9H
12H	100.70	108.57	7.87	115.304	Tied to	MS	U1489D-12H
13H	110.20	119.10	8.90	124.565	Tied to	GRA	U1489C-13H
14H	119.70	130.18	10.48	136.240	Tied to	GRA	U1489D-14H
363-U1489C-							363-
1H	0.00	0.07	0.07	2.887	Tied to	MS	U1489D-1H
2H	3.50	9.12	5.62	14.760	Tied to	MS	U1489D-2H
3H	13.00	19.31	6.31	25.437	Tied to	MS	U1489D-3H
4H	22.50	28.41	5.91	34.977	Tied to	MS	U1489D-4H
5H	32.00	38.56	6.56	45.392	Tied to	MS	U1489D-5H
6H	41.50	48.75	7.25	55.388	Tied to	MS	U1489D-6H
7H	51.00	59.35	8.35	63.521	Tied to	MS	U1489D-7H
8H	60.50	69.70	9.20	71.871	Tied to	MS	U1489D-8H
9H	70.00	80.07	10.07	86.308	Tied to	MS	U1489D-9H
10H	79.50	90.16	10.66	96.156	Tied to	MS	U1489D-10H
11H	89.00	100.35	11.35	105.521	Tied to	GRA	U1489D-11H
12H	98.50	110.48	11.98	116.084	Tied to*	L*	U1489D-12H
13H	108.00	120.86	12.86	127.000	Tied to	MS	U1489D-13H
14H	117.50	131.29	13.79	136.240	Tied to	GRA	U1489D-14H
15H	127.00	142.75	15.75		Set; GF = 1.124		U1489C-14H
16H	136.50	153.43	16.93		Set; GF = 1.124		U1489C-15H
17H	146.00	164.11	18.11		Set; GF = 1.124		U1489C-16H
18H	155.50	174.79	19.29		Set; GF = 1.124		U1489C-17H
19H	165.00	185.46	20.46		Set; GF = 1.124		U1489C-18H
20H	174.50	196.14	21.64		Set; GF = 1.124		U1489C-19H
21H	184.00	206.82	22.82		Set; GF = 1.124		U1489C-20H
22H	193.50	217.50	24.00		Set; GF = 1.124		U1489C-21H
23H	203.00	228.18	25.17		Set; GF = 1.124		U1489C-22H
24H	212.50	238.85	26.35		Set; GF = 1.124		U1489C-23H
25H	222.00	249.53	27.53		Set; GF = 1.124		U1489C-24H
26H	231.50	260.21	28.71		Set; GF = 1.124		U1489C-25H
27H	241.00	270.89	29.89		Set; GF = 1.124		U1489C-26H
28H	250.50	281.57	31.07		Set; GF = 1.124		U1489C-27H
29H	260.00	292.24	32.24		Set; GF = 1.124		U1489C-28H
30F	269.50	302.92	33.42		Set; GF = 1.124		U1489C-29H
31F	274.20	308.20	34.00		Set; GF = 1.124		U1489C-30F
32X	278.90	311.46	32.56	313.941	Tied to*	L*	U1489D-16X
33X	288.60	319.30	30.70	323.528	Tied to	L*	U1489D-17X
34X	298.30	328.48	30.18	331.831	Tied to*	L*	U1489D-18X
35X	308.00	342.38	34.38	343.236	Tied to*	L*	U1489D-19X
36X	317.70	352.17	34.47	352.624	Tied to	MS	U1489D-20X
37X	327.40	361.89	34.49	363.612	Tied to	MS	U1489D-21X
38X	337.10	372.16	35.06		Set; GF = 1.104		U1489C-37X
39X	346.80	382.87	36.07		Set; GF = 1.104		U1489C-38X
40X	356.50	392.87	36.37		Set; GF = 1.104		U1489C-39X
41X	366.20	404.29	38.09		Set; GF = 1.104		U1489C-40X
42X	375.90	415.00	39.10		Set; GF = 1.104		U1489C-41X
363-U1489D-							363-
1H	0.00	0.00	0.00	Mudline			
2H	3.70	5.61	1.91	6.494	Tied to	MS	U1489A-1H
3H	13.20	16.05	2.85	16.817	Tied to	MS	U1489C-2H
4H	22.70	25.68	2.98	26.122	Tied to	MS	U1489B-3H
5H	32.20	36.20	4.00	36.992	Tied to	MS	U1489D-4H
6H	41.70	46.35	4.65	47.125	Tied to	MS	U1489C-5H
7H	51.20	56.86	5.66	58.004	Tied to	MS	U1489C-6H
8H	60.70	66.74	6.04	67.350	Tied to	MS	U1489C-7H
9H	70.20	77.19	6.99	77.909	Tied to	MS	U1489C-8H
10H	79.70	86.87	7.17	88.285	Tied to	MS	U1489C-9H
11H	89.20	96.96	7.76	97.418	Tied to	MS	U1489C-10H
12H	98.70	107.46	8.76	108.817	Tied to	PWL	U1489C-11H
13H	108.20	118.32	10.12	119.681	Tied to	L*	U1489C-12H
14H	117.70	128.87	11.17	130.068	Tied to	GRA	U1489C-13H
16X	274.00	305.70	31.70	305.697	Tied to	MS	U1489C-31F
17X	283.70	315.50	31.80	316.315	Tied to	MS	U1489C-32X
18X	293.40	323.97	30.57	326.289	Tied to*	MS	U1489C-33X
19X	303.10	334.30	31.20	335.574	Tied to*	L*	U1489C-34X
20X	312.80	345.19	32.39	350.721	Tied to	MS	U1489C-35X
21X	322.50	354.91	32.41	355.463	Tied to	MS	U1489C-36X
22X	332.20	364.59	32.39	366.071	Tied to	MS	U1489C-37X
23X	341.90	373.83	31.93	375.442	Tied to*	MS	U1489C-38X
24X	351.60	383.18	31.58	390.737	Tied to	MS	U1489C-39X
25X	361.30	395.78	34.48	398.689	Tied to	L*	U1489C-40X
26X	371.00	404.82	33.82	405.471	Tied to*	MS	U1489C-41X
27X	380.70	414.21	33.51	416.492	Tied to*	L*	U1489C-42X

Table T23. Splice interval, Site U1489. MS = magnetic susceptibility, GRA = gamma ray attenuation, PWL = *P*-wave logger *P*-wave velocity. **Download table in CSV format.**

Top of splice interval			Bottom of splice interval				
Hole, core, section, interval (cm)	Depth (mbsf)	Depth CCSF (m)	Hole, core, section, interval (cm)	Depth (mbsf)	Depth CCSF (m)	Splice type	Data used
363-			363-				
U1489D-1H-1, 0.00	0.00	0.00	U1489D-1H-3, 18.40	2.88	2.89	Tie	MS
U1489A-1H-2, 84.60	2.35	2.89	U1489A-1H-4, 145.30	5.95	6.49	Tie	MS
U1489D-2H-1, 88.00	4.58	6.49	U1489D-2H-7, 14.60	12.85	14.76	Tie	MS
U1489C-2H-4, 113.70	9.14	14.76	U1489C-2H-6, 19.40	11.19	16.82	Tie	MS
U1489D-3H-1, 77.10	13.97	16.82	U1489D-3H-7, 39.10	22.59	25.44	Tie	MS
U1489B-3H-6, 86.00	23.56	25.44	U1489B-3H-7, 4.50	24.25	26.12	Tie	MS
U1489D-4H-1, 44.10	23.14	26.12	U1489D-4H-7, 29.60	32.00	34.98	Tie	MS
U1489C-4H-5, 56.80	29.07	34.98	U1489C-4H-6, 108.30	31.08	36.99	Tie	MS
U1489D-5H-1, 79.40	32.99	36.99	U1489D-5H-7, 19.40	41.39	45.39	Tie	MS
U1489C-5H-5, 83.10	38.83	45.39	U1489C-5H-6, 106.40	40.56	47.13	Tie	MS
U1489D-6H-1, 77.50	42.48	47.13	U1489D-6H-7, 3.80	50.74	55.39	Tie	MS
U1489C-6H-5, 63.40	48.13	55.39	U1489C-6H-7, 25.00	50.75	58.00	Tie	MS
U1489D-7H-1, 113.90	52.34	58.00	U1489D-7H-5, 65.60	57.86	63.52	Tie	MS
U1489C-7H-3, 117.50	55.18	63.52	U1489C-7H-6, 50.40	59.00	67.35	Tie	MS
U1489D-8H-1, 60.70	61.31	67.35	U1489D-8H-4, 62.80	65.83	71.87	Tie	MS
U1489C-8H-2, 67.00	62.67	71.87	U1489C-8H-6, 70.80	68.71	77.91	Tie	MS
U1489D-9H-1, 71.40	70.91	77.91	U1489D-9H-7, 31.30	79.31	86.31	Tie	MS
U1489C-9H-5, 23.90	76.24	86.31	U1489C-9H-6, 71.60	78.22	88.29	Tie	MS
U1489D-10H-1, 141.70	81.12	88.29	U1489D-10H-7, 28.80	88.99	96.16	Tie	MS
U1489C-10H-4, 149.70	85.50	96.16	U1489C-10H-5, 125.90	86.76	97.42	Tie	MS
U1489D-11H-1, 45.80	89.66	97.42	U1489D-11H-6, 106.10	97.76	105.52	Tie	GRA
U1489C-11H-4, 67.30	94.17	105.52	U1489C-11H-6, 96.90	97.47	108.82	Tie	PWL
U1489D-12H-1, 135.70	100.06	108.82	U1489D-12H-6, 112.40	107.32	116.08	Tie	MS
U1489C-12H-4, 110.80	104.11	116.08	U1489C-12H-7, 20.50	107.71	119.68	Tie	L*
U1489D-13H-1, 135.90	109.56	119.68	U1489D-13H-6, 117.80	116.88	127.00	Tie	MS
U1489C-13H-5, 14.10	114.14	127.00	U1489C-13H-7, 20.90	117.21	130.07	Tie	GRA
U1489D-14H-1, 119.30	118.89	130.07	U1489D-14H-5, 136.50	125.07	136.24	Tie	GRA
U1489C-14H-4, 44.60	122.45	136.24	U1489C-14H-7, 66.00	127.16	140.95	Set	
U1489D-16X-1, 0.00	274.00	305.70	U1489D-16X-6, 74.40	282.24	313.94	Tie	L*
U1489C-32X-2, 98.40	281.38	313.94	U1489C-32X-4, 35.80	283.76	316.32	Tie	MS
U1489D-17X-1, 81.20	284.51	316.32	U1489D-17X-6, 52.50	291.73	323.53	Tie	L*
U1489C-33X-4, 113.80	292.83	323.53	U1489C-33X-6, 89.90	295.59	326.29	Tie	MS
U1489D-18X-2, 81.90	295.72	326.29	U1489D-18X-6, 36.10	301.26	331.83	Tie	L*
U1489C-34X-3, 34.80	301.65	331.83	U1489C-34X-5, 109.10	305.39	335.57	Tie	L*
U1489D-19X-1, 127.00	304.37	335.57	U1489D-19X-7, 23.20	312.03	343.24	Tie	L*
U1489C-35X-1, 85.10	308.85	343.24	U1489C-35X-6, 83.60	316.34	350.72	Tie	MS
U1489D-20X-4, 103.30	318.33	350.72	U1489D-20X-5, 143.60	320.24	352.62	Tie	MS
U1489C-36X-1, 45.00	318.15	352.62	U1489C-36X-3, 28.90	320.99	355.46	Tie	MS
U1489D-21X-1, 55.70	323.06	355.46	U1489D-21X-6, 120.60	331.21	363.61	Tie	MS
U1489C-37X-2, 22.50	329.13	363.61	U1489C-37X-3, 118.40	331.58	366.07	Tie	MS
U1489D-22X-1, 148.50	333.69	366.07	U1489D-22X-5, 66.00	338.86	371.25		

Figure F33. Spliced L*, NGR, and WRMSL MS and GRA bulk density data, Site U1489 for the (A) upper and (B) lower splice intervals. cps = counts per second.

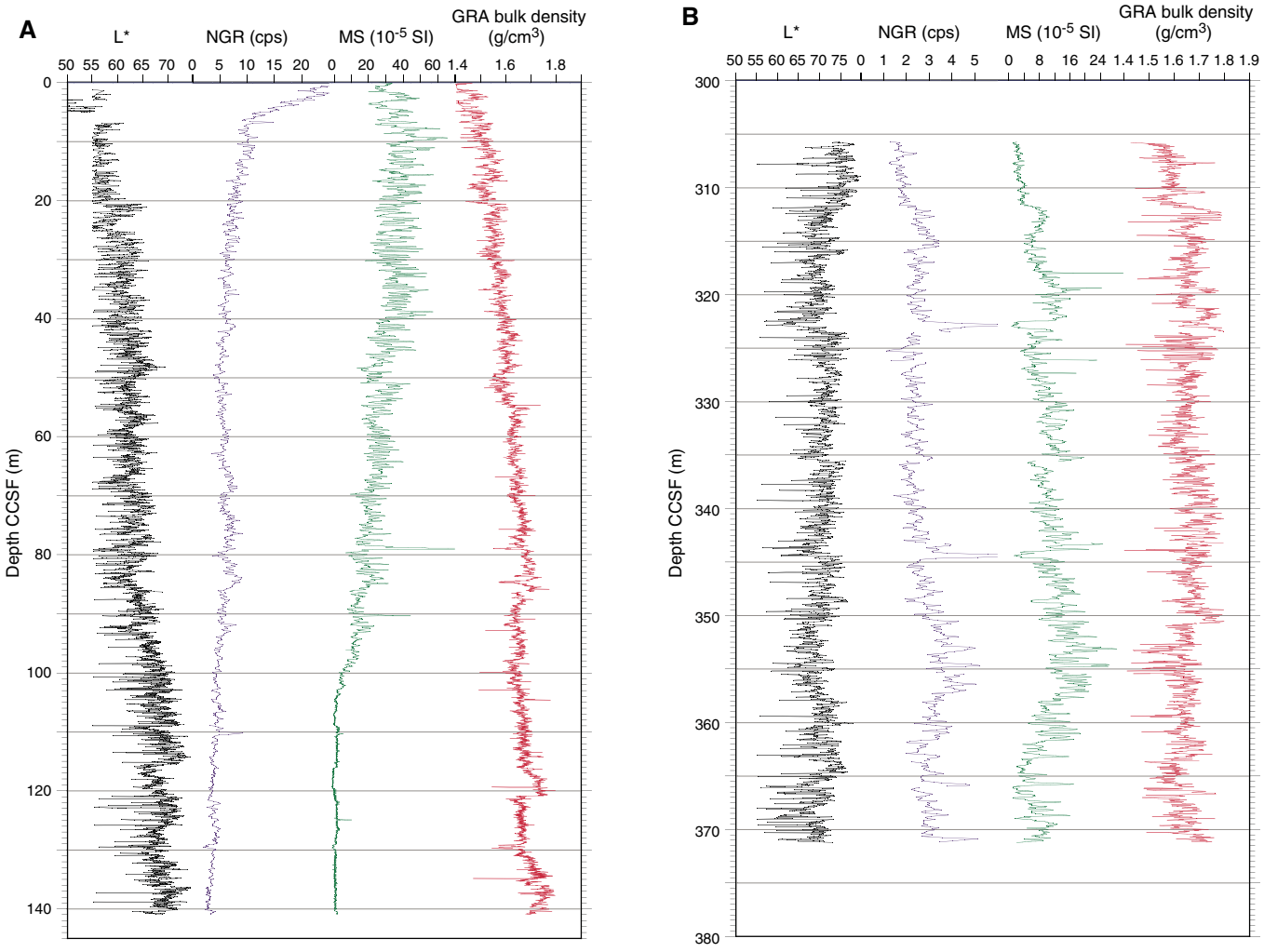

Figure F34. A. Comparison of mbsf and composite depth scales in the Site U1489 splice. B. Comparison of the growth of cumulative depth offset and mbsf depth scale.

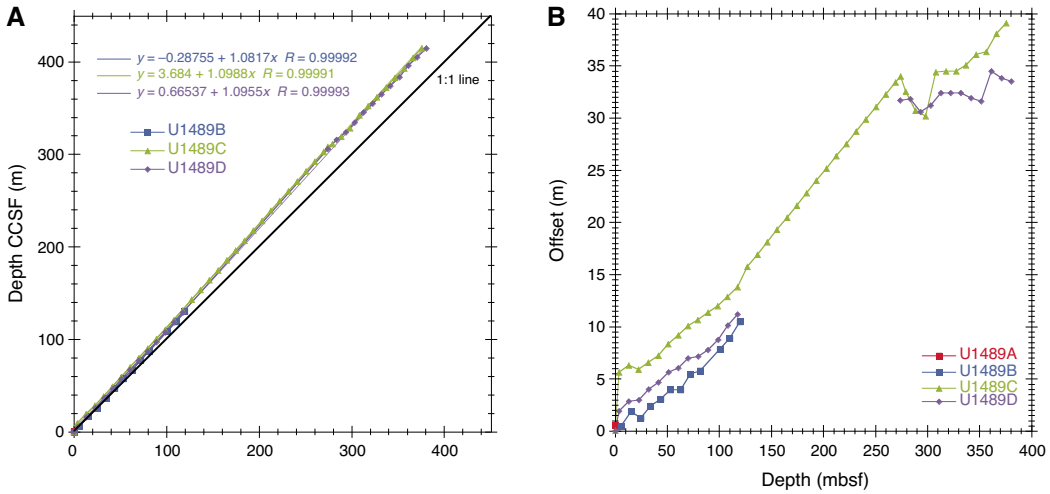

Geochemistry

Site U1489 was drilled on the western flank of the Eauripik Rise in the Caroline Basin at a water depth of 3421 m, ~81 km west-northwest of Site U1488. High-resolution interstitial water sampling was conducted in the upper ~82 mbsf at this site with the goal of reconstructing chlorinity (Cl) and $\delta^{18}O$ profiles of the Lower Circumpolar Deepwater (LCDW) during the LGM. The interstitial water profiles are largely controlled by carbonate diagenesis with a minor influence of organic matter remineralization apparent in the uppermost 50 mbsf. Preliminary shipboard Cl measurements suggest that reconstruction of the salinity of the LCDW will be possible with the samples collected at this site. For detailed background on organic matter remineralization and clay mineral alteration, see **Geochemistry** in the Site U1482 chapter (Rosenthal et al., 2018b). Carbonate ($CaCO_3$) content ranges from 50 to >90 wt% with an average of 82 wt%. Total organic carbon (TOC) is low (average = 0.14 wt%) and varies between 0 and 0.8 wt%. Because total nitrogen (TN) is close to the detection limit, the C/N ratio estimates are considered to be unreliable and therefore are excluded from this report.

Results

Volatile hydrocarbons

Headspace gas samples were taken at a frequency of one sample per core in Holes U1489B and U1489C as part of the routine environmental protection and safety-monitoring program (Table **T24**; Figure **F35**). Overall, methane concentration is low (<9 ppmv) throughout Holes U1489B and U1489C, consistent with the elevated concentration of dissolved sulfate (SO_4) throughout the entire hole (see **Sulfate and barium**); however, the methane profile exhibits a downhole increasing trend, suggesting increased production and/or decreased consumption in the lower part of the hole. Ethane and propane are below detection limit, suggesting a biogenic origin of methane.

Bulk sediment geochemistry

$CaCO_3$ content was measured on sediment samples from Holes U1489B and U1489C (Table **T25**; Figure **F35**). In general, $CaCO_3$ is the dominant component of the sediment at Site U1489, with an average of 82 wt%. $CaCO_3$ content increases with depth from ~50 wt% at the top to >90 wt% by ~120 mbsf. From ~120 to ~250 mbsf, $CaCO_3$ content is nearly constant at ~90 wt%. Below ~250 mbsf, $CaCO_3$ content decreases slightly and remains fairly invariable. TOC content ranges from 0 to 0.8 wt% with an average of 0.14 wt% over the entire sediment sequence. With the exception of the shallowest measurement (0.4 mbsf; 0.8 wt%), almost all samples have values <0.5 wt%. TN was detected in trace amounts (<0.1 wt%) throughout the hole. Because both TOC and TN contents are low, the C/N ratio is not reliable at this site and is not reported.

Interstitial water chemistry

A total of 100 whole-round samples and 1 mudline sample were taken at Site U1489: 69 samples from Hole U1489B and 32 samples from Hole U1489C. High-resolution interstitial water sampling was conducted in the upper ~82 mbsf of Hole U1489B with the goal of reconstructing Cl and $\delta^{18}O$ profiles in the LCDW during the LGM. Because of coring problems and sediment disturbances deeper than ~90 mbsf in Hole U1489B, interstitial water sampling was resumed at 88 mbsf in Hole U1489C and continued to near the bottom of the hole (deepest sample taken at 381.8 mbsf) at a frequency of one sample per core. We found small but nonetheless significant offsets in the geochemical profiles between the two sites (dashed line in Figures **F36**, **F37**). The offsets are especially visible in the profiles of Cl, phosphate (PO_4), potassium (K), and boron (B) and should be accounted for when interpreting these profiles. A total of 50 samples were analyzed on the ship following the procedures described in **Geochemistry** in the Expedition 363 methods chapter (Rosenthal et al., 2018a). Interstitial water chemistry data are reported in Table **T26**.

Table T24. Volatile hydrocarbon concentrations, Holes U1489B and U1489C. **Download table in CSV format.**

Chlorinity and salinity

Cl at Site U1489 is similar to that at Site U1488 and displays considerable variability, with values ranging between ~546 and ~564 mM (Figure **F36**). Cl increases from a mudline value of 553.8 mM to a maximum of ~563 mM between 33.6 and 43.1 mbsf and then decreases to ~550 mM at 71.6–81.1 mbsf. The peak in the chlorinity profile observed between 24 and 58 mbsf most likely represents the LGM peak in Cl. A sharp increase in Cl observed at ~88 mbsf corresponds to the depth at which we began taking interstitial water measurements from Hole U1489C and likely reflects differences between the two holes or procedural offsets in the extraction and analysis of the samples. Deeper than ~88 mbsf, Cl exhibits an overall downhole trend toward slightly lower values (~546 mM at 381.8 mbsf) interspersed with fluctuations of up to 10 mM. Salinity at Site U1489 exhibits minor downhole variations (not shown). The upper ~55 mbsf is characterized by salinity values of 37, whereas most of the underlying sediment sequence displays a salinity of 36, except deeper than 326 mbsf, where salinity increases to 36.5–37.

Alkalinity and pH

As observed at Site U1488, alkalinity increases from a mudline value of 2.5 mM to 3.5 mM in the subsequent sample at 4.4 mbsf (Figure **F36**) and then increases gradually and fairly linearly to a maximum concentration of 5.7 mM at 211.9 mbsf. Below 211.9 mbsf, alkalinity decreases gradually to 5.2 mM at 381.8 mbsf. From the mudline to 14.6 mbsf, pH decreases steadily from 7.8 to 7.5, before increasing toward a broad maximum of ~7.6 between 43 and 67 mbsf (Figure **F36**). As at Site U1488, the interstitial water pH profile shows an inverse relationship to alkalinity, with a gradual decrease toward lower values of ~7.5 at ~200 mbsf and near-constant values below that depth to near the base of the hole at 381.8 mbsf.

Sulfate and barium

The SO_4 concentration decreases from a seawater-like value of 29.1 mM at the mudline to a minimum of 22.4 mM at 200.9 mbsf (Figure **F36**). The curvature in the SO_4 profile throughout this interval indicates that sulfate reduction is driven by early diagenetic degradation of organic matter. Interestingly, deeper than 200.9 mbsf sulfate increases to a concentration of 24.4 mM at the base of Hole U1489C. As at Site U1488, the linear nature of this increase suggests diffusion from sulfate-rich fluids at depth (see **Discussion**). At Site U1489, barium (Ba) concentration remains very low throughout the hole, ranging from 0.06 to 0.26 µm (Figure **F36**). Ba increases slightly downhole, which could reflect progressive release of Ba from organic matter remineralization.

Phosphate, ammonium, and bromide

Phosphate concentration is very low at Site U1489, with values <5 µM observed throughout. PO_4 decreases abruptly from 4.3 µM

Figure F35. Methane, carbonate, TOC, and TN, Holes U1489B and U1489C.

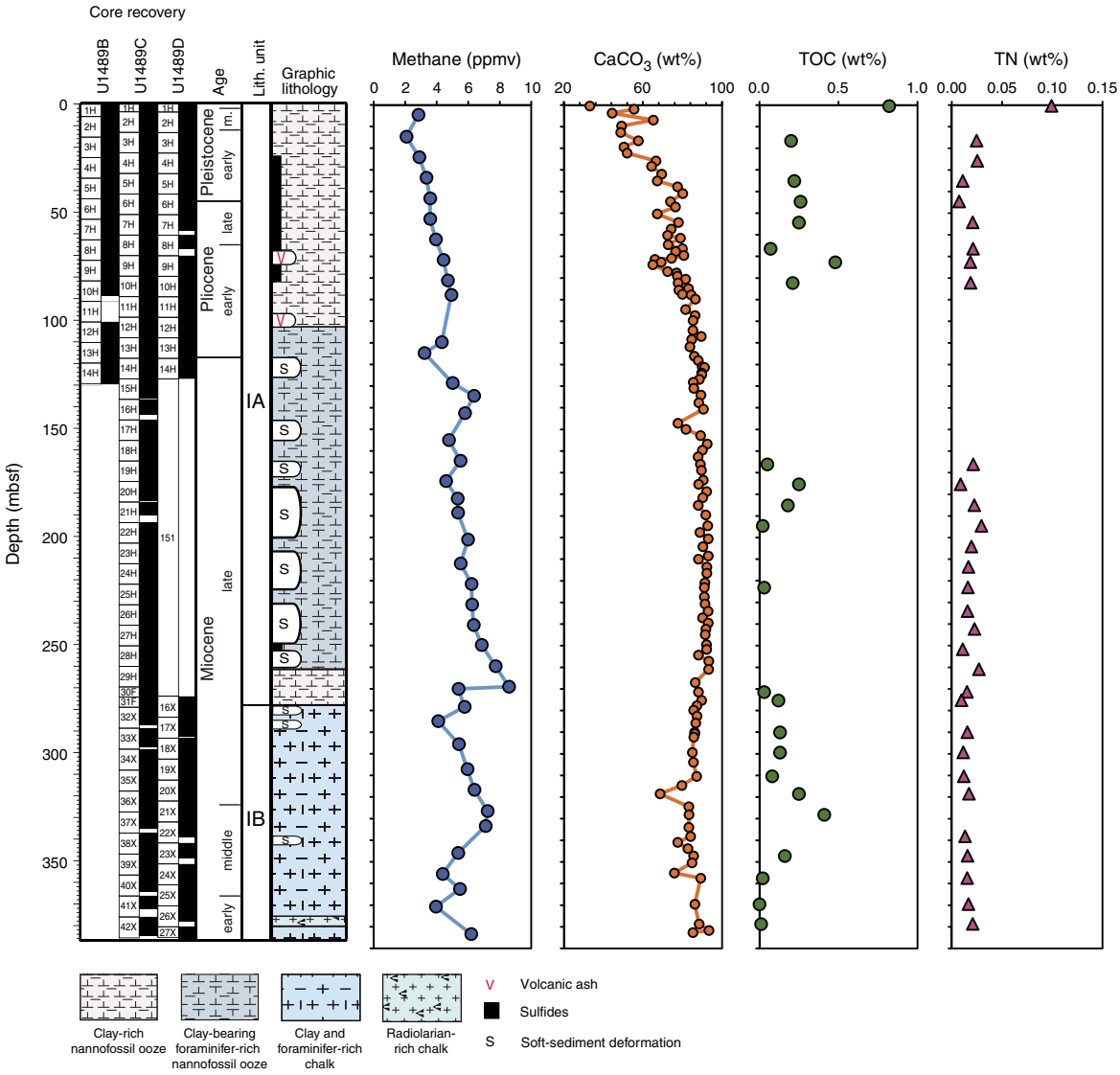

Table T25. Calcium carbonate, total organic carbon, and total nitrogen, Holes U1489B and U1489C. **Download table in CSV format.**

at 4.4 mbsf to 1.0 µM at ~10.1 mbsf (Figure F36). As at Site U1488, this abrupt decrease could reflect a combination of organic matter remineralization scavenging of PO_4 by sorption to clay minerals or local diagenetic precipitation of carbonate fluorapatite; the latter would be in agreement with evidence of carbonate dissolution in the upper sediment layers (see **Discussion**). PO_4 concentration remains low and relatively constant below 10.1 mbsf, with again a slight offset observed at ~88 mbsf where sampling switched from Hole U1489B to Hole U1489C.

Ammonium (NH_4) concentration increases from 0.03 mM at the mudline to 0.2–0.3 mM between 126.4 and 285.5 mbsf (Figure F36). Deeper than 285.5 mbsf, NH_4 concentration decreases slightly to 0.2 mM at 381.8 mbsf. As at Site U1488, the overall low NH_4 concentration at Site U1489 reflects generally low organic matter content. Bromide (Br) concentration remains largely constant throughout the hole with average values of 0.91 ± 0.02 mM, again reflecting the low organic matter content (Figure F36). Some anomalously high Br values occur in a few samples below 100 mbsf.

Manganese and iron

Manganese (Mn) concentration increases abruptly from a mudline value of 1.3 µM to 128.5 µM at 4.4 mbsf, indicating the presence of an oxic/suboxic redox boundary within this depth range (Figure F36). Deeper than 4.4 mbsf, Mn concentration decreases linearly to 7.7 µM by 38.6 mbsf and decreases further with depth to a minimum of 1.4 µM at 107.4 mbsf. This decrease suggests that Mn released from the reduction of Mn oxyhydroxide phases in the upper 4.4 mbsf is scavenged mostly deeper than 38.6 mbsf. Deeper than 107.4 mbsf, Mn concentration is nearly constant to 268.9 mbsf, at which point there is a very small, gradual increase to ~1.9 µM at 382 mbsf.

Iron (Fe) behaves similarly to dissolved Mn in the upper ~100 mbsf (Figure F36) but displays two peaks in concentration: ~40 µM between 10.1 and 33.6 mbsf and ~20 µM between 52.6 and 76.6 mbsf. As with Mn, the Fe profile in the upper sediment column is

Figure F36. Interstitial water concentration profiles, Holes U1489B and U1489C. Black stars = mudline samples, dashed line = transition at 88 mbsf from Hole U1489B samples to Hole U1489C samples; sharp offsets seen at this depth should be accounted for in any interpretation of these geochemical profiles. Fe mudline concentration of was below detection limit and is not plotted.

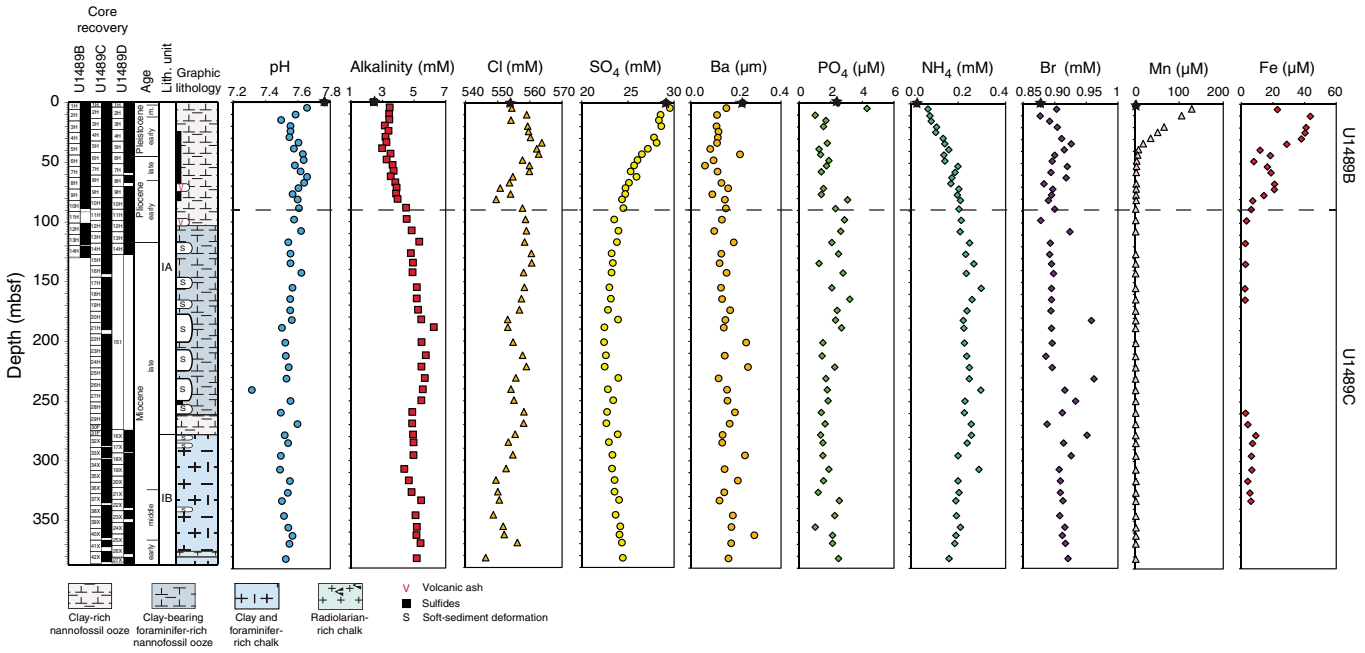

probably controlled by the reduction of Fe hydroxides and oxyhydroxides during organic matter remineralization. Dissolved Fe concentration remains very low between 76.6 and 249.6 mbsf, falling mostly below detection limit. As at Site U1488, the bottom portion of Site U1489 is characterized by slightly elevated dissolved Fe concentration, with an average value of ~6 µM deeper than 249.6 mbsf.

Potassium, magnesium, and calcium

Potassium increases from the mudline (10.5 mM) to 19.6 mbsf (13.5 mM) (Figure **F37**). K concentration remains high (>12.5 mM) downhole to 81.1 mbsf, where a sharp transition to near-constant values (11.5 ± 0.3 mM) occurs at the depth at which we began taking interstitial water measurements from Hole U1489C. As discussed above, this transition may be due to local differences between the two holes or procedural/analytical offsets rather than reflecting a major change in the interstitial water geochemical composition at Site U1489. As at Site U1488, calcium (Ca) concentration remains generally constant in the upper ~43 mbsf of Hole U1489B (~10.6 mM) (Figure **F37**). Below that depth, Ca decreases to a minimum value of 9.1 mM between 58 and 67 mbsf before increasing steadily and progressively below this interval to 15.3 mM at 381.8 mbsf. Magnesium (Mg) exhibits a progressive decrease from seawater-like values at the mudline (54.2 mM) to 43.5 mM at 326.4 mbsf (Figure **F37**). The bottom part of Hole U1489C (deeper than 326.4 mbsf) is characterized by a slight increase in Mg to 46.7 mM.

Strontium and boron

As at Site U1488, strontium (Sr) shows a steady increase over the upper 200 mbsf from a mudline Sr concentration of 0.1 mM to a maximum concentration of ~1.1 mM between 200.9 and 268.9 mbsf (Figure **F37**). Deeper than 270 mbsf, Sr concentration decreases toward the base of the hole and reaches 0.85 mM at 381.8 mbsf. Boron is similar to potassium, displaying a slight increase from the mudline (444.3 µM) to 516.6 µM at 10.1 mbsf (Figure **F37**). Below this depth, B concentration is >470 µM down to 81.1 mbsf. The sharp drop at ~88 mbsf coincides with the switch to sampling from Hole U1489B to Hole U1489C, and below that depth B concentration remains relatively constant downhole with an average value of 409 ± 10 µM.

Lithium, silica, and sodium

Lithium (Li) concentration decreases steadily from a mudline value of 25.5 µM to 15.5 µM in the interval between ~10 and 67 mbsf (Figure **F37**). Below this depth, Li concentration decreases steadily to a minimum value of 5.2 µM at 200.9 mbsf before increasing again to 10.6 mM at 316.6 mbsf. The rest of the hole is characterized by near-constant Li concentration. Silica (Si) concentration displays small variations (between ~380 and 420 µM) in the upper 29 mbsf of the hole (Figure **F37**). Below this depth, Si concentration increases to reach a local maximum of ~620 µM between ~39 and 53 mbsf. From 67.1 to 97.9 mbsf, Si concentration increases somewhat quickly from 441.4 to 869.6 µM and increases more gradually below that to a concentration of 1146 µM at the base of the hole. Sodium (Na) concentration is fairly constant throughout the entire hole, averaging 491 ± 9 mM (Figure **F37**).

Discussion

The interstitial water chemistry at Site U1489 is representative of carbonate-dominated deep-ocean sedimentary settings and is much like that of Site U1488; however, there are some notable differences between the two sites. Low organic matter input to the sediment under the oxic water column at Site U1489 and a low sedimentation rate relative to the shallower sites drilled thus far during Expedition 363 result in relatively little anoxic organic matter remineralization at this site, as evidenced by the presence of sulfate at high (>22 mM) concentration at depth and moderate downhole increases in NH_4 and Br concentrations. Slightly higher dissolved Fe concentration and substantially higher dissolved Mn concentration suggest that suboxic remineralization of organic matter at Site U1489 is enhanced relative to Site U1488, and these pro-

Figure F37. Interstitial water concentration profiles, Holes U1489B and U1489C. Black stars = mudline samples, dashed line = transition at 88 mbsf from Hole U1489B samples to Hole U1489C samples; sharp offsets seen at this depth should be accounted for in any interpretation of these geochemical profiles.

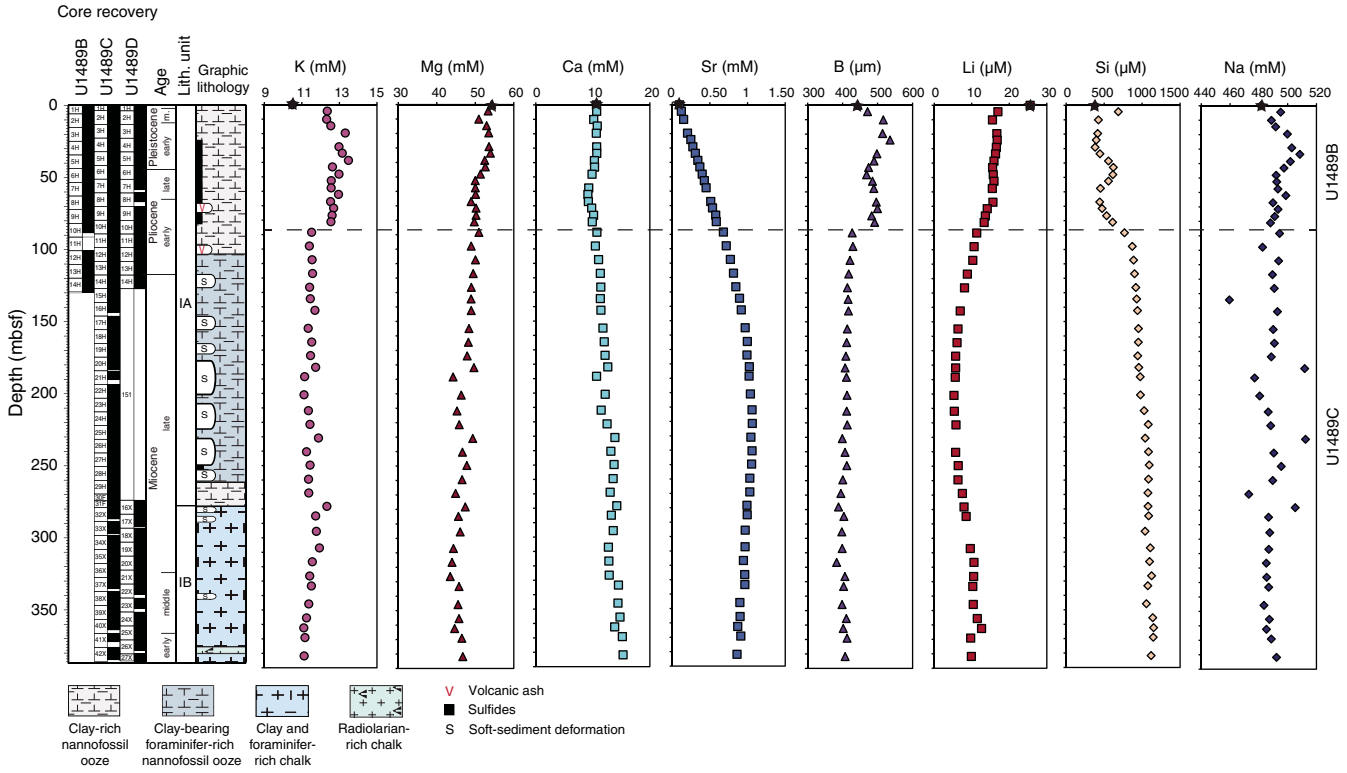

Table T26. Interstitial water geochemical data, Holes U1489B and U1489C. **Download table in CSV format.**

cesses may make a more significant contribution to organic matter degradation here than at other sites. Previous work by Bender et al. (1970) found a relatively high rate of Mn deposition in seafloor sediment in the western equatorial Pacific within a few hundred kilometers of the Eauripik Rise. The slightly lower sedimentation rate at Site U1489 than at Site U1488, if coupled with a similar rate of hydrogenous Mn accumulation at both sites, may result in greater sedimentary Mn content available for early diagenetic processes at Site U1489 and account for this difference.

Downhole trends in Ca, Mg, and Li at Site U1489 are similar to those at Site U1488 but are much more muted. A peak in Sr concentration of similar magnitude to the peak at Site U1488, albeit at greater depth at Site U1489, suggests that a decrease in carbonate dissolution is not responsible for the much lower Ca gradient with depth at Site U1489. Instead, the muted trends suggest a weaker influence of deep fluids with chemistry reflective of basalt-seawater interaction at this site. Site U1489 is located on the flank of the Eauripik Rise in water that is >800 m deeper than at Site U1488. Although its origin is not well constrained, one theory is that hotspot volcanism may have created the Eauripik Rise (Hegarty and Weissel, 1988). At the off-axis setting of Site U1489, the basaltic basement is likely older than that at Site U1488, with more time to accumulate a thicker sedimentary package at Site U1489 relative to Site U1488. These differences in basement and age/sediment thickness would contribute to the reduced gradients in the concentrations of Mg, Ca, and other ions produced or consumed during seawater-basalt interactions observed at Site U1489 and could help to explain the differences in the profiles between Sites U1488 and U1489.

References

Bender, M.L., Ku, T.-L., and Broecker, W.S., 1970. Accumulation rates of manganese in pelagic sediments and nodules. *Earth and Planetary Science Letters*, 8(2):143–148. **https://doi.org/10.1016/0012-821X(70)90164-0**

Bolli, H.M., 1957. Planktonic foraminifera from the Eocene Navet and San Fernando formations of Trinidad, B.W.I. *In* Loeblich, A.R., Jr. (Ed.), *Studies in Foraminifera*. Bulletin of the United States National Museum, 215:155–172. **http://biostor.org/reference/106017**

Bracey, D.R., 1975. Reconnaissance geophysical survey of the Caroline Basin. *Geological Society of America Bulletin,* 86(6):775–784. **https://doi.org/10.1130/0016-7606(1975)86<775:RGSOTC>2.0.CO;2**

Cande, S.C., and Kent, D.V., 1995. Revised calibration of the geomagnetic polarity timescale for the Late Cretaceous and Cenozoic. *Journal of Geophysical Research: Solid Earth,* 100(B4):6093–6095. **https://doi.org/10.1029/94JB03098**

Hegarty, K.A., and Weissel, J.K., 1988. Complexities in the developments of the Caroline plate region, western equatorial Pacific. *In* Nairn, A.E.M., Stehli, F.G., and Uyeda, S. (Eds.), *The Ocean Basins and Margins:* Boston (Springer), 277–301. **https://doi.org/10.1007/978-1-4615-8041-6_6**

Hilgen, F.J., Lourens, L.J., and Van Dam, J.A., 2012. The Neogene period. With contributions by A.G. Beu, A.F. Boyes, R.A. Cooper, W. Krijgsman, J.G. Ogg, W.E. Piller, and D.S. Wilson. *In* Gradstein, F.M., Ogg, J.G., Schmitz, M.D., and Ogg, G.M. (Eds.), *The Geologic Time Scale:* Oxford, United Kingdom (Elsevier), 923–978. **https://doi.org/10.1016/B978-0-444-59425-9.00029-9**

Hodell, D.A., and Kennett, J.P., 1986. Late Miocene–early Pliocene stratigraphy and paleoceanography of the South Atlantic and southwest Pacific Oceans: a synthesis. *Paleoceanography and Paleoclimatology,* 1(3):285–311. **https://doi.org/10.1029/PA001i003p00285**

Karlin, R., and Levi, S., 1983. Diagenesis of magnetic minerals in recent hemipelagic sediments. *Nature,* 303(5915):327–330. **https://doi.org/10.1038/303327a0**

Kennett, J.P., and Srinivasan, M.S., 1983. *Neogene Planktonic Foraminifera: A Phylogenetic Atlas:* Stroudsburg, PA (Hutchinson Ross).

Mills, P.C., 1983. Genesis and diagnostic value of soft-sediment deformation structures—a review. *Sedimentary Geology*, 35(2):83–104. **https://doi.org/10.1016/0037-0738(83)90046-5**

Pearson, P.N., 1995. Planktonic foraminifer biostratigraphy and the development of pelagic caps on guyots in the Marshall Islands group. *In* Haggerty, J.A., Premoli Silva, I., Rack, F., and McNutt, M.K. (Eds.), *Proceedings of the Ocean Drilling Program, Scientific Results,* 144: College Station, TX (Ocean Drilling Program), 21–59. **https://doi.org/10.2973/odp.proc.sr.144.013.1995**

Pribnow, D., Kinoshita, M., and Stein, C., 2000. *Thermal Data Collection and Heat Flow Recalculations for Ocean Drilling Program Legs 101–180:* Hanover, Germany (Institute for Joint Geoscientific Research, Institut für Geowissenschaftliche Gemeinschaftsaufgaben [GGA]). **http://www-odp.tamu.edu/publications/heatflow/ODPReprt.pdf**

Rosenthal, Y., Holbourn, A., and Kulhanek, D.K., 2016. *Expedition 363 Scientific Prospectus: Western Pacific Warm Pool.* International Ocean Discovery Program. **https://doi.org/10.14379/iodp.sp.363.2016**

Rosenthal, Y., Holbourn, A.E., Kulhanek, D.K., Aiello, I.W., Babila, T.L., Bayon, G., Beaufort, L., Bova, S.C., Chun, J.-H., Dang, H., Drury, A.J., Dunkley Jones, T., Eichler, P.P.B., Fernando, A.G.S., Gibson, K.A., Hatfield, R.G., Johnson, D.L., Kumagai, Y., Li, T., Linsley, B.K., Meinicke, N., Mountain, G.S., Opdyke, B.N., Pearson, P.N., Poole, C.R., Ravelo, A.C., Sagawa, T., Schmitt, A., Wurtzel, J.B., Xu, J., Yamamoto, M., and Zhang, Y.G., 2018a. Expedition 363 methods. *In* Rosenthal, Y., Holbourn, A.E., Kulhanek, D.K., and the Expedition 363 Scientists, *Western Pacific Warm Pool.* Proceedings of the International Ocean Discovery Program, 363: College Station, TX (International Ocean Discovery Program). **https://doi.org/10.14379/iodp.proc.363.102.2018**

Rosenthal, Y., Holbourn, A.E., Kulhanek, D.K., Aiello, I.W., Babila, T.L., Bayon, G., Beaufort, L., Bova, S.C., Chun, J.-H., Dang, H., Drury, A.J., Dunkley Jones, T., Eichler, P.P.B., Fernando, A.G.S., Gibson, K.A., Hatfield, R.G., Johnson, D.L., Kumagai, Y., Li, T., Linsley, B.K., Meinicke, N., Mountain, G.S., Opdyke, B.N., Pearson, P.N., Poole, C.R., Ravelo, A.C., Sagawa, T., Schmitt, A., Wurtzel, J.B., Xu, J., Yamamoto, M., and Zhang, Y.G., 2018b. Site U1482. *In* Rosenthal, Y., Holbourn, A.E., Kulhanek, D.K., and the Expedition 363 Scientists, *Western Pacific Warm Pool.* Proceedings of the International Ocean Discovery Program, 363: College Station, TX (International Ocean Discovery Program). **https://doi.org/10.14379/iodp.proc.363.103.2018**

Rosenthal, Y., Holbourn, A.E., Kulhanek, D.K., Aiello, I.W., Babila, T.L., Bayon, G., Beaufort, L., Bova, S.C., Chun, J.-H., Dang, H., Drury, A.J., Dunkley Jones, T., Eichler, P.P.B., Fernando, A.G.S., Gibson, K.A., Hatfield, R.G., Johnson, D.L., Kumagai, Y., Li, T., Linsley, B.K., Meinicke, N., Mountain, G.S., Opdyke, B.N., Pearson, P.N., Poole, C.R., Ravelo, A.C., Sagawa, T., Schmitt, A., Wurtzel, J.B., Xu, J., Yamamoto, M., and Zhang, Y.G., 2018c. Site U1488. *In* Rosenthal, Y., Holbourn, A.E., Kulhanek, D.K., and the Expedition 363 Scientists, *Western Pacific Warm Pool.* Proceedings of the International Ocean Discovery Program, 363: College Station, TX (International Ocean Discovery Program). **https://doi.org/10.14379/iodp.proc.363.109.2018**

Rowan, C.J., Roberts, A.P., and Broadbent, T., 2009. Reductive diagenesis, magnetite dissolution, greigite growth and paleomagnetic smoothing in marine sediments: a new view. *Earth and Planetary Science Letters,* 277(1–2):223–235. **https://doi.org/10.1016/j.epsl.2008.10.016**

Saito, T., 1976. Geologic significance of coiling direction in the planktonic foraminifer *Pulleniatina. Geology,* 4(5):305–309. **https://doi.org/10.1130/0091-7613(1976)4<305:GSOCDI>2.0.CO;2**

Shipboard Scientific Party, 1971, Site 62. *In* Winterer, E.L., Riedel, W.R., Brönnimann, P., Gealy, E.L., Heath, G.R., Kroenke, L., Martini, E., Moberly Jr., R., Resig, J., and Worsley, T. (Eds.), *Initial Reports of the Deep Sea Drilling Project*, 49–322. **https://doi.org/10.2973/dsdp.proc.7.104.1971**

Stoner, J.S., and St-Onge, G., 2007. Magnetic stratigraphy in paleooceanography: reversal, excursion, paleointensity and secular variation. *In* Hillaire-Marcel, C., and de Vernal, A. (Eds.), *Developments in Marine Geology* (Volume 1): *Proxies in Late Cenozoic Paleoceanography.* R. Stein (Series Ed.): Amsterdam (Elsevier B.V.), 99–138. **https://doi.org/10.1016/S1572-5480(07)01008-1**

van Morkhoven, F.P.C.M., Berggren, W.A., Edwards, A.S., and Oertli, H.J., 1986. Cenozoic cosmopolitan deep-water benthic foraminifera. *Bulletin des Centres de Recherches Exploration-Production Elf-Aquitaine,* 11.

Wade, B.S., Pearson, P.N., Berggren, W.A., and Pälike, H., 2011. Review and revision of Cenozoic tropical planktonic foraminiferal biostratigraphy and calibration to the geomagnetic polarity and astronomical time scale. *Earth-Science Reviews,* 104(1–3):111–142. **https://doi.org/10.1016/j.earscirev.2010.09.003**

Wilkens, R.H., Westerhold, T., Drury, A.J., Lyle, M., Gorgas, T., and Tian, J., 2017. Revisiting the Ceara Rise, equatorial Atlantic Ocean: isotope stratigraphy of ODP Leg 154. *Climate of the Past,* 13:779–793. **https://doi.org/10.5194/cp-13-779-2017**

Zijderveld, J.D.A., 1967. AC demagnetization of rocks: analysis of results. *In* Collinson, D.W., Creer, K.M., and Runcorn, S.K. (Eds.), *Developments in Solid Earth Geophysics* (Volume 3): *Methods in Palaeomagnetism:* Amsterdam (Elsevier), 254–286. **https://doi.org/10.1016/B978-1-4832-2894-5.50049-5**